Photonic crystal rod fibers: Understanding a new class of active optical waveguides

Laurila, Marko; Lægsgaard, Jesper; Broeng, Jes; Alkeskjold, Thomas Tanggaard

Publication date:
2012

Document Version
Publisher's PDF, also known as Version of record

Photonic crystal rod fibers: Understanding a new class of active optical waveguides

Ph.D. Thesis
Marko Laurila

November 29th, 2012

DTU Fotonik
Department of Photonics Engineering

DTU Fotonik
Department of Photonics Engineering
Technical University of Denmark
Building 345V
DK-2800 Kgs. Lyngby
Denmark

Preface

The work presented in this thesis has been carried out as a part of my Ph.D. project in the period January 2nd 2010 – November 30th 2012.

The work took place at DTU Fotonik Department of Photonics Engineering, Technical University of Denmark, Kgs. Lyngby, Denmark and the experimental part was conducted at NKT Photonics, Birkerød, Denmark. In addition, external research stays were carried out at EOLITE Systems, Pessac, France, and Friedrich Schiller University Jena, Institute of Applied Physics, Jena, Germany, and Boston University, Nanostructured Fibers and Nonlinear Optics, Boston, USA.

The project was financed by Technical University of Denmark under The Danish Council for Independent Research and Technology and Production Sciences (FTP) and supervised by

- Jesper Lægsgaard, Assoc. Professor, DTU Fotonik, Technical University of Denmark, Kgs. Lyngby, Denmark
- Jes Broeng, Ph.D., NKT Photonics A/S, Birkerød, Denmark
- Thomas Tanggaard Alkeskjold, Ph.D., NKT Photonics A/S, Birkerød, Denmark

Virum, 29th November 2012

Marko Laurila

Contents

Acknowledgements

First of all I would like to thank my supervisors for giving me an opportunity to do a Ph.D. project together with DTU Fotonik and NKT Photonics. Their support, suggestions and guidance kept me on the right track during my project and made the three years enjoyable. I thank Jes Broeng for creating and letting me be part of NKT Photonics' creative fiber technology team with full support of the company. I thank Jesper Lægsgaard for always helping, supporting and challenging me theoretically during my project. Special thanks goes out to Thomas T. Alkeskjold, whose constant drive to help and share his experimental and theoretical knowledge made it possible to complete the experimental studies and successfully analyze measurement results.

I would like to thank all people at EOLITE Systems, Pessac, France; Friedrich Schiller University Jena, Institute of Applied Physics, Jena, Germany and Boston University, Nanostructured Fibers and Nonlinear Optics, Boston, USA for their help and for giving me an opportunity to collaborate with them.

Thanks goes out to my former Ph.D. student colleagues Danny Noordegraaf, Christina B. T. Olausson, Jens K. Lyngsøe, Kristian R. Hansen, Jure Grgic, Anna C. Brunetti and Alessio Stefani for always helping out. Big thanks also to my fellow Ph.D. students Simon T. Sørensen, Mette M. Jørgensen and Sidsel R. Petersen for having great time in the lab as well as abroad at conferences. Also very warm thanks to all people at DTU Fotonik and NKT Photonics, especially Lara Scolari and Johannes Weirich, with whom I had pleasure to work with for their positive and helpful attitude. Special thanks to Chris Brooks for critical discussions, help on writing the thesis by correcting endless grammar mistakes and having good craic in the lab.

Big thanks goes out to Tarja who has been with me and always supporting me, Sami who gave a new perspective to my life, my family and friends for their help and support during my Ph.D. project.

Last I would like to honor the passing of my father, who always motivated me on my career. He only saw the beginning of my Ph.D.

project but was not fortunate enough to see my graduation.

Abstract

In this PhD thesis an experimental study of modal characterization methods on large mode area photonic crystal fibers (PCFs) is performed and the development of a new ytterbium-doped photonic bandgap PCF rod fiber is presented.

The first focus of this work is to use modal characterization methods which can accurately resolve propagation modes and their weights in optical waveguides to examine guiding properties and single-mode (SM) operation of different PCFs. A spatially and spectrally resolved (S^2) imaging setup is developed to evaluate the SM properties of flexible PCF with a 40 μm core diameter. The limitations of the method are discussed and another modal characterization method is introduced. Cross correlated (C^2) imaging, which can resolve modes in fibers with very large cores, is described. C^2 imaging is then successfully employed to verify the resonant coupling condition between core modes and the cladding band as the underlying mechanics to ensure SM operation of the new rod fiber design (85 μm core diameter), which was developed during this thesis work.

The second focus of this work is the study of the new ytterbium-doped rod fiber design under active operation. Performance of the rod fiber is evaluated in high power laser and laser amplifier configurations. The high power rod amplifier setup including the seed source is developed and characterized. Results obtained from the rod fiber showed simultaneously SM, near diffraction limited output beam quality with high average power and pulse energy generation using both laser and laser amplifier configurations. Modal instabilities (MIs) in high power fiber amplifiers are discussed, and a memory effect of the MI threshold level together with a recovery method and evidence of improved performance while suppressing MIs are reported. Thermally induced refractive index changes in the core under high power operation is discussed and quantified as a shift of the photonic bandgap in the rod fiber design.

Resumé (Danish abstract)

I denne afhandling gennemføres en eksperimentel undersøgelse af modale karakteriseringsmetoder på stor-kerne fotoniske krystalfibre (PCFs) præsenteres udviklingen af en ny ytterbium-doteret fotonisk båndgabs (PBG) rod fiber.

Det første mål i dette arbejde er at bruge modale karakteriseringsmetoder, der kan skelne propagerende modes og deres vægt i en optisk bølgeleder med stor nøjagtighed, til at undersøge bølgeledende egenskaber og single-mode (SM) opførsel af forskellige PCF. En opstilling til spatially and spectrally resolved (S^2) afbildning er udviklet til at vurdere SM egenskaber af fleksible PCFs. Begrænsningerne ved fremgangsmåden diskuteres og en anden modal karakteriseringsmetode introduceres. Krydskorreleret (C^2) afbildning, der kan skelne modes i fibre med meget store kerner, beskrives. C^2 afbildning anvendes derpå med held til at verificere den resonante koblingsbetingelse mellem kerne- og kappe-modes som de underliggende mekanismer der sikrer SM opførsel af det nye rod fiber design (85 μm core diameter), som blev udviklet i løbet af dette projekt.

Det andet fokusområde i dette arbejde er et studie af det nye ytterbium-doterede rod fiber design når det opereres som forstærker. Rodfiberens funktionalitet evalueres i laser- og forstærkerkonfigurationer. En højeffekts rod-forstærkeropstilling, inklusiv seed-laser, udvikles og karakteriseres. Resultater opnået med rod-fiberen viste samtidig SM, nær diffraktionsbegrænset strålekvalitet ved forstærkerudgangen, med høj gennemsnitlig effekt og pulsenergi i både laser- og forstærkerkonfigurationer. Modale ustabiliteter (MIs) i højeffekts-fiberforstærkere diskuteres, og en degradering af MI tærsklen over tid demonstreres, sammen med en metode til delvis gendannelse af den oprindelige tilstand. Forbedret ydelse og MI-undertrykkelse ved brug af denne metode dokumenteres. Termo-optiske effekter i kernen ved høj udgangseffekt diskuteres, og kvantificeres som en forskydning af rod-fiberens båndgab.

Publication list

Journal publications

1. M. M. Jørgensen, **M. Laurila**, D. Noordegraaf, T. T. Alkeskjold, J. Lægsgaard, "Photo-recovery of modal stability in rod fiber amplifiers," Optics Express, to be submitted (2013).

2. **M. Laurila**, R. Barankov, M. M. Jørgensen, T. T. Alkeskjold, J. Broeng, J. Lægsgaard, S. Ramachandran, "Cross-correlation Imaging of Single-Mode Photonic Crystal Rod Fiber with Distributed Mode Filtering," Optics Express, submitted (2013).

3. **M. Laurila**, M. M. Jørgensen, K. R. Hansen, T. T. Alkeskjold, J. Broeng, J. Lægsgaard, "Distributed mode filtering rod fiber amplifier delivering 292W with improved mode stability," Optics Express, **20**(5), 5742, (2012).

4. M. M. Jørgensen, S. R. Petersen, **M. Laurila**, J. Lægsgaard, T. T. Alkeskjold, "Optimizing single mode robustness of the distributed modal filtering rod fiber amplifier," Optics Express, **20**(7), 7263, (2012).

5. S. R. Petersen, T. T. Alkeskjold, F. Poli, E. Coscelli, M. M. Jørgensen, **M. Laurila**, J. Lægsgaard, J. Broeng "Hybrid Ytterbium-doped large-mode-area photonic crystal fiber amplifier for long wavelengths," Optics Express, **20**(6), 6010, (2012).

6. **M. Laurila**, J. Saby, T. T. Alkeskjold, L. Scolari, B. Cocquelin, F. Salin, J. Broeng, J. Lægsgaard, "Q-switching and efficient harmonic generation from a single-mode LMA photonic bandgap rod fiber laser," Optics Express, **19**(11), 10824, (2011).

7. **M. Laurila**, T. T. Alkeskjold, J. Lægsgaard, J. Broeng, "Modal analysis of a large-mode area photonic crystal fiber amplifier using spectral-resolved imaging," Optical Engineering, **50**(11), 111604 (2011).

8. T. T. Alkeskjold, **M. Laurila**, L. Scolari, and J. Broeng, "Single-mode ytterbium-doped large-mode-area photonic bandgap rod fiber amplifier," Optics Express, **19**(8), 7398, (2011).

9. K. P. Hansen, C. B. Olausson, J. Broeng, D. Noordegraaf, M. D. Maack, T. T. Alkeskjold, **M. Laurila**, T. Nikolajsen, P. M. W. Skovgaard, M. H. Sørensen, M. Denninger, C. Jakobsen, and H. R. Simonsen, "Airclad fiber laser technology," Optical Engineering **50**(11), 111609, (2011).

Conference contributions

1. **M. Laurila**, R. Barankov, T. T. Alkeskjold, J. Broeng, J. Lægsgaard, S. Ramachandran, "Resonant coupling in single mode photonic crystal rod fiber with distributed mode filtering verified using cross correlated imaging," Proceedings of SPIE, accepted for publication, paper 8601-19 (2013).

2. S. R. Petersen, T. T. Alkeskjold, **M. Laurila**, T. V. Andersen, J. Lægsgaard, "Nonlinear spatial mode imaging of hybrid photonic crystal," Proceedings of SPIE, accepted for publication, paper 8601-21 (2013).

3. M. M. Jørgensen, **M. Laurila**, D. Noordegraaf, T. T. Alkeskjold, J. Lægsgaard, "Thermal-recovery of modal instability in rod fiber amplifiers," Proceedings of SPIE, accepted for publication, paper 8601-29 (2013).

4. M. M. Jørgensen , K. R. Hansen, **M. Laurila**, T. T. Alkeskjold, J. Lægsgaard, "Modal instability of rod fiber amplifiers: a semi-analytic approach," Proceedings of SPIE, accepted for publication, paper 8601-73 (2013).

5. **M. Laurila**, T. T. Alkeskjold, J. Broeng, J. Lægsgaard, "Distributed Mode Filtering Rod Fiber Amplifier With Improved Mode Stability," - OSA Technical Digest (CD). Lasers, Sources, and Related Photonic Devices, paper FW5C.4, OSA, (2012).

6. **M. Laurila**, T. T. Alkeskjold, M. M. Jørgensen, S. R. Petersen, J. Broeng, J. Lægsgaard, "Highly efficient high power single-mode fiber amplifier utilizing the distributed mode filtering bandgap rod fiber," Proceedings of SPIE, Vol. 8237, pp. 823710-9, (2012).

7. T. T. Alkeskjold, **M. Laurila**, M. M. J ørgensen, S. Petersen, J. Broeng, C. Olausson, and J. Lægsgaard, "Advances in Solid Core

Photonic Bandgap Fiber Amplifiers," in Optical Fiber Communication Conference, OSA Technical Digest, paper OTh1H.1, (2012).

8. E. Coscelli, F. Poli, M. M. Joergensen, **M. Laurila**, J. Lægsgaard, T. T. Alkeskjold, L. Leick, J. Broeng, A. Cucinotta, S. Selleri, "Thermal effects in Yb-doped double-cladding Distributed Modal Filtering rod-type fibers," Transparent Optical Networks (ICTON), 2012 14th International Conference on , pp.1-4, (2012).

9. M. M Jørgensen, S. R. Petersen, **M. Laurila**, J. Lægsgaard, T. T. Alkeskjold, "Design optimization of the distributed modal filtering rod fiber for increasing single mode bandwidth," Proceedings of SPIE, Vol. 8237, pp. 82373P-10, (2012).

10. S. R. Petersen, T. T. Alkeskjold, F. Poli, E. Coscelli, M. M. Jørgensen, **M. Laurila**, J. Lægsgaard, J. Broeng "Ytterbium-doped large-mode-area photonic crystal fiber amplifier with gain shaping for use at long wavelengths," Proceedings of SPIE, Vol. 8237, pp. 82373O-8, (2012).

11. **M. Laurila**, J. Saby, T. T. Alkeskjold, L. Scolari, B. Cocquelin, F. Salin, J. Broeng, J. Lægsgaard, "Millijoule pulse energy second harmonic generation with single-stage photonic bandgap rod fiber laser," 2011 Conference on Lasers and Electro-Optics Europe and 12th European Quantum Electronics Conference (CLEO EUROPE/EQEC), (2011) **post-deadline paper**.

12. **M. Laurila**, T. T. Alkeskjold, J. Lægsgaard, J. Broeng, "Spatial and spectral imaging of LMA photonic crystal fiber amplifiers," Proceedings of SPIE, Vol. 7914, pp. 79142D-9, (2011).

13. T. T. Alkeskjold, **M. Laurila**, L. Scolari, and J. Broeng, "Low-NA single-mode LMA photonic crystal rod fiber amplifier," Proceedings of SPIE, Vol. 7914, pp. 79141S-9, (2011).

14. J. Broeng, **M. Laurila**, D. Noordegraaf, C. B. Olausson, K. P. Hansen, M. D. Maack, T. T. Alkeskjold, J. K. Lyngsøe, M. Denninger, C. Jakobsen, H. R. Simonsen, "Photonic crystal fibres in the market," in 16th Opto-Electronics and Communications Conference (OECC), pages: 53-54, 2011, IEEE, (2011).

Chapter 1

Introduction

Optical fibers were invented over a hundred years ago but the discoveries in 1970 [1] revolutionized the modern world, especially in the area of telecommunications by providing a way to transfer large amounts of data over long distances [2]. Already by the end of the 1990's fibers were used around the world. Their use had rapidly expanded beyond the area of optical telecommunications to include new applications in various fields [3]. Rear earth (RE) doping of optical fibers [4] expanded the use of fiber optics even more and erbium doped fiber amplifiers were utilized as a part of telecommunication networks as early as the mid 1990's [3]. However, new RE ions such as neodymium and ytterbium soon revolutionized methods for material processing [5, 6]. Ytterbium (Yb) doping of optical fibers soon became the most dominant method to pursue high power fiber laser operation [7], and after the so called double cladding design was introduced the output of fiber laser systems had grown exponentially [8].

Laser transitions can be discovered in many types of materials when they are doped with active RE ions. Gases, liquids, solid-state materials and semiconductors can serve as host materials; however, the energy difference between the pump and laser photons, the so called quantum defect, causes a thermal load inside the active material. This thermal load is not homogeneous and typically causes the thermal profile to be highest in the middle of the active medium. Power scaling will lead to a thermal lensing and birefringence by thermally induced mechanical-stress and eventually the beam quality is limited by thermo-optical effects. Therefore, it has become evident that reducing thermo-optical distortions is vital for high-power scaling efforts. Typically, solid-state laser geometries, especially at high power operation, suffer from the thermo-optical problems but they can be reduced by using thin disk [9]

or a slab [10] designs. These designs ease the thermo-optical problems, resulting in a nearly homogeneous temperature profile in the active medium and giving weaker thermal-lens and birefringence effects [8]. However, output power levels of kilowatts or multi-kilowatts require alternative methods to overcome the thermo-optical limitations and distribution of the thermal load over a long propagation length, such as in a shape of a fiber, is an excellent solution.

A fiber design, compared to the solid-state design, has a long gain medium length while maintaining a small cross-section, which results in outstanding thermo-optical properties [11]. The large surface-to-active volume ratio offers good heat dissipation over a long length and at the same time excellent confinement of the laser light inside the fiber structure. A fiber can either be core or cladding pumped and can be easily coiled, allowing for a small footprint and direct beam delivery [7]. Excellent beam quality can be achieved with a single-mode (SM) fiber design; however, when light propagates under tight confinement over considerable lengths in the core of a fiber, non-linear effects such as stimulated Raman scattering (SRS), simulated Brillouin scattering (SBS), Self-phase modulation, four-wave-mixing and self-focusing are enhanced [12]. The non-linear effects can be fatal and introduce fundamental limits to power scaling efforts of fibers. Therefore, a new era of novel fiber designs has emerged.

Non-linear effects scale with the intensity and the propagation length of the signal inside the core of the fiber, and thus novel fiber designs with larger effective core areas and shorter propagation lengths are needed. Special techniques using coiling or tapering of conventional step-index fibers can provide SM operation for core diameters up to 40 μm [13]. Other methods such as tailoring propagation loss of higher order modes (HOMs) for example in chirally coupled core fibers [14] and leakage channel fibers [15] are also being investigated. More precise control of the index contrast between the core and the cladding to manufacture a SM core can be achieved with PCF [16] and core diameters up to 100 μm are feasible [17]. Such a very large core fiber can deliver extreme peak powers and pulse energies with nearly diffraction limited output [18–20] without non-linear effect limiting the available power. However, very large effective core area fibers often support an increasing number of HOMs, thereby decreasing the beam quality. Requirements of SM operation of very large core fibers demand novel fiber designs to suppress any HOMs. One such method has already been shown to be successful and works by delocalizing the higher-order core modes [21]. In addition, manufacturability of the fiber designs with acceptable yield requires designs with more robustness against manufacturing

tolerances.

These high-performance fiber designs with large effective core areas require new experimental characterization methods to evaluate their modal properties and identify the SM guiding regime. The usual method employed to measure beam quality is the so called M^2 parameter, which characterizes among other things the angular divergence of the beam [22, 23]. However, even when this parameter is close to the limiting case of unity, which corresponds to a diffraction-limited Gaussian beam, SM operation is not necessarily guaranteed [24]. Therefore, new alternative methods which can reliably reveal the modal content of signal light propagating in optical waveguides are currently under active development.

In this Ph.D. thesis two modal characterization methods spatially and spectrally resolved (S^2) imaging [25] and cross correlated (C^2) imaging [26] are used to examine guiding properties and SM operation of two photonic crystal fibers (PCFs). An S^2 imaging setup is constructed, calibrated and utilized to characterized a flexible SM PCF with core diameter of 40 μm. A description of the setup and the mathematical routines used along the results are shown. The second modal characterization method, C^2 imaging, is applied to a new SM rod type fiber with core diameter of 85 μm. In this work the SM properties as well as resonant coupling between core modes and cladding band is investigated. For this purpose a C^2 imaging system was improved to accept rod type fibers. This work was performed in collaboration with Boston University.

The major part of this thesis consists of the development of a new ytterbium (Yb)-doped SM photonic bandgap (PBG) rod fiber design pioneered by Thomas T. Alkeskjold [27, 28] and a study of the modal properties using C^2 imaging. A fiber amplifier setup including a high power seed system is built, characterized and used to seed the rod fiber and high power experiments using the rod fiber in laser and laser amplifier configurations are performed. Efficiency and modal quality, as well as study of modal instabilities at high power operation are described in this thesis. In addition, thermally induced refractive index changes under high power operation are reported.

All the passive and active step-index large mode area (LMA) fibers and PCFs used in this thesis work were manufactured by NKT Photonics, Denmark, Birkerød.

The outline of the thesis is as follows:

Chapter 2 gives an introduction to optical fibers. First, a conventional

step-index fiber design is described, followed by more advanced fiber designs: PCF and PBG fiber designs. A rod fiber design together with an approach to ensure robust SM operation is also discussed.

Chapter 3 gives an introduction to fiber lasers and amplifiers and why they have become an important part of today's modern materials processing industry. Different operational conditions for fiber lasers and amplifiers are described. The chapter ends with a description of the limits for power scaling of fiber lasers and amplifiers.

Chapter 4 describes two modal characterization techniques for two different PCF designs. The chapter also describes the limiting factors of each characterization technique and a detailed study of SM properties of the fibers tested.

Chapter 5 describes the development of the new rod fiber design and its performance in a ns pulse width laser cavity. The chapter begins with an introduction of a new rod fiber design and a study of its guiding dynamics is shown together with the SM properties. Then a description of the experimental laser cavity setup is given. Last, the high power ns laser results are described and the chapter ends with frequency doubling and tripling results yielding record high pulse energies at visible and UV light from a simple Q-switched fiber laser cavity.

Chapter 6 describes the high power amplifier experiments performed with the new rod fiber design. First, the experimental setup is shown and the seed source and pump module are characterized. Then, efficiency and mode quality of the rod fiber is investigated under ultrafast pulse (ps) amplification. Modal instabilities (MIs) in rod fibers under high power operation are described. A permanent decay (memory effect) of the MI threshold level is described and a recovery method shown. In addition, an improvement of the MI threshold level is reported when the rod fiber is used in a special guiding regime. The chapter ends with a description of the thermally induced refractive index change of the core under a high power operation and physically manifests as a shift of the distinct photonic bandgap edge.

Chapter 7 holds the conclusion of this thesis and describes areas of possible future work.

Chapter 2

Optical fibers

This chapter gives an introduction to the basic properties of conventional step-index fiber, photonic crystal fiber (PCF), photonic bandgap (PBG) fiber, rod type fiber and large pitch fiber (LPF), explaining the guiding mechanism for each fiber type. In the last section, the well established method to determinate the M^2 parameter of a beam is discussed.

2.1 Step-index fibers

The simplest form of optical fiber is a step-index fiber made of a doped-silica glass core which is surrounded by a silica glass cylindrical cladding consisting of a lower refractive index material. The cladding is typically surrounded by a polymer based coating providing protection for more robust handling of the fiber. Figure 2.1 shows a cross section and a refractive index profile for a typical step-index fiber. The light propagating in the core is confined by total internal reflection (TIR) due to the refractive index contrast difference between the core and the cladding. However, the light is only guided in the core if the incident ray angle of propagation is below the critical angle $\theta_i < \theta_{max}$, illustrated in Fig. 2.2. The angle θ_r of the refracted light is defined by Snell's law as follows [29]

$$n_0 \sin\theta_i = n_1 \sin\theta_r \tag{2.1}$$

where n_0 and n_1 are refractive indices of the air and the fiber core, respectively. Internal to the fiber at the core/cladding interface, for an angle of incidence ϕ such that $\sin\phi < n_2/n_1$ where n_2 is the refractive index of the cladding, refraction is possible. The critical angle ϕ_c within the fiber is then defined through the relation

$$\sin\phi_c = \frac{n_2}{n_1}. \tag{2.2}$$

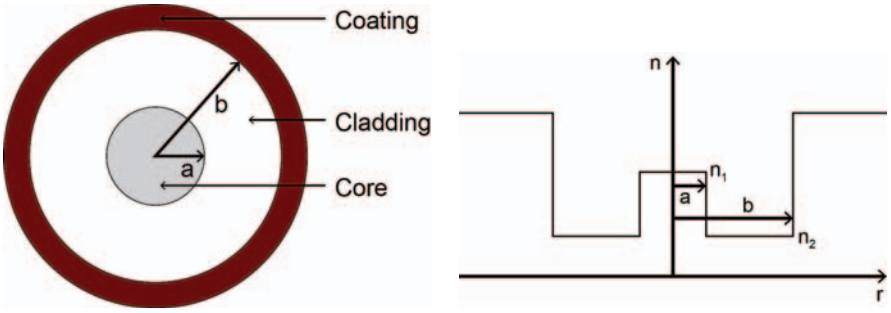

(a) (b)

Figure 2.1: (a) Cross section and (b) refractive index profile for step-index fiber.

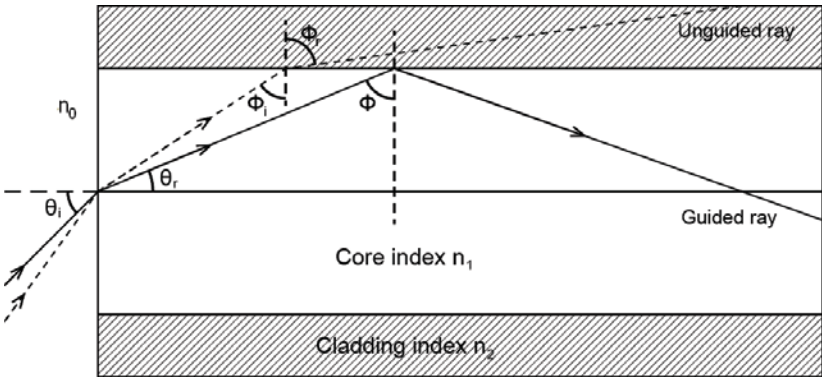

Figure 2.2: Illustration of total internal reflection in a step index fiber.

Using Eqs. 2.1 and 2.2 the maximum angle that the incident light will experience TIR and propagate along the fiber, can be calculated. The maximum acceptance angle θ_{max}, which is also known as the numerical aperture (NA), can be expressed through the following relation [29]

$$\sin\theta_{max} = \frac{1}{n_0}\sqrt{n_1^2 - n_2^2}. \tag{2.3}$$

2.1.1 Double cladding fiber structure

A double cladding fiber is an optical fiber which structure has two claddings surrounding the core. The core is surrounded by an inner cladding with a refractive index n_2, which is surrounded by a second cladding with a refractive index n_3 (outer cladding). Each layer of cladding has a lower refraction than the material it encases, shown in Fig. 2.3. The second cladding is typically made of a low index polymer

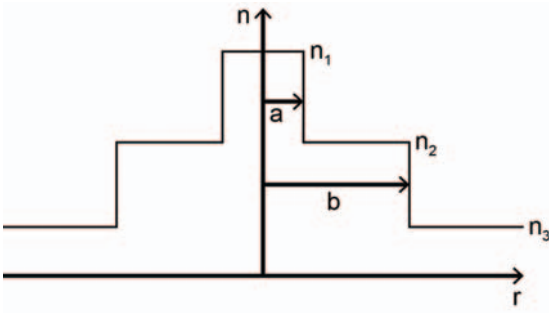

Figure 2.3: Refractive index profile of a double cladding step-index fiber.

or fluorinated silica, typically resulting in a maximum NA of ∼0.48 and ∼0.3 respectively [30]. However, the second cladding can also be realized with a ring of closely-spared air holes [31] enabling much higher NAs. A cladding NA of up to 0.9 has been demonstrated using this method [32]. This kind of fiber structure is commonly referred to as air-clad PCF which is explained in detail in Section 2.3.

2.2 Fiber modes

A fiber can support one or several spatial core modes, and for double clad fibers the cladding typically guides in the multimode regime, supporting hundreds of spatial modes. For normal applications guidance of a single spatial mode is preferable due to the resulting high beam quality and good pointing stability, and therefore a great deal of developmental work has been done to maintain the single-mode (SM) operation of large core fibers. The number of guided core modes in a standard, cylindrically-symmetric step-index fiber can be described by the V-number

$$V = \frac{2\pi}{\lambda} aNA \tag{2.4}$$

where a is the radius of core of the fiber [2]. A V-number below 2.405 is typically the criteria necessary to ensure SM operation of an optical fiber. However, even if the core has a V-number higher than 2.405 it can be operated such that a single spatial mode exits the fiber by introducing bend loss for higher order modes (HOMs) or by selective excitation of only the fundamental mode (FM) using mode matching.

2.3 Photonic crystal fibers

A photonic crystal fiber (PCF) is a microstructured fiber where the core light is confined by an arrangement of air holes in the cladding structure and the core is formed by one or more missing air holes in the middle of the fiber [16, 33]. Figure 2.4(a) shows a scanning electron microscope (SEM) image of the end facet of a passive solid core PCF. The distance between each air hole is referred to as pitch and is given by Λ while the air hole diameter is denoted d. The air holes in the cladding structure will effectively lower the refractive index of the cladding and therefore confine the light in the core by modified TIR [34].

PCFs can be engineered to guide only the FM, and thus perform

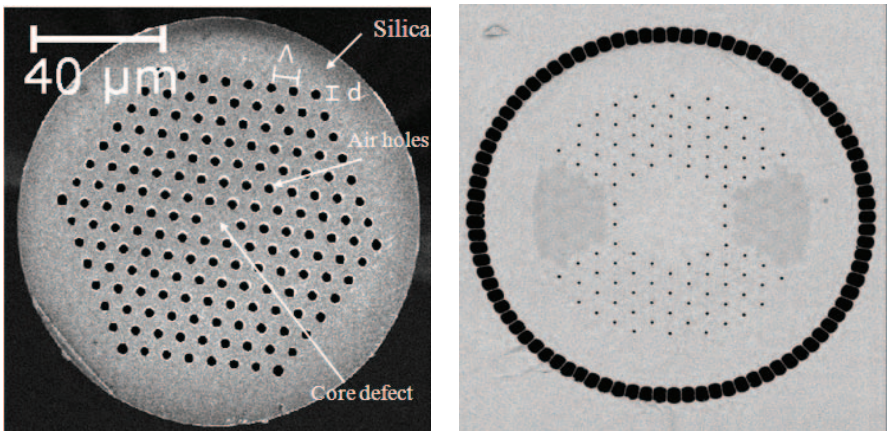

(a) (b)

Figure 2.4: (a) SEM image of solid core PCF. (b) SEM image of air-clad PCF.

under SM operation over all optical wavelengths if $d/\Lambda < 0.4$ [35]. This endlessly SM behavior can be explained by the modal filter or modal sieve experienced by the core light produced by the array of air holes [34]. The fundamental transverse mode with a lobe dimension of $\sim 2\Lambda$ fits into the core but cannot escape through the gaps between the air holes. On the other hand, HOMs have much smaller transverse lobe dimensions and can leak away from the core through gaps between the air holes. When the diameter of the air holes is increased, gaps between them becomes smaller, less higher modes can leak away from the core [34] and it is possible to confine more HOMs in the core. However, PCFs with a $d/\Lambda > 0.45$ can still be SM. The only caveat is that a cut-off wavelength is established, and like conventional step-index fibers the fiber appears to

have both multi mode (MM) and SM regimes of operation depending on the wavelength of propagated light [16].

PCF technology can be used to manufacture double-clad fibers by placing a ring of closely spaced air-holes in the outer cladding. One example of this type of fiber structure is shown in Fig. 2.4(b). This fiber structure has 19 missing holes in the core region, stress applying parts (SAPs) comprised of Boron doped silica on both sides of the core in the cladding which contribute to the polarization maintaining properties of the core and a ring of air-holes confining the cladding. The NA of the air-clad is defined by the width of the silica bridges between the air holes [32]. However, even though a high NA is preferable PCFs are typically designed to support an NA of $\sim$0.55 – 0.6 due to the difficulty encountered when cleaving fibers with larger NAs and thinner silica bridges [36, 37].

2.3.1 Photonic bandgap fibers

A PBG fiber is typically PCF with a cladding structure consisting of high index inclusions which guide the light through the photonic bandgap effect. The guiding mechanism can be explained by the formation of photonic bands and bandgaps or by anti-resonant scattering [38, 39] and has been referred to as an antiresonant reflecting optical waveguide (ARROW) [40, 41]. A cladding structure with high index inclusions supports a number of discrete optical modes with which light from the core can couple. The coupling between the core and cladding modes is due to a power transfer between them, and due to the discrete nature of the cladding modes this only occurs at certain wavelengths, i.e., the core only guides light within certain wavelength bands. In the ARROW waveguide, the light can escape from the core at the resonance wavelengths but between the resonances the light is reflected back and thereby confined by the core.

2.4 Rod type fibers

Up to 100 μm core diameters can be manufactured using PCF technology [17, 18], providing nearly SM operation. The fiber design is no longer flexible due to the very large core and extremely low NA $\sim$ 0.01. These very large core fibers are commonly referred to as rod type fibers due to their physical size and shape and to the fact they cannot be bent. Figure 2.5 shows an end view of a standard SM step-index fiber together with a SEM image of rod type fiber with a core diameter of 100 μm. Both pictures are in the same scale and the rod type fiber has an effective core

area (A_{eff}) of $\sim 6000\ \mu m^2$, which is over 200 times more than the standard step-index fiber. The rod fiber utilizes an air-clad design giving a large NA to the pump, and when combined with high core absorption the typical application length can be as short as 70 cm, which is useful in mitigating non-linear effects. Such a large core can be operated at significantly high peak powers and pulse energies without reaching non-linear effect threshold levels. The amplification of signal light and the gain properties of active fibers is discussed more in Chapter 3.

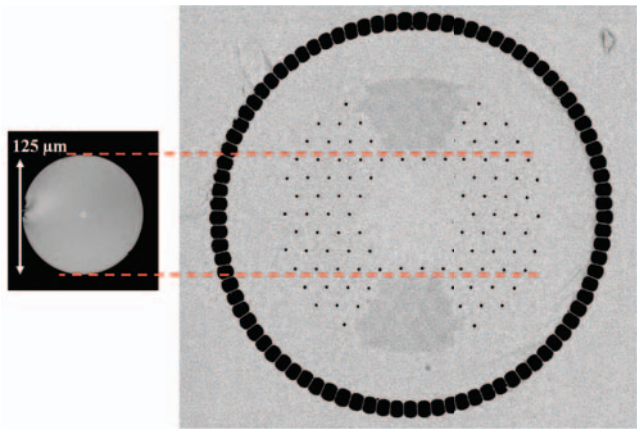

Figure 2.5: End view of a standard SM step-index fiber (left) and SEM image of a rod type fiber with a core diameter of 100 μm (right).

2.4.1 Large pitch fiber

A large pitch fiber (LPF) is a new type of PCF rod fiber with improved SM guidance within core diameters up to 130 μm [21, 42–44]. The core of the fiber is confined by only two rings of air holes in the cladding structure and operates via modification of TIR. The improved SM properties are achieved by delocalizing the HOMs in the core as well as providing preferential gain for the FM [45]. This structure results in high mode discrimination with only moderate degradation of beam quality of the FM [21]. The LPF design is proven to work under high power operation and provides SM operation; however, extremely high tolerance limits are necessary for manufacturing. The refractive index of the core and the cladding has to be matched with less than $5{\cdot}10^{-5}$ accuracy in order to maintain the SM operation and acceptable beam quality from the fiber with mode field diameters (MFDs) of 100 μm and beyond [42].

2.5 M^2 parameter

The M^2 parameter, also referred to as the beam quality factor, is commonly used to measure the beam quality of a laser beam. It can be defined by the half-angle beam divergence θ in following relation,

$$M^2 = \theta \frac{\pi w_0}{\lambda} \tag{2.5}$$

where λ is the wavelength and w_0 is the beam radius at the beam waist [22, 23]. The M^2 parameter is a metric used to define how closely a measured beam behaves compared to an ideally diffraction-limited Gaussian beam with a Gaussian intensity profile along the beam cross-section, which has the M^2 parameter of 1. The M^2 parameter is calculated by measuring the evolution of the beam radius along its axis of laser propagation and limits how tightly a laser beam can be focused given a converging optical element. The M^2 parameter is widely recognized by the industry as the main method of describing the beam quality of a laser source. However, it has been shown, that a low M^2 parameter is not a guarantee of SM operation [24]. Actually, an output beam with a M^2 value less than 1.1 can still show significant HOM content [24]. Therefore, new modal characterization methods which can resolve the modal weight and content of an output beam of a laser source or a fiber such as spatially and spectrally resolved (S^2) and cross correlated (C^2) imaging have been developed. Both of these characterization techniques are introduced in Chapter4 where experimental results obtained utilizing both techniques are also reported.

2.6 Summary of chapter 2

In this chapter an introduction to the basic properties of optical fibers was given. The step-index fiber, PCF, PBG fiber, and LPF were shortly described and the guiding mechanic for each fiber design was explained. Finally, the M^2 parameter, a metric used to determine beam quality, was described as well as the motivation why new modal characterization methods are required.

Chapter 3

Fiber lasers and amplifiers

Doping of optical fiber with rare earth (RE) ions started with erbium (Er) driven by the telecommunications industry, and has been an existing technology for decades [4]. In 1987, the first modern Er-doped fiber amplifier was demonstrated [46]. However, power scaling of Er-doped fibers has proven to be difficult due to concentration quenching and homogeneous up-conversion [47, 48], but still relatively high output power levels have been demonstrated; 67W [49] output was achieved with Er alone and 151 W output was achieved with co-doping with ytterbium (Yb) [50]. However, Yb ion doping, offers much better power scaling capabilities even though Yb-doped fibers are not fully free from limitations such as concentration quenching. Development of Yb ion doping gained significant attention during the 90's and soon become the most dominant fiber type involved in power scaling efforts of fiber lasers [51, 52].

Fiber based systems have been competing with much more mature technologies such as CO_2 and solid-state laser technologies, especially in the area of material processing. Today fiber based systems are rapidly replacing them. The fast development of fiber based systems, especially power scaling due to, among other things, significantly better thermal management compared to solid-state lasers, has resulted in record breaking output powers [7, 8, 53, 54]. Fiber based systems typically offer low running costs, a small footprint, easy beam delivery with high beam quality and high efficiency. Therefore, in many applications like marking, cutting and welding of various materials fiber based systems are widely used.

This chapter gives an introduction to fiber lasers and amplifiers. Only Yb-doped fiber systems are considered and their advantages and

disadvantages are described. Different operational conditions and power scaling capabilities and limitations of fiber lasers and amplifiers are discussed.

3.1 Fiber lasers

A fiber laser works as a wavelength and brightness converter, i.e. low brightness pump light from multi mode (MM) pump diodes is converted to a high brightness single-mode (SM) output, usually at a longer wavelength. The concept of using a fiber as the gain medium of a laser cavity was demonstrated as early as 1988 using a neodymium doped double clad fiber [55, 56]. In the case of double clad RE-doped fibers it is typical that pump light is coupled to the cladding and the core of the fiber is doped with RE ions. The pump light has an overlap with the core and thereby is absorbed by the core, energizing RE ions to an excited state. The RE ions will then emit light at longer wavelengths with lower photon energy by spontaneous emission. When a feedback is provided to the laser cavity and the gain, introduced by the active ions, compensates for the cavity losses it is possible for the cavity to lase by stimulated emission [57]. A double clad fiber, by the simplest form can act as a laser cavity when fiber Bragg gratings are written into the core to provide the cavity feedback necessary for lasing, as illustrated in Fig. 3.1

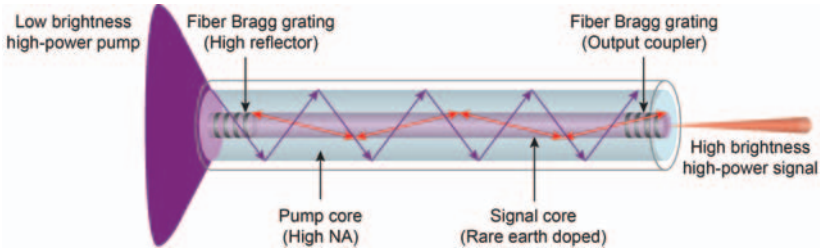

Figure 3.1: A double-clad fiber laser. The cavity is formed using a Bragg gratings providing necessary feedback back to the cavity.

3.1.1 Continuous wave operation

A continuous wave (CW) fiber laser is typically constructed by using an active double clad fiber and a pair of fiber Bragg gratings, which both form the cavity and lock the lazing wavelength, illustrated in Fig. 3.1. CW fiber lasers can typically be operated without non-linear effects limiting their power scaling and record high average powers have been

shown [7]. The only limiting case for power scaling efforts of CW fiber lasers is single frequency operation, where simulated Brillouin scattering (SBS) will limit such efforts. Power scaling is driven by both the development of cheaper high power MM pump diodes [58], optical components such as combiners [59] and of course development of the optical fibers themselves. Large brightness enhancement close to 6 orders of magnitude is easily achieved with cladding pumped fiber lasers having a SM core and large outer cladding diameter with high numerical aperture (NA) [50, 60]. Over kilowatts of average output powers have been reported [7] and commercial products reaching up to 10 kW with a SM output are available, one for example by IPG Photonics [61]. 10 kW fiber lasers produced by IPG Photonics operate in a regime where the quantum defect is greatly reduced, lowering thermal load via the tandem pumping scheme [62]. In tandem pumping, an Yb-doped fiber laser is pumped at 1018 nm and the signal is emitted at 1070 nm, giving roughly half of the quantum defect than in typical diode pumping schemes at 915 nm or 976 nm.

3.1.2 Q-switching: ns pulse generation

Q-switching can be realized in fiber lasers fairly easily by simply modulating the cavity loss using either passive or active Q-switching methods. The minimum pulse duration is defined by the decay time of the cavity and fiber lasers with pulses up to hundreds of ns in duration have been reported [7]. The maximum extractable (available) energy from the fiber laser has been shown to be around ten times the saturation energy [63]. The available energy scales with the active area of the core and with very large core fibers (135 μm core diameter) 25 mJ/m can be extracted [64]. Q-switching offers high pulse energy generation from a fiber laser design but it lacks capabilities to meet the demands for temporal pulse shaping. Therefore, many fiber lasers are constructed using a so called master oscillator power amplifier (MOPA) structure, where a low power directly modulated diode laser or an externally modulated CW fiber laser is amplified. The MOPA structure is described in detail later in Subsection 3.2.2.

3.1.3 Mode locking: ultrashort pulse generation

In mode-locking, the phase of the various frequency modes of the laser cavity are locked, resulting in the generation of extremely short pulses. These mode-locked pulses are phase coherent, which in generally is not the case in Q-switching. Yb has a broad emission cross section

of ∼100 nm, and therefore it can support generation and amplification of ultra short pulse down to tens of femtoseconds, and 36 fs pulse generation from an Yb-doped fiber laser has been reported [65]. Ultrashort pulses can be generated either with passive mode-locking using a saturable absorber, the typically method for generation of $<$ ps pulses, or active mode-locking by periodic modulation of the intracavity resulting ps pulses with a high repetition rate. Semiconductor saturable absorber mirrors are widely used for passive mode-locking [66] due to favorable properties such a self-starting, stability and reliability.

3.2 Power scaling

Power scaling of fiber lasers has developed rather quickly due to the excellent properties of Yb such as the ion's low quantum defect and the ability to create gain medium with high doping concentrations resulting high pump absorption per unit length. Laser amplification technology has had the benefit of maturing quickly over the last few years, and a fiber laser can be further power scaled using a fiber amplifier. Several amplifier stages can be used in series, each of them having unique fiber designs and the whole system can in most cases be made monolithic.

3.2.1 Fiber amplifier

A fiber amplifier is an optical fiber based device in which the core is doped with RE ions. Typically, low brightness pump light is injected into the cladding of the fiber, or in the case of core-pumped fibers SM pump light is injected into the core. Also, the signal to be amplified is injected into the fiber core. The pump light energizes RE ions inside the core to the excited state from where they will either naturally decay or amplify the input signal by the stimulated emission, illustrated in Fig. 3.2.

3.2.2 Master oscillator power amplifier structure

In one example of a monolithic master oscillator power amplifier (MOPA) fiber laser configuration, a master oscillator is formed with a pair of fiber Bragg gratings directly written in the core of a gain fiber pumped with high power diodes, typically into the cladding. The gratings create a cavity that generates light at the signal wavelength that is sent into the power amplifier. The pump power from the pump diodes can be used to pump both the master oscillator and power amplifier, as illustrated

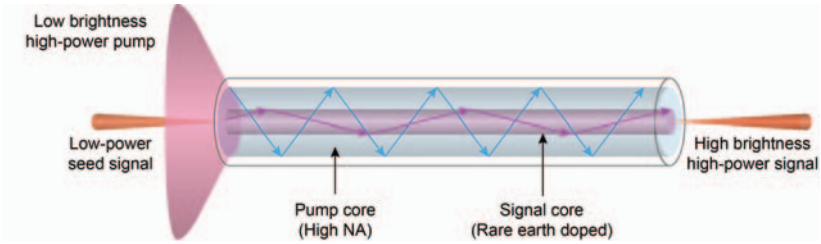

Figure 3.2: A double-clad fiber amplifier. A seed signal is injected into the core of the fiber and high power pump light into the cladding. The signal is amplified as it travels along the fiber due to the stimulated emission.

in Fig. 3.3. High output power levels can be reached with fairly simple, low-part-count, monolithic designs and thermal management is easy e.g. due to the low number of splices and optical components in the system.

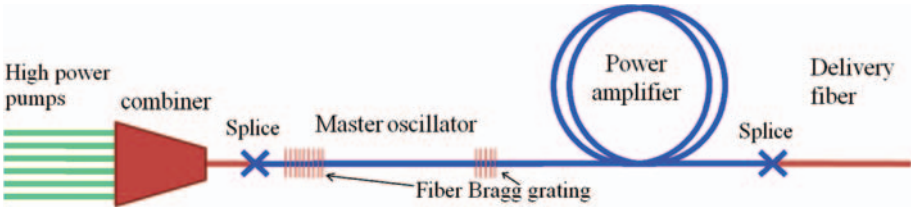

Figure 3.3: A double cladding monolithic MOPA fiber laser configuration. A fiber laser (master oscillator) is formed with the two fiber Bragg gratings written directly in the core. This is followed by a power amplifier. Both the master oscillator and power amplifier are pumped with the same pump diodes.

3.3 Limitations of fiber lasers and amplifiers

3.3.1 Gain saturation

A laser medium cannot maintain a constant gain for arbitrarily high input signal. It would require the material to possess an arbitrary amount of gain which is not physical. Therefore, extractable gain is reduced for high input signals, which is called gain saturation. The stored energy, which is proportional to the number of excited ions in the gain medium, determinates the available gain. As the excited ions posses a certain lifetime and decay time, the gain has a some finite response [67]. For a low-gain laser amplifier or laser the saturation power of the signal $P_{S,sat}$

is defined as [11, 51]

$$P_{S,sat} = \frac{\hbar\nu_s}{(\sigma_{em} + \sigma_{abs})\tau} A, \tag{3.1}$$

where σ_{em} and σ_{abs} are the emission and absorption cross sections, respectively. $\hbar\nu_s$ is the signal photon energy, τ is the lifetime of the excited state, and A is the active core area. Like gain saturation, the pump absorption can also saturate as the density of the ions in the ground state becomes depleted. The pump saturation $P_{P,sat}$ is defined by [11, 51]

$$P_{P,sat} = \frac{\hbar\nu_p}{(\sigma_{em} + \sigma_{abs})\tau} \frac{A}{G}, \tag{3.2}$$

where $\hbar\nu_p$ is the pump photon energy, G is the geometry factor for the cross section of the pump light. For single-clad, core pumped fiber lasers $G \approx 1$ and for double clad fiber lasers $G = (\frac{R_{core}}{R_{cladding}})^2$, therefore the double clad fibers offer much high pump saturation power.

Due to the high gain provided by Yb-doping a signal can experience a gain of tens of decibels per amplification stage. However, the gain can be also limited by an amplified spontaneous emission (ASE). ASE originates in active medium operating with high gain from luminescence caused by spontaneous emission, which can be further amplified to high power levels within the fiber via stimulated emission. ASE reduces the gain available for the signal and increases the noise generated by the amplifier. However, ASE can be reduced when the fiber amplifier is operated at a lower gain level by optimizing the fiber length or by using special fiber designs to suppress it or using using bandpass filters.

3.3.2 Thermal lensing

Thermal lensing is caused by the thermal load in the active medium which modifies the refractive index of the material, eventually affecting the beam quality. Typically the gain medium is hotter along the axis of propagation of the signal, causing a transverse gradient of the refractive index towards the outer surfaces of the material. As a result, the material may experience a thermally induced mechanical stress [68].

Yb-doped fiber lasers are largely immune to thermal lensing due to the excellent heat dissipation properties of optical fibers and having a large surface-to-volume ratio. However, significant heating of the fiber still occurs due to the quantum defect associated with the gain medium in high power operation. In general, for fibers the thermal lensing is not the main limiting factor of power scaling efforts but when the core size gets very large and the thermal load is extreme the thermal lensing starts to play important roles [69].

3.3.3 Photodarkening

Photodarkening can be described as a loss mechanism in Yb-doped glass through which the glass experiences a decreased transmission for the signal light propagating in the core [70] and thereby introduces larger thermal load. The physical origin of the mechanics behind photodarkening is still under debate and many theories have been posited, such as color center formation [70–75]. Photodarkening was considered one of the imminent threats of future power scaling efforts of fiber lasers and amplifiers, especially in their reliability, but new co-dopants such as Al, Ce or P have shown significant photodarkening resistance in fibers [76, 77].

3.3.4 Non-linear effects

The peak power of an amplified pulse is generally the limiting factor of ultrashort pulse amplification due to non-linear effects such as stimulated Raman scattering (SRS) and SBS, self phase modulation (SPM) and four-wave mixing. The standard step-index fiber widely used in telecommunications networks has a SM core diameter of 6 μm and a cladding diameter of 125 μm resulting an effective core area (A_{eff}) of $\sim$ 28 μm^2. Such a small effective area will enhance non-linear effects such as SRS, which is caused by scattering of signal photons by the molecular structure within optical fiber. The threshold power $P_{Raman}(th)$ is estimated by [78],

$$P_{Raman}(th) \approx \frac{16 \cdot A_{eff}}{g_R \cdot L_{eff}}, \tag{3.3}$$

where L_{eff} is the effective length of the fiber and g_R the Raman gain. Stimulated Brillouin scattering is also enhanced in fibers with small effective areas in much the same way, and the threshold power of $P_{Brillouin}(th)$ is estimated [78],

$$P_{Brillouin}(th) \approx \frac{21 \cdot A_{eff}}{g_B(\Delta\nu) \cdot L_{eff}}, \tag{3.4}$$

where $g_B(\Delta\nu)$ is the Brillouin gain which depends on the laser signal linewidth $\Delta\nu$. The Brilloin wave is generated when a high intensity signal generates an acousto-optical wave in the fiber. The refractive index of the fiber is modified by the acousto-optical wave, creating a grating which reflects the signal light in the direction opposite of signal propagation. SBS is the limiting factor for narrow signals (single frequency operation) but with broader signals SRS becomes the dominant limit of output power.

The Kerr effect causes a non-linear phase delay with the same geometric shape as the propagating optical intensity, resulting in a non-linear change of the refractive index and therefore spectral broadening of the pulse through self phase modulation (SPM). A pulse having a time-dependent power profile $P(t)$ generates the non-linear phase $\phi(t)$ across the pulse which can be defined as [2, 7],

$$\phi(t) = \frac{n_2 k}{A_{eff}} P(t) L_{eff}, \tag{3.5}$$

where n_2 is the second order non-linear index of refraction of the core, A_{eff} the effective area and the wave number $k = 2\pi/\lambda$. Assuming a logarithmic gain G per unit length of the fiber L, the L_{eff} can be written as [7],

$$L_{eff} = \frac{1}{G}(1 - e^{-GL}). \tag{3.6}$$

The non-linear phase inversely scales with the effective area of the core and therefore by using large mode area (LMA) fibers peak powers up to 1 MW has been demonstrated [15], even higher peak powers have been reported using rod type fibers, up to multi-megawatts [20].

Four-wave mixing occurs if at least two frequencies components propagate in an optical fiber and as they modulate the refractive index two new frequency components are generated. Four-wave mixing can cause significant spectral broadening of pulses in fiber amplifiers which is unwanted but when enhanced it can be used for supercontinuum generation.

3.4 Summary of chapter 3

In this chapter the basic principles of fiber lasers and amplifiers were given. The power scaling capabilities, including a discussion of the different ways to pursuit higher output powers with fiber based systems. The limitations of fibers lasers and amplifier caused by gain saturation and non-linear effects were also described.

Chapter 4

Modal analysis of photonic crystal fibers

Ytterbium (Yb)-doped large mode area (LMA) fibers have attracted many new applications both in the scientific and industrial worlds. The demand for higher output powers has pushed fibers toward having a larger and larger effective core area (A_{eff}) to mitigate non-linearities. With increasing A_{eff}, fibers easily support an increasing number of higher order modes (HOMs), which limits the pointing stability and spatial manageability of the output beam. Photonic crystal fibers have unique properties compared to standard step-index LMA fibers through, for example, better index control, and can be engineered to suppress or not guide HOMs [16, 36]. However, even though a fiber can be designed to provide single-mode (SM) operation, experimental methods to prove it are rare, especially for LMA fibers.

The criterion for SM operation is, according to the ANSI/TIA-455-80-C standard, that the HOMs present should be suppressed by more than 19.3 dB below the fundamental mode (FM) while the fiber is coiled with a 28-cm diameter, which is typically measured via the bent reference cut-off method [79]. This standard describes how to measure the cut-off wavelength of un-cabled SM fibers by the transmitted power and is generally accepted in the field of optical fibers as the common method of quantifying whether a fiber is SM. However, the cut-off method has been proven to be difficult for LMA photonic crystal fibers (PCFs) due to the low numerical aperture (NA) of the core and the strong wavelength dependence of that NA, which for example gives rise to a short-wavelength bend-loss edge in PCFs [80]. Therefore, new characterization methods that can analyze the modal content of fibers are under development and a few methods have already been shown to

work.

Spatially and spectrally resolved (S^2) imaging described by Nicholson et al. [81, 82] spatially resolves propagating modes and their relative intensities. This method can be directly applied for measuring the power difference between the FM and HOMs and has been demonstrated with both standard step-index fibers and PCFs [25, 82–86]. However, the method has its limitations and therefore using it especially with very large core fibers is challenging, due to the requirements of broad or tunable sources around 1 μm which are not widely available but necessary to detect a high number of spectral beatings. Another modal characterization method, cross correlated (C^2) imaging introduced by Schimpf at al. [26], relies on interference of the modes in a test fiber and a reference arm and thereby is free of the limits of S^2 imaging.

This chapter describes the two modal characterization methods, S^2 and C^2 imaging. An S^2 imaging setup is built and calibrated using the reference cut-off method. After calibration the SM properties of an ytterbium (Yb)-doped PCF is evaluated using various input coupling conditions, e.g. offset input coupling to deliberately excite HOMs. In Section 4.2, C^2 imaging is described and its advantages over S^2 imaging are discussed. A C^2 imaging setup is utilized to examine a passive SM PCF rod fiber (85 μm core diameter) and the guiding dynamics of the rod fiber are analyzed.

4.1 Spatial and spectrally resolved imaging

Two or more modes propagating in an optical fiber form a spatial and spectral interference pattern if the modes have different group velocities. The spatially and spectrally resolved (S^2) imaging method analyzes this interference pattern and can detect small quantities of HOMs as they interfere with the FM. No prior knowledge of the fiber properties are required to fully quantify the modal shape of the different modes and their relative intensities and phases [81]. Two electrical fields (a FM and a HOM) $E_1(x, y, \omega)$ and $E_2(x, y, \omega)$ that propagate in an optical fiber are related in the following way

$$E_2(x, y, \omega) = \alpha(x, y) E_1(x, y, \omega) \tag{4.1}$$

where $\alpha(x, y)$ is assumed to be constant and independent of the wavelength at a given position. The field is propagated assuming the group delay difference between the modes is independent of frequency,

$$E_2(x, y, \omega) = \alpha(x, y) E_1(x, y, \omega) exp(-i\omega\Delta\tau_b), \tag{4.2}$$

where τ_b is the relatively group delay between the two modes. The spectral intensity pattern caused by interference between the two fields is then [81]

$$I(x, y, \omega) = I_1(x, y, \omega)[1 + \alpha^2(x, y) + 2\alpha(x, y)cos(\omega\Delta\tau_b)]. \tag{4.3}$$

The Fourier transform of the spectral intensity pattern is

$$F(x, y, \tau) = (1+\alpha^2(x, y))F_1(x, y, \tau)+\alpha(x, y)[F_1(x, y, \tau-\tau_b)+F_1(x, y, \tau+\tau_b)] \tag{4.4}$$

where F_1 is the Fourier transfer of the optical spectrum of a single mode. Then the ratio $f(x, y)$ of the two modes with group delay of τ_b and 0 can be defined

$$f(x, y) = \frac{F(x, y, \tau = \tau_b)}{F(x, y, \tau = 0)} = \frac{\alpha(x, y)}{1 + \alpha^2(x, y)} \tag{4.5}$$

and finally $\alpha(x, y)$ can be written as

$$\alpha(x, y) = \frac{1 - \sqrt{1 - 4f^2(x, y)}}{2f(x, y)}. \tag{4.6}$$

The total intensity of each mode is the integral over the entire measurement wavelength range. The relative power of the HOM to the FM can be written as

$$MPI = 10log\frac{\int\int I_2(x, y)dxdy}{\int\int I_1(x, y)dxdy}, \tag{4.7}$$

where I_1 and I_2 represent the intensity distribution of the FM and the HOM, respectively. If $\alpha(x, y)$ and τ_b are frequency dependent, Fourier integrals can be applied to Equation 4.5

4.1.1 Measurement setup

The experimental setup is shown in Fig. 4.1. An Yb-doped amplified spontaneous emission (ASE) source consisting of three core-pumped stages gives a stable and SM broadband seed signal spectrum between 1040 and 1070 nm. This is used to seed a test fiber and generate interference patterns so that S^2 imaging measurements can be performed. The ASE source is free-space coupled into the test fiber and the study of the modes of the fiber can be achieved by offsetting the input beam and deliberately exciting HOMs. The test fibers are polarization maintaining, and a polarizer is used to launch the light along the slow polarization axis of the test fiber. The orientation of the slow axis in this study is defined as the horizontal plane parallel to the optical table and the

stress rods are oriented in the horizontal plane. The test fibers are coiled to a specific coil diameter along the x-axis. The near-field (NF) of the test fiber is imaged onto a SM fiber (HI1060) probe with a simple lens pair with magnification of roughly 13 x. The fiber probe is mounted on motorized stages to ensure quick and accurate movement within the cross-sectional area of the output beam and is connected to an optical spectrum analyzer (OSA). The scanning time of one full measurement consisting of a 31 x 31 matrix is limited by the speed and spectral resolution of the OSA. A polarizer at the output side is used to align the polarization of the modes along the same polarization axis.

A mathematical routines developed in Matlab are used to ana-

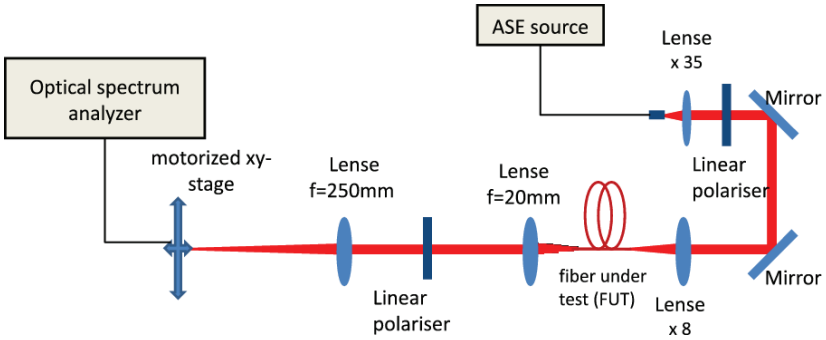

Figure 4.1: Experimental S^2 imaging setup.

lyze the captured spectral traces and calculate the HOM suppression measured with S^2 imaging. In the data analyzed, all the measured spectra are converted to frequency, then interpolated and resampled to get equal sample spacing. The spectra are then remodulated by a Hamming sampling window in order to reduce sample-related broadening, which increases the effective resolution of the fast Fourier transforms (FFTs).

4.1.2 Calibration of the S^2 imaging setup

The mathematical routines used when a S^2 imaging measurement is analyzed were numerically calibrated by constructing an S^2 emulator using simulated modes. A commercial finite-element-solver (JCMWave GmbH, Berlin, Germany) was used to simulate the modal fields and propagation constants. In these simulations the stress distribution from the stress elements was included. The simulated modes were propagated along the fiber and the spectral interference pattern at each of the spatial measurement points was calculated. Figure 4.2(a) shows the simulated intensity profile after propagating a LP01 and LP11 mode in the PCF when the HOM (LP11 mode) content is 100 times weaker than the

FM. The Fourier transform of the optical interference spectrum at one

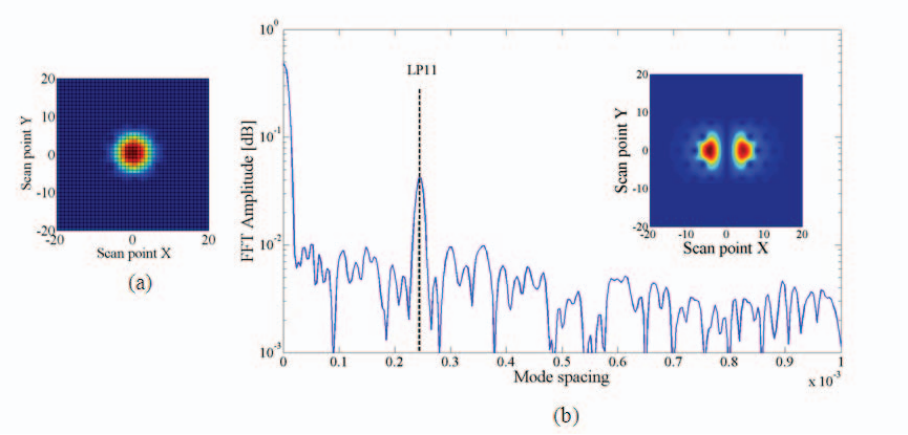

Figure 4.2: (a) Simulated intensity profile of the FM and a weaker HOM (100x) after traveling through a PCF with a 40 μm core diameter. (b) Example Fourier transform, shown as a function of mode spacing, which is defined by the effective index difference between the interfering modes, and reconstructed intensity profile of the LP11 mode suppressed by 20 dB.

spatial point of the simulated intensity profile is shown in Fig. 4.2(b). The Fourier spectrum is shown as a function of mode spacing, which is defined by the effective index difference between the interfering modes. The mode spacing is calculated using the relation $\Delta n = \lambda^2/(\Delta\lambda \cdot L)$, where Δn is the mode spacing, λ is the wavelength, L is the fiber length, and $1/\Delta\lambda$ is the frequency obtained with an FFT. The Fourier spectrum in Fig. 4.2(b), shows two spectral components at 0 and $0.23 \cdot 10^{-3}$ corresponding to the FM and the LP11 mode suppressed by 20 dB, respectively. The inset of Fig. 4.2(b) shows the reconstructed LP11 mode profile. The reconstructed LP11 mode profile is post-processed by increasing the sampling rate by simply interpolating the gray scale map index value across the image. This is done after the HOM suppression is calculated and only done to give a better visualization for the reader, and therefore does not affect the HOM suppression calculations.

In addition, the S^2 imaging system was experimentally calibrated by using a 1-m-length polarization maintaining (PM) step-index LMA fiber with 0.06 NA and 15 μm mode field diameter (MFD), illustrated in the inset of Fig. 4.3. The principle here is to use a fiber with known HOM suppression, which can be measured with a standard spectral transmission measurement and relate these results to the S^2 imaging measurements. The modal properties of the fiber were characterized in two different bent configurations and the relative power difference was measured. A

slightly bent configuration, where the HOM content was suppressed by 20 dB at 1045 nm is defined as follows. The wavelength was chosen measuring the transmission spectrum for the fiber both when it was straight and when slightly bent with a minimum radius of curvature of 65 cm. Figure 4.3 shows the relative intensity difference between the two mea-

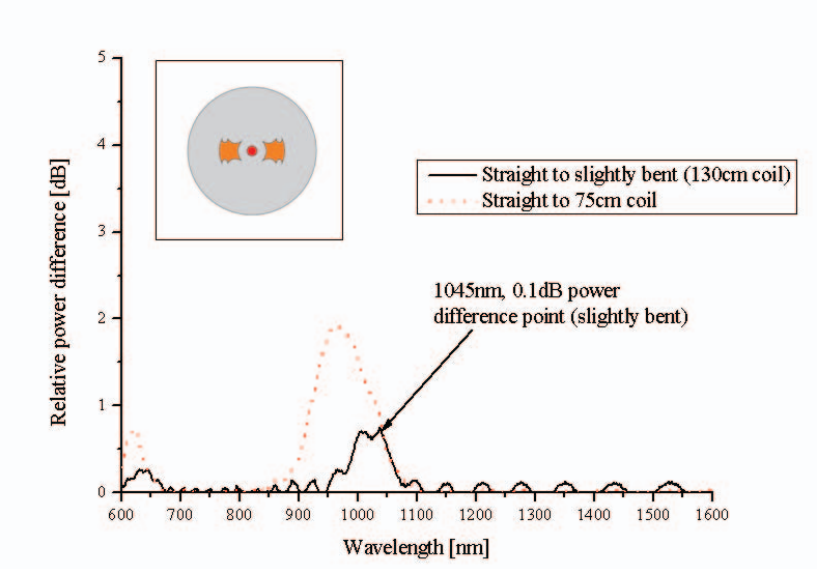

Figure 4.3: Transmission measurement of a PM step-index LMA fiber with a 0.06 NA and 15 μm MFD, showing the wavelength where the HOM content is suppressed by 20 dB. The fiber design is illustrated in the inset.

sured spectra and a 0.1-dB difference in transmission at the 1045-nm wavelength for a slightly bent configuration with a 130-cm coiling diameter (solid line). When the fiber is bent more and the coiling diameter is reduced to 75 cm (dotted line), the 0.1-dB transmission difference moves to ∼950 nm. At that wavelength, the HOMs carry 2.27 % of the power and the relative power difference (suppression) between the HOMs and the FM is then 16.4 dB. However, when the measurement was performed, the light was coupled into the fiber by overfilling the NA of the core, and thus all the supported modes were excited. Therefore, two HOMs and only one FM were excited. This means that the HOM suppression is, assuming the power is split equally between the two HOMs, 3 dB larger (i.e., 19.4 dB) and the HOM suppression should therefore be expected to be around 20 dB at the 1045-nm wavelength.

Three simulated mode profiles in the used fiber are shown in Fig. 4.4. These modes can be selectively excited by offsetting the input beam waist either along the y- or x-axis direction, exciting either LP11 mode

oriented along the y- or x-axis, together with the FM. The same finite-element-solver was used as in the earlier simulations. Several S^2 imaging

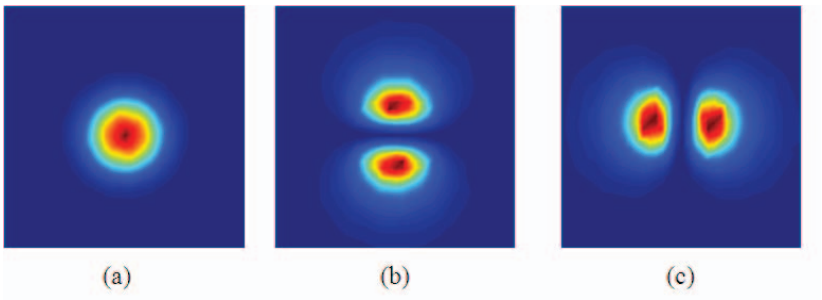

Figure 4.4: Simulated intensity profiles: (a) Fundamental mode (LP01), (b) LP11 mode oriented along the y-axis, and (c) LP11 mode oriented along the x-axis.

measurements were performed on the same fiber using three different input coupling conditions attempting to excite HOMs in a simple and repeatable way:

1. Fundamental mode coupling, input signal is coupled into the core optimizing the overlap between the input beam and the fundamental mode of the fiber

2. y-axis LP11 mode coupling, offsetting the input beam orthogonal to the stress rod elements

3. x-axis LP11 mode coupling, offsetting the input beam toward the stress rod elements.

The coupling configurations used attempt to deliberately excite significant content of the HOMs and achieve a good degree of repeatability. The y- or x-axis LP11 mode coupling condition is found by translating the input beam off center along the y- or x-axis respectively until a 3-dB power drop is measured for the FM. This power drop is measured by placing the pickup fiber in the middle of the output beam, where the modes have the lowest spatial overlap, the FM has the highest intensity and the LP11 mode has close to zero intensity. Therefore, ∼50 % of the power launched into the core is coupled to the FM and the remaining ∼50 % is coupled mainly to the LP11 modes, but also to non-guided cladding modes.

The fiber was aligned with the stress rod elements in the horizontal plane and linearly polarized broadband light between 1040 and 1070 nm was coupled to the fiber with the axis of polarization parallel to the slow

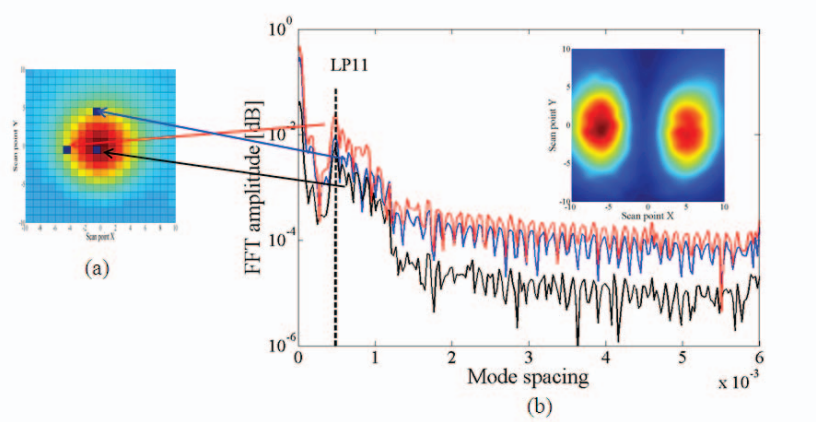

Figure 4.5: Example of the S^2 imaging measurement on a 1 m length PM LMA step-index fiber with 0.06 NA and 15 μm MFD: (a) Typical intensity profile and (b) example Fourier transforms at three different scan points, shown with dark dots on (a) and reconstructed intensity image of the LP11 mode, HOM suppression of 24.1 dB.

axis of the fiber. The measured intensity profile is shown in Fig. 4.5(a). An example of three Fourier transforms at different scan points of the measured beam are shown in Fig. 4.5(b), one calculated in the center of the beam and two at the full width half maximum (FWHM) of the beam. The Fourier transforms show a clear presence of the LP11 mode, which is identified by calculating the theoretical mode spacing between the FM and the LP11 mode. Other spectral components, after the LP11 mode peak, correspond to coupling between the FM and HOMs throughout the length of the fiber and therefore they appear as multiple peaks rather than a one single peak. This is called distributed scattering and is described in detail in Ref. [81]. The reconstructed LP11 mode is shown in the inset of Fig. 4.5(b), and the measured HOM suppression is 24.1 dB.

Figure 4.6 shows a histogram of the measured HOM suppression while varying the integration window width of the Fourier transforms when performing HOM suppression calculations, and using different input offsetting conditions. The average HOM suppression is 22.5 dB $\pm$3 dB, which agrees reasonably well with the expected value of 20 dB obtained with the bent transmission reference method.

4.1.3 Measurements on a SM LMA PCF

S^2 imaging was performed on a 2.2-m-length polarizing Yb-doped PCF (DC-200/40-PZ-Yb-03). The FM had a 29-μm MFD with an NA of 0.03 at 1064 nm. The multi mode (MM) pump cladding was 200 μm, having

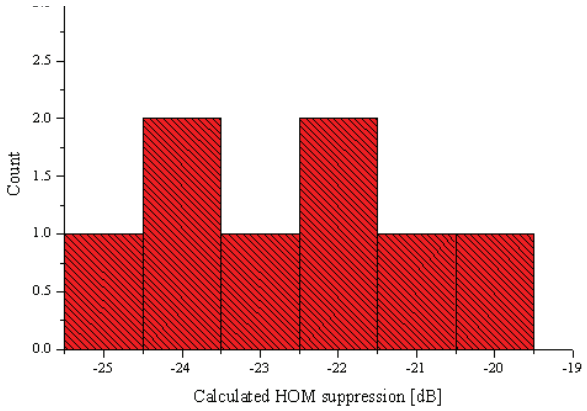

Figure 4.6: Histogram of the measured HOM suppressions obtained with S^2 imaging, while offsetting the input beam and varying the width of the Fourier integration window when calculating the HOM suppression. The average HOM suppression is 22.5 ±3 dB.

an NA of 0.6. A schematic and a micrograph image of the fiber is shown in Fig. 4.7. LMA PCFs are sensitive to bending, especially if the bending

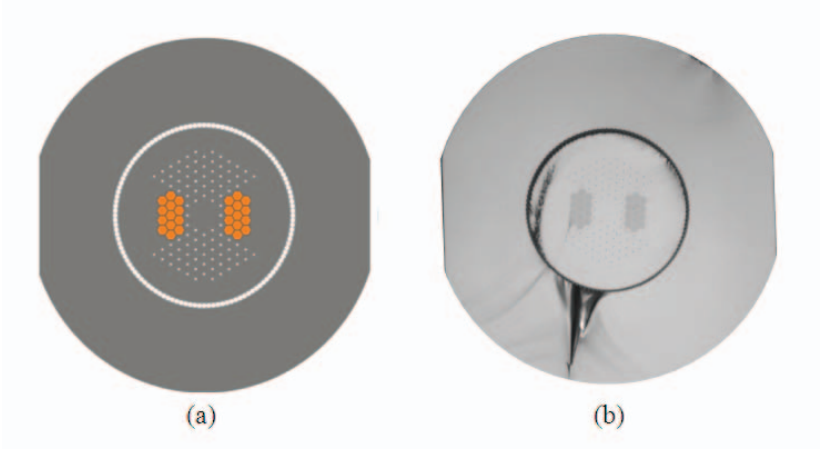

Figure 4.7: (a) Schematic of the fiber design illustrating the flat sides on each side of the stress rod elements and (b) optical micrograph picture of the fiber.

plane is not aligned with the stress rod elements [86]. The flat sides of the outer fiber structure, shown in Fig. 4.7, will automatically orient the fiber along the stress rod axis, thus avoiding twist while coiling the fiber. In addition, because the fiber bend diameter is always oriented along the stress rod elements, the modal stability is increased and the

unwanted bend loss for the FM is reduced.

Low HOM content is difficult to analyze if the signal-to-noise level is not high enough (the term noise here is understood as light coupled into the cladding). Therefore, the air cladding of the test fiber was removed with a cladding mode stripper (Glycerol) over a 25 cm section at the output end of the fiber and achieved an increase in signal-to-noise level from 25 to 37 dB.

Linearly polarized light between 1040 and 1070 nm was coupled into the slow axis of the test fiber with optimized mode matching between the coupled beam and the FM of the fiber. The test fiber was coiled to a 28-cm coiling diameter and three different input coupling conditions were used, as described earlier. The measurement was repeated five

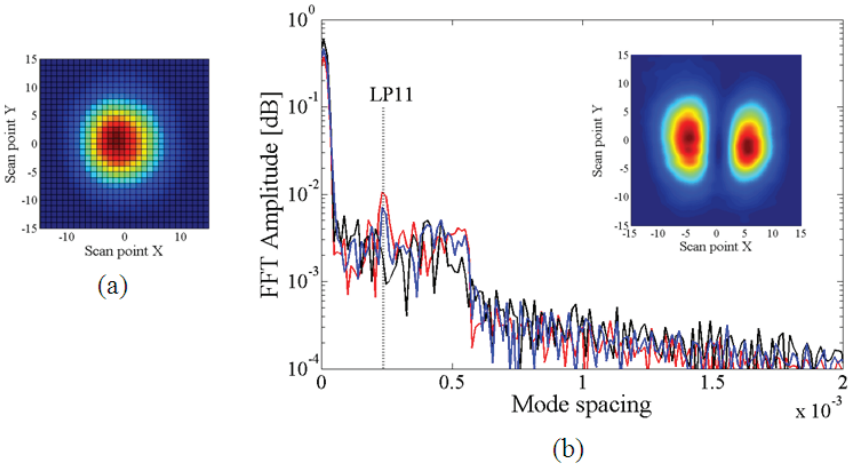

Figure 4.8: Example of S^2 imaging on a 2.2-m DC-200/40-PZ-Yb-03 having 29-μm MFD and NA of 0.03: (a) Example intensity profile and (b) example Fourier transforms at three different points at the beam, selected as in Fig. 4.5, and the reconstructed intensity image of LP11 mode, HOM suppression 24.7 dB.

times for the same fiber, and each time the fiber was recoiled and both ends were re-cleaved. Additional measurements were performed with a 40-cm coiling diameter. A typical intensity profile obtained with S^2 imaging is shown in Fig. 4.8(a). An example of Fourier transforms at three different points of the measured beam as described before is shown in Fig. 4.8(b), and the reconstructed LP11 mode is shown in the inset of Fig. 4.8(b). Only the LP11 mode has clearly observable peaks in the Fourier spectrum, and the mode spacing matches the calculated value. Other HOMs were not found, even when offsetting the input beam. However, as in the earlier experiments with the step-index fiber,

distributed scattering throughout the fiber length gives rise to the other spectral components observed after the main peak.

Table 4.1 summarizes the five S² imaging measurements performed

Table 4.1: Summary of the five S² imaging measurements on a 2.2-m-length DC-200/40-PZ-Yb-03 coiled to 28 cm diameter using three different launching conditions.

Measurement	HOM suppression (dB)		
	FM coupling	x-axis LP11 coupling	y-axis LP11 coupling
1	33.1	23.8	28.6
2	33.7	27.7	30.4
3	31.5	24.5	23.2
4	33.4	25.9	26.2
5	31.6	21.7	24.5
Average (dB)	**32.7**	**24.7**	**26.6**
STDV (dB)	**1.0**	**2.3**	**2.9**

on the fiber when the fiber is coiled to 28 cm diameter. Using the FM input coupling condition, the LP11 mode is relatively weak with an average suppression of 32.7 dB. When offsetting the input beam one lobe of the LP11 mode overlaps with the input beam and is excited. Depending on the offsetting direction, either a LP11 mode along the y- or x-axis is excited. The LP11 mode oriented along the x-axis, shown in Fig. 4.4(c), has the stress rod element barrier while the fiber is coiled, and therefore is less sensitive to bend loss than the LP11 mode oriented along the y-axis. For this reason in the case of x-axis LP11 mode coupling, the HOM suppression is smaller (24.7 dB) than with the y-axis LP11 mode coupling (26.6 dB).

One important factor when performing the S² imaging measurement is the coupling repeatability between various measurements. Even a slight error, for example, on the coupling angle will change the overlap between the input beam and the different modes in the fiber. Therefore, the three aforementioned coupling conditions were used as they seemed to give fairly repeatable results with a standard deviation of <3.0 dB.

In the last experiment, S² imaging was performed while increasing the bend diameter from 28 to 40 cm. The test fiber was the same as before and the input coupling conditions were varied. Figure 4.9 illustrates the measured HOM suppressions for the two bend diameters and three coupling conditions. The stress rod element barrier effect is

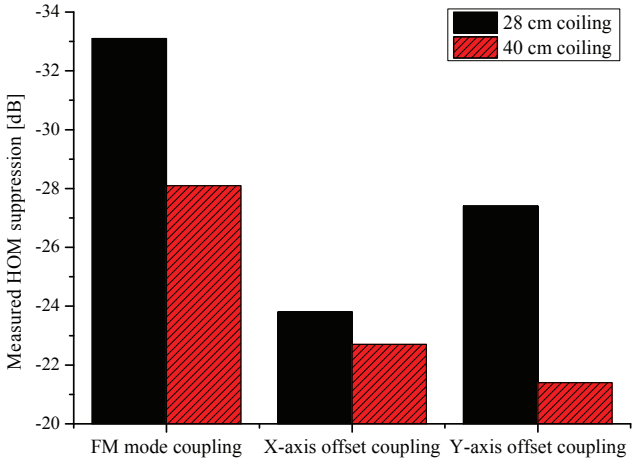

Figure 4.9: Measured HOM suppression of a 2.2-m length DC-200/40-PZ-Yb-03, using two bending diameters.

efficient for the LP11 mode oriented along the x-axis, and therefore the measured HOM suppression is lower for the both bending diameters. However, the LP11 mode oriented along the y-axis is more susceptible to bend loss, and therefore less HOM suppression is measured at the 40-cm bend diameter.

4.1.4 Discussion on measurement results

S^2 imaging is a relatively new measurement technique offering both spectral and spatially resolved data in a single measurement. Being an interferometric method, S^2 imaging is extremely sensitive and can characterize multiple HOMs simultaneously from LMA fibers, where conventional M^2 or cut-off measurements fail. However, S^2 imaging has important limitations:

- **long measurement time:** measurements often take several minutes while simultaneously requiring an extremely stable seed source, stable launching conditions and no mechanical perturbations on the fiber for the duration of the measurement process.

- **spectral interference:** typically the modes in LMA fibers with MFDs larger than 40 μm have a small inter-modal group delay. The

resulting mode spacing corresponds to a spectral beating period of 18 – 30 nm using typical fiber lengths. Since at least three to four spectral interference peaks are necessary to resolve such beating, a spectral measurement range over 100 nm is required. Stable and smooth tunable or broad band seed sources around the 1 μm region are not widely available.

- **sensitivity to a reference mode:** the method relies on a use of a reference mode, typically the FM, when the interference signal is analyzed. Therefore, a reasonable estimate of the relative power content of different modes can be obtained only if the reference mode has the highest power level, and the method fails to characterize the cases where multiple modes have similar power levels

- **assumption of negligible dispersion:** when the interference signal is analyzed the dispersion of different modes is typically neglected. However, normally the measurement is performed over a large spectral range (20 – 100 nm) and thereby the dispersion properties over the wavelength range in some cases are relevant.

- **polarization properties:** the method fails to resolve polarization states of the different modes present in the fiber.

Therefore, another modal characterization method which is free of the above limits, C^2 imaging, is described in Section 4.2 and demonstrated using a fiber with very large core diameter.

4.2 Cross correlated imaging

The C^2 imaging method relies on interference in the time domain between an external reference beam and each of the modes propagating in the test fiber as a function of the relative group delay. A major advantage of C^2 imaging arises through the freedom to independently tailor the properties of the reference beam. This affords one the ability to resolve modal content for arbitrary modal combinations of the test beam [26] as well as polarization and dispersion properties of each mode [87], which is difficult or impossible with S^2 imaging. In addition, required seed sources are inexpensive and widely available (for example LEDs), so it is not difficult to integrate a C^2 imaging apparatus with laser systems operating at 1 μm. Even though the resolution of the method is dictated by the spectral width of the seed source similar to S^2 imaging, this limitation is not as significant as it is with S^2 imaging. With C^2 imaging it

is possible to obtain excellent results using just a 10 nm spectral range and it is possible to resolve the various modes present in very LMA fibers (core diameters >60 μm).

C^2 imaging is used in this study to examine the guiding properties of passive photonic bandgap (PBG) PCF rod fiber with a very large core. The rod fiber design is based upon the idea of distributed mode filtering (DMF) [27], which results in SM and MM regimes depending on the wavelength. In the SM guiding regime within a specific wavelength range, HOMs couple resonantly to a band of narrowly spaced cladding modes. Outside the resonant coupling regime, the fiber appears either MM or does not guide light in the core. A detailed description of guiding properties and analysis of the DMF rod fibers will be shown later in Section 5.1.

In the following experiments, resonant mode coupling is resolved with C^2 imaging and is demonstrated as the underlying mechanism for SM guidance within specific wavelength ranges. SM operation is tested for various offset input coupling conditions to deliberately excite HOMs. The experiments were performed in a collaboration with Boston University, Boston, USA, using their existing C^2 imaging setup. The original setup was designed to measure only flexible fibers and therefore it was modified to be used together with rod type fibers.

4.2.1 Measurement setup

A schematic representation of the C^2 imaging system is shown in Fig. 4.10. The setup utilizes a standard Mach-Zehnder interferometer. The signal and reference paths are created with a beam splitter and consist of the test fiber and a SM PM reference fiber, respectively. Those paths are imaged onto a CCD camera at the output end of the interferometer after recombination. The interferometer has linear polarizers in both arms to ensure the reliable measurement of the modal power of elliptically polarized light transmitted through the test fiber. A linear polarizer in the signal arm defines the plane of polarization of light coupled into the test fiber. The linear polarizer in the reference path ensures coupling either to the fast or slow axis of the SM PM fiber (PM980XP). A specific length of 101 cm for the reference fiber is chosen to bring the optical path length of the reference path within the range of the translation stage used to control the relative optical path length of the beams.

A 1050 nm superluminescent SLED was used as the light source for the experiments. Wavelength tuning is achieved by filtering the source light with an angle-tunable bandpass filter with FWHM of about 10 nm.

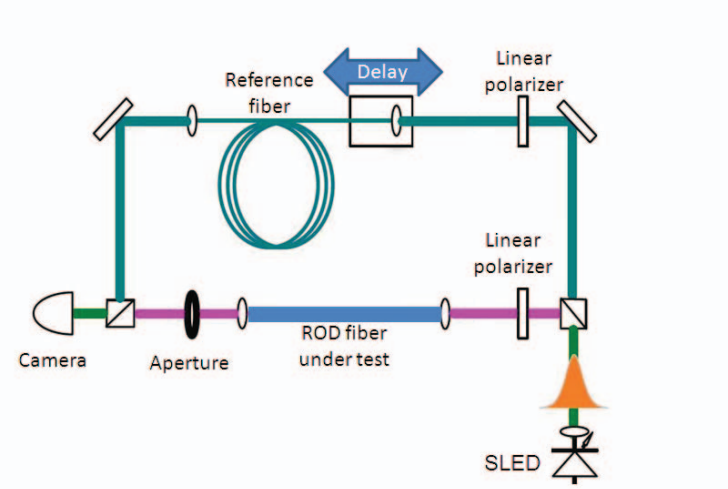

Figure 4.10: C^2 imaging setup [88].

To avoid scrambling the polarization state, the bandpass filter was inserted into the signal path before the linear polarizer. The filter has a Gaussian profile and is used at an angle corresponding to a center wavelength of 1040 nm or 1060 nm, as shown in Fig. 4.11. A NF image of the fiber under test is obtained using a single (plano-convex) lens with 50-mm focal length which images the fiber output onto a CCD camera. A reference beam is expanded to ensure flatness of the phase front within the imaging range. The beam overlaps spatially with the test fiber image at the image plane of the CCD camera located about 97 cm away from the output end of the test fiber. An adjustable aperture is inserted between the lens and the CCD camera ∼23 cm away from the lens. This aperture is used in the experiments to remove most of the cladding light. The relative group delay of the reference and the test beam is controlled by a motorized linear translation stage which changes the length of the interferometer reference arm. At each delay point, the interference pattern is recorded and cross-correlation traces are analyzed. When analyzing the cross-correlation traces, the mathematical routines and theories of C^2 imaging developed in Ref. [88] are followed.

The cross-correlation signal $P(x, y, \tau)$ recorded by the CCD camera

$$P(x, y, \tau) = \Sigma_m p_m G^2_{mr}(\tau - \tau_{mr}) I_m(x, y), \tag{4.8}$$

is a function of the position (x, y) in the imaging plane and the differential time delay τ_{mr} between each of the modes m and the reference mode r. The signal obtained is the summation over vertical

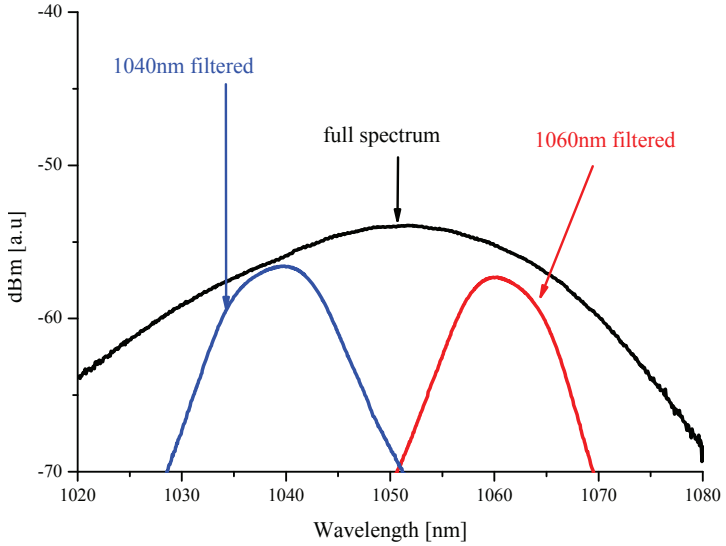

Figure 4.11: Measured input spectra for different C² imaging measurements (used pick-up fiber HI1060).

and horizontal linearly polarized states of the reference beam and accounts for the possibility of elliptically polarized modes propagating in the test fiber. The time delay $\tau = d/c$, where c is the speed of light in vacuum, is controlled by the position of the translation stage d. The stack of the images $P(x, y; \tau)$ obtained at the image plane encode the modal power p_m and the modal intensities $I_m(x, y)$, the two quantities of prime importance of the study. Detailed explanation of the C² imaging theory is shown in ref. [26]. The behavior of $G_{mr}(\tau)$, the magnitude of the coherence function, is dictated by the spectral properties of the seed source and also by the relative dispersion of mode m and the reference beam [26, 88].

Dispersive broadening of the function can be compensated for by adjusting the length of the reference fiber [26]. When the effects of dispersion are negligible, either due to dispersion-compensation or if the seed source is narrow enough to ignore dispersive effects, the mutual coherence function is characterized by a finite extent in the time domain that is inversely proportional to the spectral bandwidth of the source. This property allows one to separate the modes, when they are characterized by sufficiently large differential group delay. As a result, the modal intensity and the power of every individual mode is measured simultaneously. The modal power is encoded in the net C² trace, which is obtained by averaging the cross-correlation signal over the imag-

ing plane while taking normalization of the modal intensity into account.

4.2.2 Modeling of C^2 imaging from a DMF rod fiber

A finite-element-method solver is used to simulate the power overlap ratio in the core of the DMF rod fiber design for the most relevant modes, shown in Fig. 4.12. The simulated DMF rod fiber design has SM guidance for the wavelengths between 1022 and 1045 nm, beyond which it appears MM, supporting the HOMs. The field distributions of these modes are similar to that of a LP11 mode and thereby they are reference as $LP11_2$ and $LP11_3$ modes. The SM guidance regime is defined at the wavelengths where the FM has minimum 80 % core power overlap and therefore well guided, while the HOM has less than 50 % core power overlap. The criteria for theoretical SM guidance regime has been shown to have sufficient agreement with fabricated DMF rod fibers [89]. Figure 4.12 illustrates the simulated field profiles of the different modes in the SM and MM guiding regimes. The field profiles show how HOMs effectively couple out from the core to the resonator elements inside the cladding structure within the SM guiding regime

C^2 imaging traces for the DMF rod fiber used in the experiments were simulated to estimate the limits of resolution and understand the ability of the method to probe the modal content of this type of fiber. First, the effective refractive indices (n_{eff}s) of the modes in the DMF rod fiber were simulated. From the simulated effective refractive index (n_{eff}) the net C^2 trace in Fig. 4.13 was modeled for the rod fiber for a source with the Gaussian spectrum with a central wavelength of $\lambda = 1040$ nm and FWHM of 10 nm (spectrum shown in Fig. 4.13 inset). The rod fiber supports propagation of the FM and two HOMs, $LP11_2$, $LP11_3$ - characterized by the relative group delays and dispersion properties obtained from the simulations of the fiber design. The $LP11_1$ mode is neglected due to its low core overlap ratio at 1040 nm. The dash-dotted line represents the coherence function in the case of the ideal dispersion-compensation of all the modes.

For this simulation it is assumed that each of the HOMs contributes 1 % of the total power, which translates to 20 dB suppression of those modes, as the peak values of the dash-dotted line indicate. The positions of the peaks define the relative group delay of the modes with respect to the FM. Dispersion effects lead to noticeable broadening of the peaks, resulting in the C^2 trace shown as a solid line. Based upon a specific fiber design, the simulations for this fiber indicate that in the SM guiding regime at a center wavelength of $\lambda = 1040$ nm, an offset coupling mainly

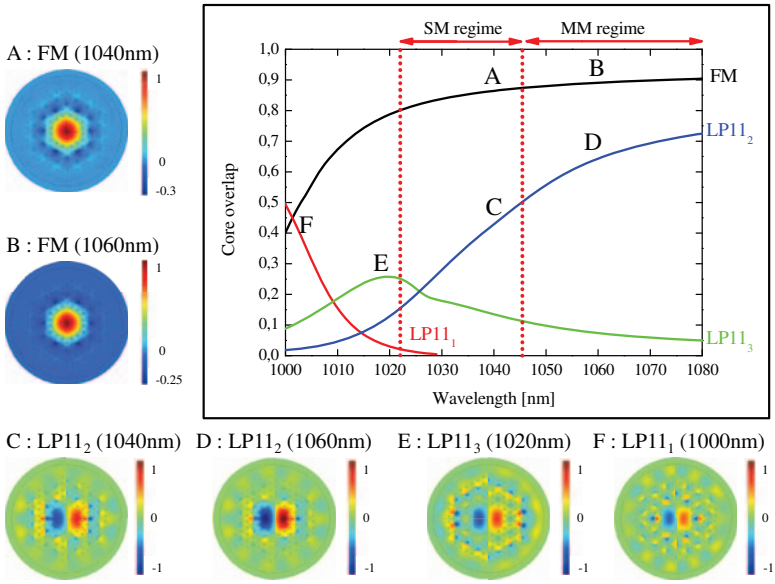

Figure 4.12: Simulated core overlap ratio (power) of different modes in the DMF rod fiber. Showing the most relevant modes and two guiding regions SM and MM. Insets illustrate the simulated electric field profiles of different modes at specific wavelengths

excites two HOMs, $LP11_2$ and $LP11_3$, with average group delay differences of ∼1.2 ps/m and ∼2.9 ps/m, with respect to the FM respectively, as shown in Fig. 4.13. At a longer center wavelength of 1060 nm, the peak representing the $LP11_2$ mode is separated by a group delay value of just ∼0.6 ps/m, as Fig. 4.14 illustrates.

In the simulations and experiments relatively narrow input spectra (FWHM = 10 nm) centered at 1040 nm and 1060 nm were specifically chosen. An input signal with wider spectral range would certainly lead to narrower and better resolved temporal features representing the HOMs, but a broader source would cover both the SM and MM regimes, confusing their relative contribution. The simulations done with Gaussian spectral profiles demonstrate that at a center wavelength of 1040 nm the $LP11_2$ mode can clearly be resolved in the C^2 imaging trace, as shown in Fig. 4.13. In contrast, at a center wavelength of 1060 nm, due to a smaller group delay the LP11 mode appears almost as a shoulder superimposed on the feature representing the FM, as seen in Fig. 4.14.

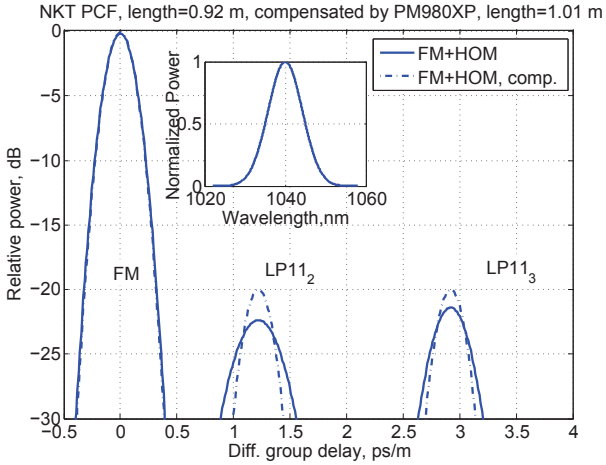

Figure 4.13: Simulated C^2 imaging trace of DMF rod fiber at 1040 nm (98 % in the FM, 1 % in each of the two HOMs): solid line represent the trace accounting for the dispersion of the modes, dash-dotted line depicts the trace with digitally compensated dispersion. Inset: Gaussian spectrum centered at 1040 nm with FWHM = 10 nm, used in the simulation.

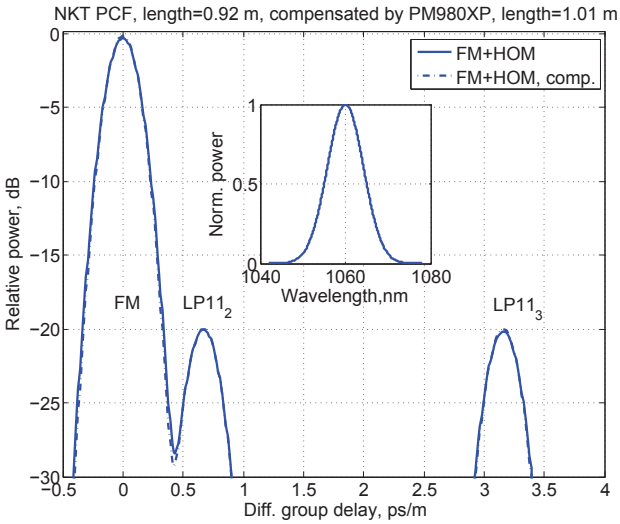

Figure 4.14: Simulated C^2 imaging trace of DMF rod fiber at 1060 nm (98 % in the FM, 1 % in each of the two HOMs)

4.2.3 Input coupling conditions

The SM operation of the DMF rod fiber is evaluated at different input coupling conditions by analyzing the corresponding C^2 imaging traces. One naturally expects that an offsetting coupling results in the appearance of HOMs in the trace, and more so as the offset is increased. To analyze these effects in the experiments, the following procedure is adopted.

1. **Optimal input coupling condition:** the position of the input-coupling lens, which a C^2 trace reveals the most SM beam is identified.

2. **Offsetting input coupling condition:** the input-coupling lens is shifted in either the horizontal or vertical direction, which is specified as $x_{\mu m}/y_{\mu m}$, where x and y stand for the horizontal or vertical direction of the offset coupling, respectively.

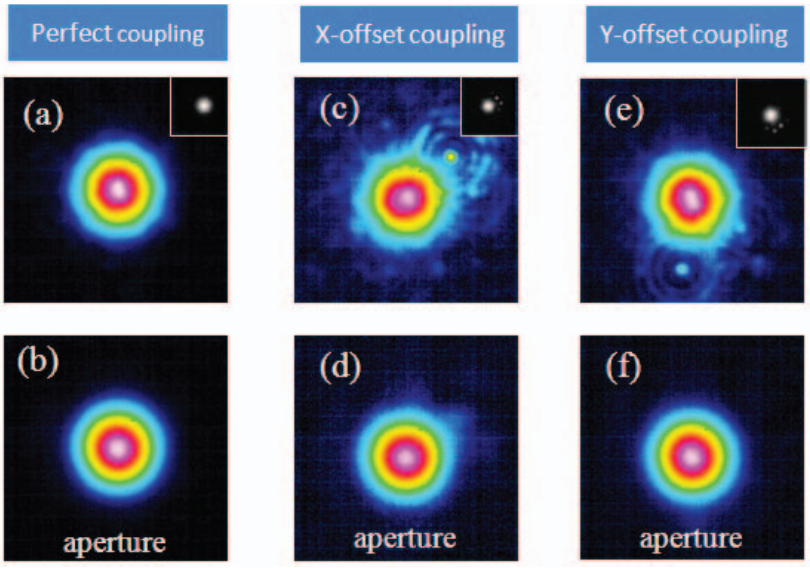

Figure 4.15: Near-field images of three different coupling conditions with and without the aperture. Inserts in (a), (c) and (e) show the images at the facet. Images recorded at the SM regime of the DMF1040.

The input coupling lens is moved by a distance (in μm), which is measured from the position of optimal input coupling. The displacement is limited to 30 μm in either direction since at larger values the input light dominantly couples to the cladding modes of the fiber and the core-to-clad intensity ratio decreases to a point that analysis of the core modes

becomes difficult or meaningless. Specifically, at the 30 μm offset coupling less than half of the light couples to the core modes of the fiber.

The fiber is characterized by special higher index resonator elements in the cladding tailored to inhibit propagation of HOMs in the core at certain wavelengths. At these wavelengths, HOMs within the core resonantly couple to the resonator elements in the cladding and are then guided through the length of the rod fiber. This is evident in the NF images of the fiber output, especially when light is coupled with an offset, as shown in Fig. 4.15 (c) and (e). Since the C^2 imaging measurements require analysis of NFs images of the output facet of the fiber this spurious effect is eliminated by inserting an aperture at the output of the test fiber in some of the measurements (e.g. when offset coupling is attempted). The aperture filters cladding light away, allowing one to accurately determine the modes present in the core. As a result, the resonant coupling between the core and the cladding band can be directly measured.

4.2.4 Measurements on a SM DMF rod fiber

The tested DMF rod fiber has a MFD of 60 μm and length of 92 cm. The end facets of the rod fiber are collapsed within ~200 μm of the flat-cleaved facet. This fiber has a single cladding structure and is designed

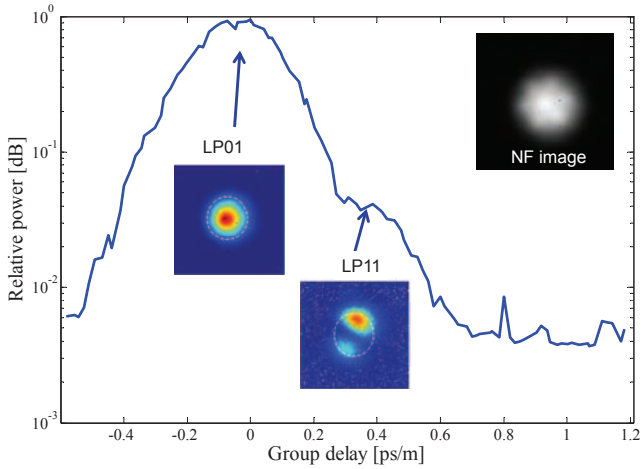

Figure 4.16: Calculated envelope function of the C^2 trace showing the total power of all the modes. The LP11 mode has 14 dB less power than the fundamental mode (LP01). The insert shows the measured NF image. The white dotted circle illustrates the core area.

and measured to be SM within the wavelength range from 1030 nm to 1050 nm. The exact boundaries of the SM regime, which are difficult to measure experimentally, are estimated with ±5 nm uncertainty. At wavelengths longer than 1050 nm the fiber becomes MM supporting HOMs in addition to the FM, which are not coupled to the cladding band. Hereafter, the term "DMF1040" is used when referring to this rod fiber.

The DMF1040, which is SM at the wavelength of 1040 nm, was first tested using a source centered at $\lambda = 1060$ nm with FWHM of 10 nm, as shown in Fig. 4.11. At this wavelength, the DMF1040 rod fiber is expected to be MM. By careful alignment of the input beam a condition in which it appeared that only the FM was excited was achieved, as the perfectly symmetric output image demonstrates in the inset of Fig. 4.16. However, the calculated envelope function of the C^2 trace in Fig. 4.16 indicates a significant contribution of and LP11 mode to the modal power. The group delay (ps/m) is calculated from the generated delay $\tau = d/c$, where d is the movement of the reference arm and c speed of light in vacuum, and normalizing with the length of the test fiber. Indeed, image reconstruction identifies that the LP01 and LP11 modes dominate light propagation in the fiber. The $LP11_3$ mode is not observed in the experiments due to its low core overlap ratio at 1060 nm.

Reconstructed images were obtained by integrating over portions of

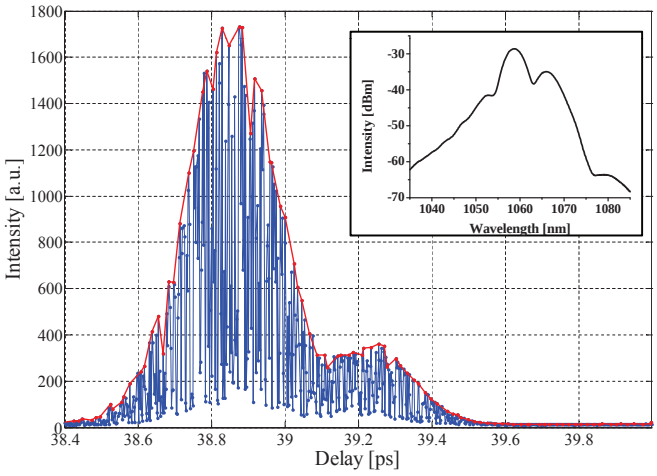

Figure 4.17: Example of recorded interference intensity at one point on the CCD camera as a function of generated delay. The trace is obtained from the DMF1040 using a 1060 nm signal (offset coupling condition). The red line represents the envelope of the trace (averaged over 8 points). The insert shows a clear beating pattern on the output spectrum.

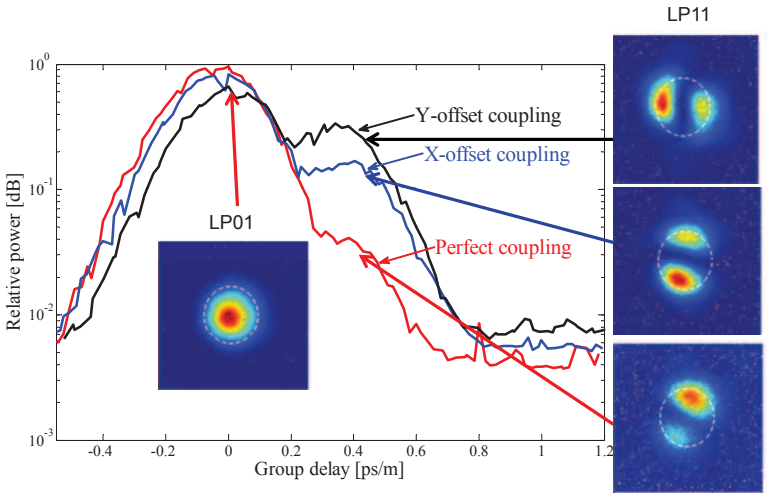

Figure 4.18: Summary of the DMF1040 modal output in the the MM regime (1060 nm) using different coupling conditions: perfect, x_{30} and y_{30}. The inserts show the reconstructed mode images.

the two peaks visible in the C^2 trace, as described in Ref.[88]. The reconstructed images are normalized: the red color corresponds to the maximum and the blue color to the minimum value of the modal intensity. The boundary of the core is illustrated by the white dashed line forming a circle. All the images presented employ the same scale and color-coding. According to the envelope of C^2 trace (averaged over 8 points of the raw trace), the LP11 mode is suppressed by about 14 dB below the FM.

As expected, when offsetting the input signal the fiber enters MM regimes of operation. Even though the two modes propagating in the fiber have a small differential group delay, C^2 imaging is still capable of resolving the modes that appear as the two peaks present in Fig. 4.17. The shown figure represents an example of measured data (raw data) at one spatial point on the image plane as a function generated delay. The MM behavior identified by C^2 imaging is also confirmed by the analysis of the output spectrum shown in the inset of Fig. 4.17: the oscillatory component in the spectrum indicates interference of the modes. While simple spectral methods have been used to analyze spectra similar to the ones shown here and quantitatively measure modal discrimination [90], unique identification of the modes involved is difficult to obtain.

Offset input coupling along x- and y-directions can lead to strong

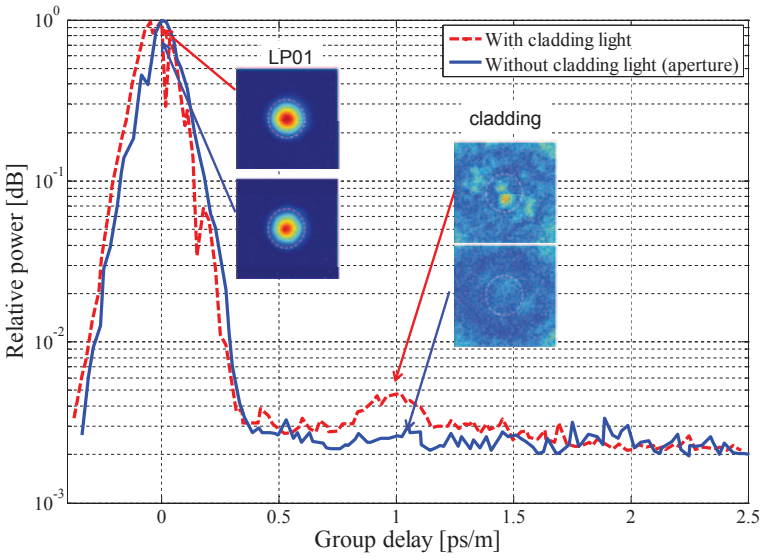

Figure 4.19: Obtained C^2 trace on the DMF1040 at 1040 nm with and without the cladding light, under the perfect coupling condition. The inserts show the reconstructed mode images.

excitation of LP11 mode such that in extreme cases this mode contributes almost 50 % of total power in the core. Figure 4.18 summarizes the characteristic behavior of the fiber for different coupling conditions. Also illustrated in the insets are the corresponding reconstructed mode images. Slight asymmetries of the reconstructed images, corresponding to the LP11 mode are due to imperfect alignment conditions of the reference and signal beams.

Next, the DMF1040 was tested in the SM regime using a source with a center wavelength $\lambda = 1040$ nm and FWHM of 10 nm, as shown in Fig. 4.11. At the optimal input-coupling condition, the corresponding C^2 trace has two peaks, one corresponding to the FM, as confirmed by the reconstruction, and another apparently corresponding to cladding modes, see Fig. 4.19. Indeed for the latter, the modal reconstruction demonstrates a feature of small relative intensity in the core region, with the size smaller than the FM on top of a noisy background. The hypothesis that the cladding modes may be responsible for the peak was tested by filtering them out with the help of an aperture located at the output of the fiber. After such filtering it was found that the peak disappears, and the modal reconstruction in the same region results in a featureless background, as Fig. 4.19 illustrates.

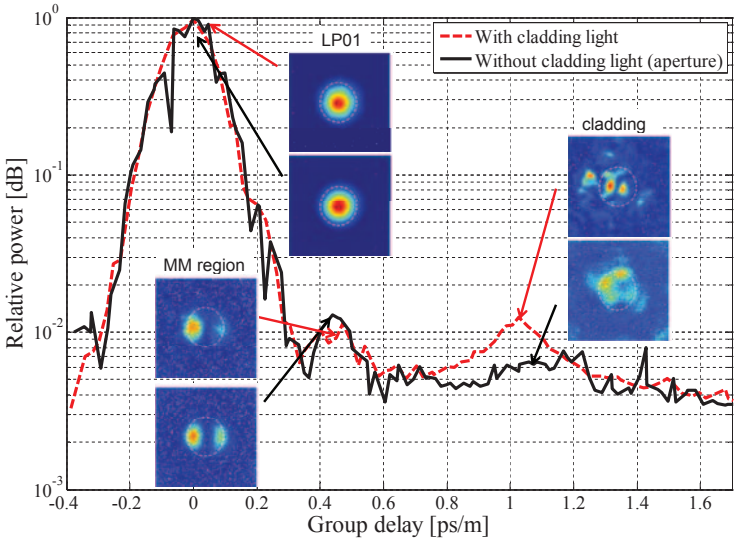

Figure 4.20: Obtained C² trace on the DMF1040 at 1040 nm with and without the cladding light under x-offset coupling condition. The inserts show the reconstructed mode images.

The resonant coupling between the core and cladding regions becomes evident when input coupling is deliberately misaligned. According to the fiber design, one expects that these excited HOMs are effectively coupled to the cladding band, and C² imaging verifies this. Specifically, Fig. 4.20 illustrates C² traces obtained at one specific horizontal offset coupling (x_{30}) position. A measurement without the aperture shows a relatively large contribution of HOMs at a differential group delay of ∼1 ps/m, which agrees relatively well with the simulations (1.2 ps/m) in Fig. 4.13. The slight difference is explained by a small mismatch between the simulated fiber design and the one used in the experiments. For example, small variations of air-hole diameters along the fiber cross-section and also along the fiber length are challenging to implement in the simulations, yet they lead to slight changes in the group delays of the modes. In addition, optical measurements of the refractive index of the core and exact dimensions of the fiber cross-section are very challenging, especially for the air-hole diameters of few micrometers or smaller. After an aperture is applied to filter out the cladding modes, the height of the peak decreases and the reconstruction shows a weak HOM. The simulations in Fig. 4.13 also predict another LP11 mode at an average group delay of ∼2.9 ps/m, but in the experiments this mode was not observed

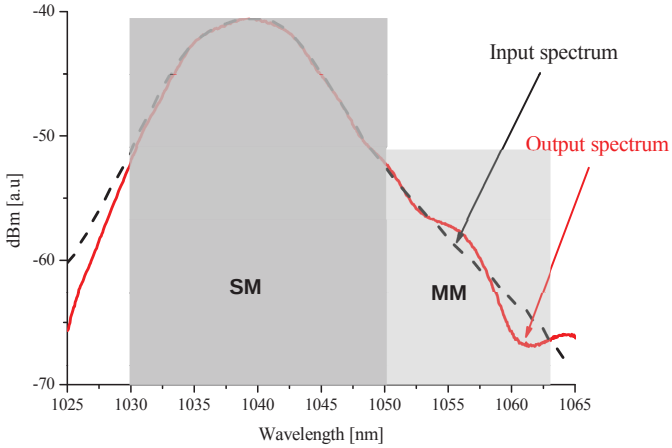

Figure 4.21: Input and output spectrum recorded for DMF1040 at 1040 nm signal. The output spectrum shows beating pattern after 1050 nm, which is outside of the SM guiding region of the DMF1040. The modal content of this mode is observed with the C^2 imaging.

even under the extreme offset coupling conditions, due to its low core overlap ratio. Interestingly, Fig. 4.20 also demonstrates an LP11 mode at a differential group delay of about ∼0.5 ps/m, as confirmed by the analysis and mode reconstruction of the corresponding peak.

The mode is suppressed 19.5 dB below the FM. Simulations of the fiber performed at 1040 nm in Fig. 4.13 seem to disagree slightly with the observations; however, this mode is present as the result of a weak spectral overlap of the seed source with the MM regime located at 1060 nm. Indeed, the spectral output measured at the output of the fiber shows oscillatory behavior resulting from modal interference at wavelengths exceeding 1050 nm, which is well within the MM guiding region, as Fig. 4.21 illustrates.

HOMs are slightly more pronounced in the fiber when offsetting input coupling in the y-direction (y_{30}). The reconstruction of the peak at ∼1.1 ps/m indicates that an LP11 mode is present and is suppressed 20 dB below the FM. Similar to the case observed with offset input coupling in the x-direction, a HOM at ∼0.45 ps/m is visible due to the signal spectral overlap with the MM region. Figure 4.22 summarizes C^2 imaging measurements performed on the DMF1040 using various offset coupling conditions.

As a summary, even under severe offset couplings (x_{30} or y_{30}) the

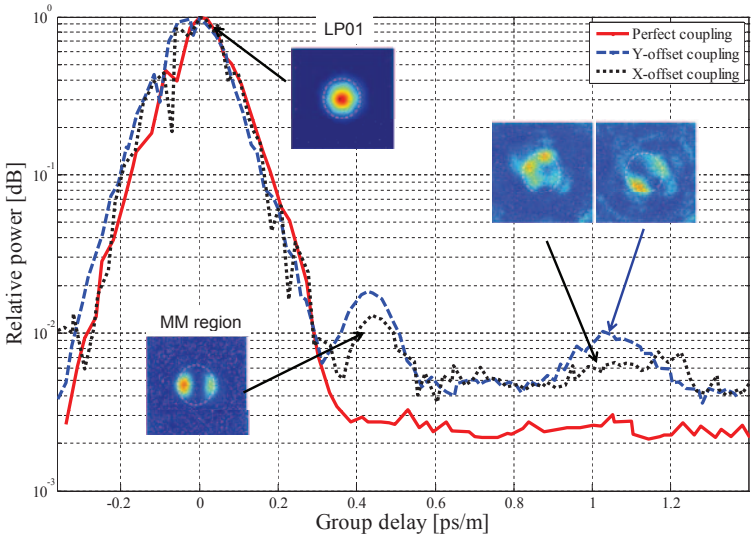

Figure 4.22: Summary of different C² imaging measurements on DMF1040 with different coupling conditions (without cladding light) at 1040 nm.

tested fiber operates in the SM regime with only a small contribution of LP11 mode, which is suppressed 20 dB below the FM.

4.2.5 Discussion on C² imaging results

Using C² imaging, resonant coupling between core and cladding modes of a rod PCF was observed. Specifically, in the SM regime offset input coupling conditions caused the resonant coupling of an excited LP11 mode to the cladding modes, as was verified by using the aperture and analyzing the corresponding C² traces. When the same fiber was used in the MM regime, this coupling was not observed. This was verified using the same method of analyzing the two C² traces obtained with and without an aperture. The two measurements with and without the aperture provided the same modal weights for the FM and HOM.

In the C² imaging measurements the background noise level limits the range of modal weight measurements. At optimal input coupling conditions the background noise level is estimated to be suppressed 28 dB below the signal peak intensity but rises up 2 dB to 26 dB below signal peak intensity for offset coupling conditions. The increase is mainly due to the presence of cladding modes, even though a simple aperture to fil-

ter them out was used. A lower background noise level can be achieved if one employs, for example, a method of spatial filtering which fully removes the low-angle cladding light. However, for the measurements the background noise level of about 26 dB still provides excellent conditions for studying SM operation of rod fiber designs.

A relatively narrow spectral source with a FWHM of about 10 nm spectral range was used to resolve the modes of the DMF rod fiber. However, the sensitivity of C^2 imaging method has led to the appearance of an LP11 mode resulting from the spectral overlap of the source with the MM regime of operation of the fiber. A narrower source centered within the SM region would lead to a lower temporal resolution due to the broadening of the cross-correlation traces and therefore would not allow one to resolve modal content. It is desirable then to employ sources with some appreciable smooth spectral width to avoid artifacts, such as the characteristic sinc-like "ringing" due to the sharp spectral edges. It would also benefit future investigations to use sources having limited spectral width with spectral edges that decay faster than a Gaussian function.

The C^2 imaging measurements were performed on a passive DMF rod fiber but the methods can be also employed for the studies of active fibers. There is a difficulty, in that the active rod fibers are heavily doped and typically the nominal core Yb absorption exceeds levels of >500 dB/m at 976 nm and ∼9 dB/m at the signal at the wavelength of 1030 nm. The absorbed light at 1030 nm is further re-emitted at the wavelengths exceeding 1030 nm. Problems then arise from the fact that the re-emitted signal is guided in the core and in the cladding which increases the background noise level. If the doping level is high enough, all signal light guided within the core would be absorbed along the fiber length, thereby rendering C^2 imaging unusable. One way to get around the problems arising from absorption is to operate the active medium in a transparent regime for the signal light by for example supplying sufficient gain to the signal by operating the fiber in a transparent regime.

For the given several plausible assumptions it is believed that C^2 imaging can be also applied to study active amplifier systems. If the gain related thermo-optical shift of the refractive index as well as the Kramers-Kronig shift do not significantly affect the phases and/or the group delays of different modes and provided the spectral changes related to the gain are properly accounted for, the resolution of the modal weights even in high-power amplifiers becomes feasible.

4.3 Summary of chapter 4

In this chapter two modal characterization methods, S^2 imaging and C^2 imaging, were described and used with two PCFs. S^2 imaging was employed on an Yb-doped SM PCF with a 40 μm core diameter and the SM properties were evaluated under offset input coupling. The HOM content was measured to be suppressed 24 dB below the FM with 3 dB variance. With C^2 imaging, the resonant coupling condition between the core modes and cladding band was evaluated in a passive SM PBG rod fiber with DMF effect under using offset input coupling (85 μm core diameter). The HOMs efficiently coupled out from the core to the cladding band and were suppressed 20 dB below the FM when the fiber was operated in the SM guiding regime.

Chapter 5

High energy fiber laser cavity

The constant demand for higher pulse energy and peak power generation from fiber lasers requires fiber designs with larger effective core area (A_{eff}) in order to mitigate non-linear effects, increase the extractable energy and increase the damage threshold level at the fiber facets. However, beam quality becomes essentially critical for single-mode (SM) operation and a very low core numerical aperture (NA) carries extremely high index precision requirements when fibers with active cores are manufactured. Very large mode area (LMA) fiber designs up to 100 μm core diameters have shown that new, more effective methods to suppress or not to guide higher order modes (HOMs) are required to provide truly SM operation of such fibers.

In this chapter a new ytterbium (Yb)-doped photonic bandgap (PBG) photonic crystal fiber (PCF) design with a very large core diameter of 85 μm and efficient HOM suppression is introduced. The fiber design was introduced early in 2011 by Alkeskjold et al. [27, 28] and in this chapter the distributed mode filtering (DMF) rod fiber is analyzed in detail. The guiding properties of the fiber are described and the fiber is used in a laser cavity configuration yielding high pulse energies. In the last section, second and third harmonic generation is tested with this rod fiber. The laser cavity and higher harmonic generation experiments were performed in collaboration with EOLITE Systems, Pessac, France, using their facilities and experimental setup.

5.1 Distributed mode filtering rod fiber

In LMA PCF rod fiber designs, efficient suppression of HOMs is challenging due to the ultra low NA requirements, but also because rod fibers are typically short (∼1 m) and kept straight, which complicates efficient HOM suppression. The basic idea behind the development of the new PBG DMF rod fiber design is more efficient HOM suppression and manufacturability with an acceptable yield. Typically, manufacturability of fibers with very large core diameters is challenging due to the extreme tolerance requirement of the ultra-low index difference between the core and cladding, and the DMF rod fiber design eases these requirements significantly. High-index elements called DMF elements form cladding bands through which HOMs are coupled to and therefore they are removed or not guided by the core. Due to the discrete nature of these elements and the method by which coupling of HOMs from the core to the cladding occur, the core of the DMF rod fiber only guides in a certain wavelength range and exhibits non-guiding, SM and multi mode (MM) behavior in different wavelength regions. A schematic and an optical micrograph of a manufactured DMF rod fiber is shown in Fig. 5.1. The DMF elements are arranged in a honeycomb-lattice, shown as cyan rings in Fig. 5.1(a) and air holes surrounded by light colored rings in Fig. 5.1(b).

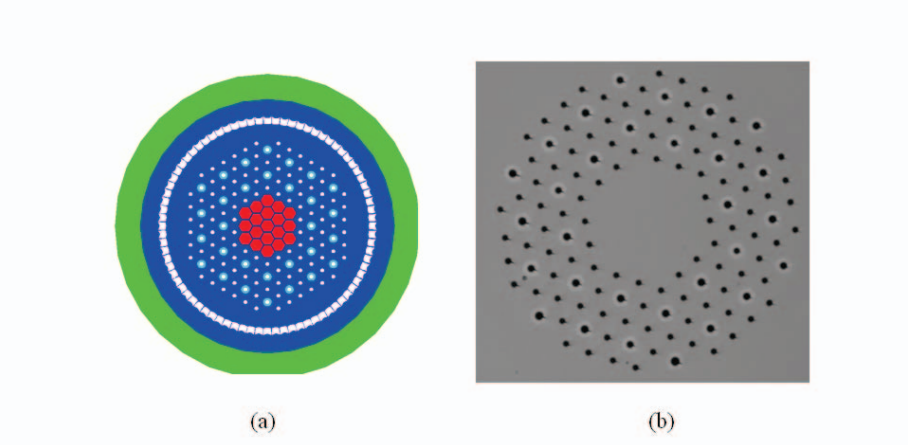

Figure 5.1: DMF rod fiber design. (a) Schematic of the rod fiber illustrating an Yb-doped core and the high-index elements (Germanium) arranged in a honeycomb lattice. (b) Optical micrograph of a manufactured fiber, only showing the central region.

5.1.1 Guiding dynamics

Figure 5.2 shows the transmission spectrum of a passive 85 μm core DMF rod fiber. A halogen-tungsten source was coupled into the core of the DMF rod fiber, the output light was coupled into a SM LMA20 fiber and the spectrum was recorded with an optical spectrum analyzer (OSA). The oscillations in the spectrum originate from modal interference of the guided modes of the rod fiber as they are coupled to the pick-up fiber. The lack of oscillations indicates that only one spatial mode is guided in the core. The non-guided regime is found in the wavelength range 980 – 1030 nm, which corresponds to the region where the fundamental mode (FM) couples out to the cladding band. The inset of Fig. 5.2 illustrates the trends of the effective mode indices of the FM and higher order core modes together with the band of the cladding modes as a function of wavelength. In the same figure near-field (NF) images are shown for different guiding regimes. At 1030 nm the FM couples out to the cladding band and therefore the rod fiber operates in a leaky regime; at 1052 nm the core supports only the FM and at 1085 nm a combination of the FM and HOMs is observed in the core of the rod fiber.

No oscillations are observed in the range 1050 – 1070 nm which indicates that the HOMs are phase matched (resonant coupling) to the cladding modes and therefore only the FM is guided in the core. Oscillations are observed at longer wavelengths (MM1 and MM2), which is a clear sign of interference between the FM mode and HOMs in the core region.

If the refractive index of the core is increased, the transmission spectrum in Fig. 5.2 will shift towards blue wavelengths. However, the DMF resonant elements in the cladding structure will shift the transmission spectrum toward red wavelengths as their refractive index is increased. In a case of an Yb-doped DMF rod fiber, thermal load, which is mainly confined to the core, can cause the refractive index to increase as the signal power is increased, and if the DMF rod fiber is operated in a leaky wavelength regime, a certain thermal load can move operation into the SM region, illustrated in Fig. 5.3. A signal at 1030 nm is initially weakly confined to the core but after DMF filtering and subsequent blue shifting the signal becomes more confined to the core and therefore shifts to the SM guiding region. This behavior is studied later in Section 6.1.3 by operating DMF rod fibers in different guiding regimes. In addition, the movement of the photonic bandgap via a thermally induced refractive index change in the core is identified under high power amplifier experiments in Section 6.3.

An Yb-doped DMF rod fiber 120 cm in length with a core diameter

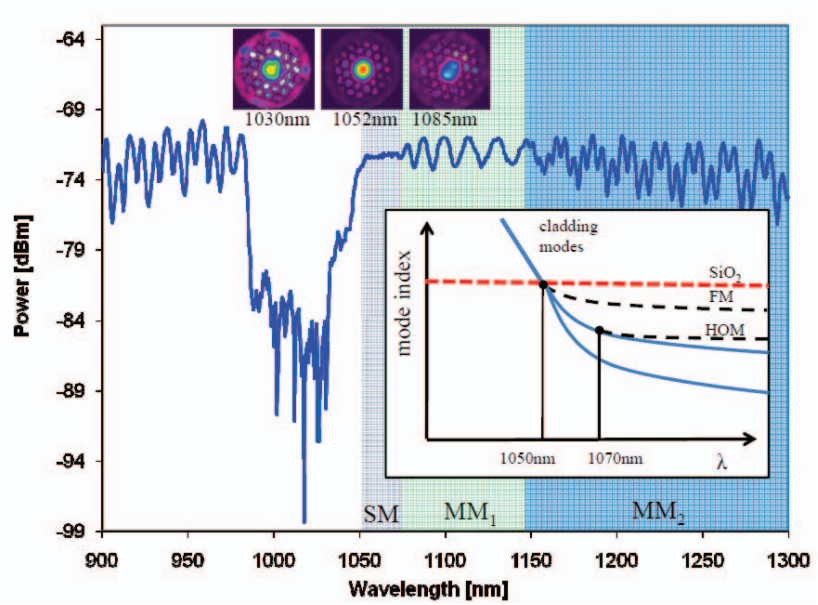

Figure 5.2: Transmission measurement of a passive DMF rod fiber with 85 μm core diameter. The measurement shows several interference patterns and indicates a SM region in the range 1050 – 1070 nm. Sketched effective mode indices of the FM and higher order core modes together with the band of cladding modes as a function of wavelength are illustrated in the same figure. NF images for different guiding regimes are also shown.

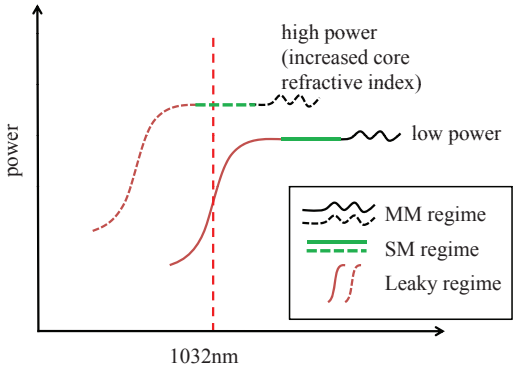

Figure 5.3: Sketched illustration of the evolution of guided regions as the refractive index of the core is increased (low and high power operation).

of 85 μm and an estimated NA ~0.01 was manufactured. The size of the pitch was 15.0 μm and the air-hole to pitch size ratio was 0.1. The fiber

had a pump cladding diameter of 267 μm with 0.6 NA and the cladding pump absorption was $\sim$ 27 dB/m at 976 nm. The active rod fiber was SM in the range 1030 – 1045 nm. Figure 5.4 shows the SM behavior of the rod fiber, when an input beam at 1032 nm was moved along the x- and y-axis. No HOMs are excited at 1032 nm when the input was misaligned.

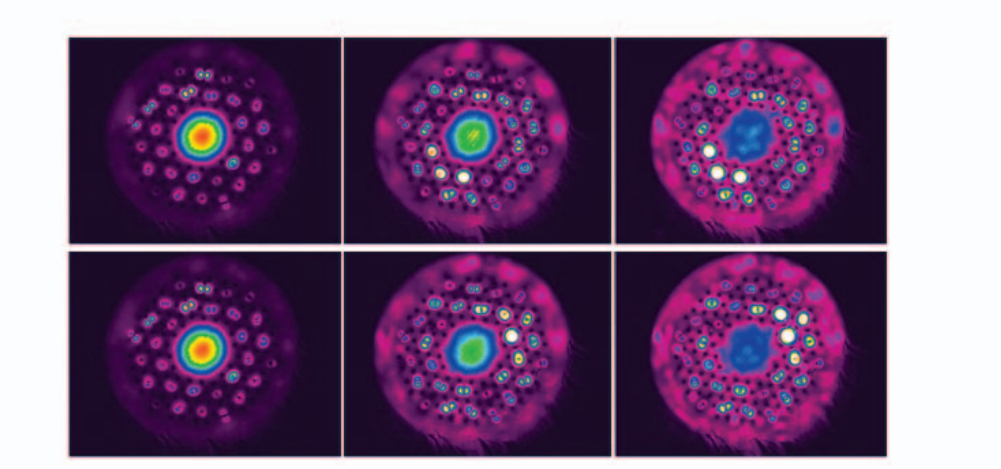

Figure 5.4: NF images of the Yb-doped DMF rod fiber at 1032 nm wavelength. The input beam is moved along the x (top row) and y (bottom row) direction and no HOMs are excited.

5.2 Experiment setup

A fiber laser cavity setup was used to test the performance of the DMF rod fibers in the continuous wave (CW) and Q-switched, high pulse energy regimes. The experimental setup, illustrated in Fig. 5.5, consists of a CW 976 nm pump diode with a 400 μm core diameter delivering 200 W of optical power, followed by a PCF DMF rod fiber, having polished end facets at angles of 5° (HR) and 0° (OC) (without end caps). An acoustic-optical-modulator (AOM) was employed when operating in a Q-switched regime. The laser cavity was formed by using either a highly reflective (HR) mirror with spectrally flat response or a volume Bragg grating (VBG) operating at 1030 nm and the 4 % end facet reflection at the output end. The length of the rod was 75 cm and the pump light was double passed through the rod fiber. In these experiments a commercial M^2 measurement device (DataRay Inc, WinCamD

+ M2DU M2) with a standard 4 Sigma M^2 calculation routine was used to determinate output beam quality.

A pinhole positioned after the end facet of the rod fiber was used

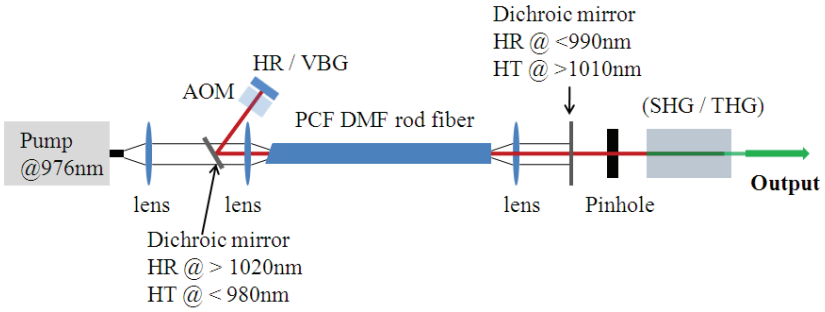

Figure 5.5: Schematic of the high power fiber laser cavity setup.

in order to quantify the ratio between core and cladding light and to investigate the guiding dynamics of the core. In all measurements, the pinhole was used to suppress cladding light and all the reported power values represent only the core signal power.

5.2.1 Continuous wave laser cavity measurements

No HOMs were observed when the rod fiber was operated in a CW laser cavity configuration using a flat HR mirror and the end facet as a cavity feedback. The output beam was stable with close to diffraction limited beam quality, having M^2 values less than 1.4. In this configuration the lasing wavelength is not locked and lasing was observed to occur within a wide wavelength range between 1024 – 1047 nm. A portion of the observed lasing is spectrally outside of the previously measured SM regime of the DMF fiber, leading to degradation of the M^2 number. Spatial or spectral filtering is required to fully obtain a diffraction-limited beam with M^2 approaching 1. Figure 5.6 shows an optical slope efficiency measurement including NF and far-field (FF) images recorded at 110 W output power. The slope efficiency was measured to be 62 % and was calculated using the measured core signal power versus the available pump power. The light intensity in the cladding region was manageable, increasing from 5 % to 18 % while the pump power was increased from 23 W up to 210 W.

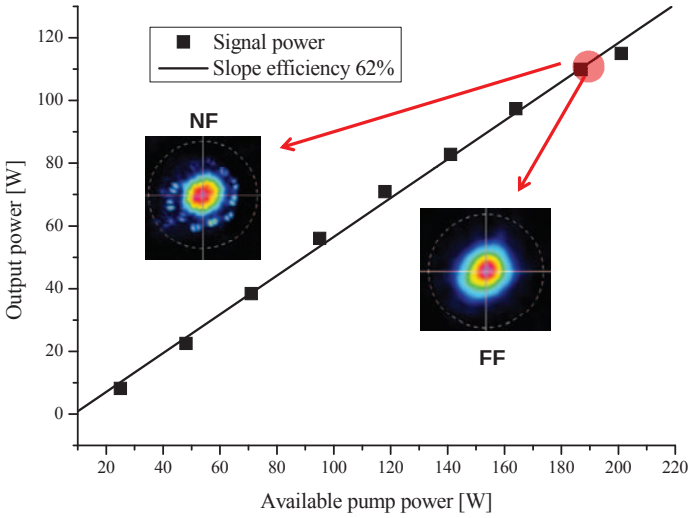

Figure 5.6: Slope efficiency measurement of the DMF rod fiber, in a laser cavity (CW) configuration formed with a flat HR mirror. Insets show NF and FF images at 110 W output power level.

5.3 High pulse energy generation

An AOM was inserted into the cavity and a flat HR mirror and the feedback from the end facet was used to form the cavity. Again, very stable and near diffraction limited beam quality was achieved up to 104 W of average output power with 100 kHz repetition rate, corresponding to pulse energies of ∼1 mJ. With low repetition rates (10 – 30 kHz) pulse energies up to 2.7 mJ were obtained, resulting a peak power of ∼200 kW. To avoid damages at the fiber facets the maximum pulse energy was limited to 2.7 mJ. The damage threshold level of the facets was experimentally observed to occur at pulse energies of ∼ 3.0 mJ. The slope efficiency was measured to be 57 % at 100 kHz repetition rate, shown in Fig. 5.7 and the temporal pulse width was measured to be 21 ns at the highest output power level. The beam quality was fairly consistent at all power levels and NF and FF images at 80 W output power are shown in Fig. 5.7. The M^2 values were typically around 1.2 except at high output power levels, over 75 W, where the light guided by the DMF elements caused an increase of the measured M^2 values. This is caused by the high amount of cladding light due to parasitic lasing outside of the SM regime of the DMF rod fiber. If a spatial filter is used at the output, a smaller M^2 number can be achieved.

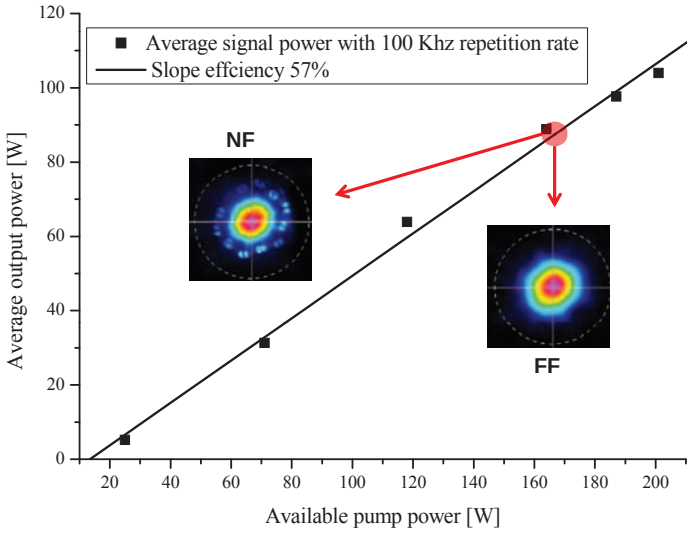

Figure 5.7: Slope efficiency measurement of the DMF rod fiber, in a Q-switched laser cavity configuration formed with a flat HR mirror. Insets show NF and FF images at 80 W of average output power level. The slope efficiency measurement was performed at 100 kHz repetition rate and the temporal pulse width was measured to be 21 ns at the highest power level.

5.3.1 Wavelength locking

The flat HR mirror was replaced with a VBG exhibiting a high reflectivity at 1030 nm (0.4nm spectral range). Again, the DMF rod fiber was tested with various repetition rates up to 200 kHz and up to pulse energies of 2.0 mJ (at 10 kHz), which was set as a limit in order to avoid damage to the end facets. No beam quality degradation was observed at the various repetition rates used up to 47 W of average output power. M^2 values were always measured to be <1.1. However, an abnormal behavior was observed at high output power levels. Above 47 W, the output power started to decrease when the pump power was increased. The same behavior was observed with the CW configuration as well but at a slightly higher output power level of 69 W. The threshold level of this behavior seemed to depend on the applied laser cavity configuration and shows that the spatial phase distortion introduced by the thermal load in the VBG cannot be perfectly filtered out by the short piece of rod fiber used in the cavity.

The measured slope efficiency was 51 %, shown in the inset of Fig. 5.8. The same figure shows the recorded NF and FF images at 33 W average output power level. Improvement on the recorded NF

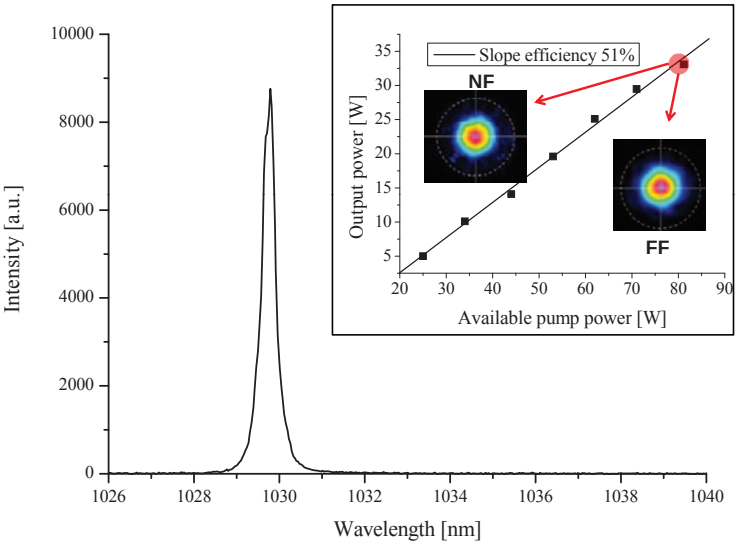

Figure 5.8: Recorded output spectrum of the laser cavity at 33 W of output power at 20 kHz repetition rate and temporal pulse width of 14 ns; spectral FWHM ∼0.4 nm. The inset shows a slope efficiency measurement together with NF and FF images at 33 W of average output power. The slope efficiency measurement was performed at 20 kHz repetition rate and temporal pulse width of 14 ns at the highest power level.

images compared to the earlier experiments was observed due to the wavelength locking of the VBG. The lasing occurs at the wavelength which is fully within the SM region of the DMF rod fiber. The spectral width was measured to be ∼0.4 nm at 33 W average output power at 20 kHz repetition rate and 14 ns temporal pulse width.

The Q-switched laser cavity configuration provides high peak and average power with a good spatial and spectral brightness and therefore efficient high power harmonic generation can be performed. The relation between spectral brightness of a source $B_{spectral}$ and spatial brightness $B_{spatial}$ is described by the following formula:

$$B_{spectral} = \frac{B_{spatial}}{\Delta\lambda} = \frac{\frac{P}{\Omega A}}{\Delta\lambda} \approx \frac{4P}{\pi MFD^2 NA^2 \Delta\lambda} \tag{5.1}$$

where $\Delta\lambda$ is the linewidth, P is the output power, MFD is the mode-field diameter of the output beam, Ω is the far-field solid divergence angle of the output beam and NA is the numerical aperture of the core. The spectral brightness of the fiber laser was calculated to be 125 $W/\ \mu m^2\ /\ nm$.

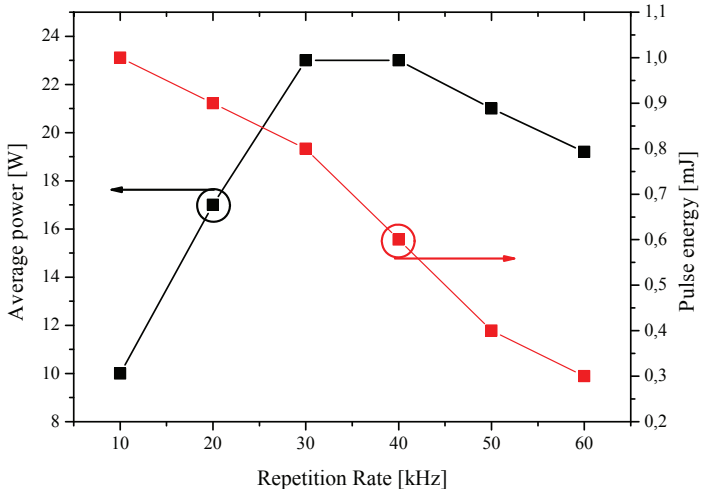

Figure 5.9: Maximum obtained average power and pulse energy of the SM DMF rod fiber after SHG at 515 nm as a function of pulse repetition rate.

5.3.2 Harmonic generation

Non-linear Lithium Triborate (LBO) crystals were inserted after the rod fiber in order to evaluate the laser cavity output via second-harmonic generation (SHG) and third-harmonic generation (THG). For SHG a 20-mm long LBO crystal with non critical phase matching was used. Two critically phase matched 15 - mm long LBO crystals in a row were used for THG [91, 92]. The crystals were antireflection coated and placed inside a temperature controlled oven. The output beam from the laser cavity was focused down with a ∼200 μm beam diameter at the beam waist within the crystal.

Second harmonic generation experiments

Stable SHG signal up to 23 W of average output power at 30 kHz repetition rate was achieved. A single-stage Q-switched rod fiber laser delivering record high pulse energy of 1 mJ at 515 nm at 10 kHz repetition rate and 13 ns temporal pulse width was demonstrated. The maximum obtained average power and pulse energy after SHG is shown in Fig. 5.9.

The system was operated at the highest possible power level for ∼10 min and no power or beam quality degradation was observed. The conversion efficiency from IR to green light was 48 %, as shown in Fig. 5.10(a). The beam quality was near diffraction limited with

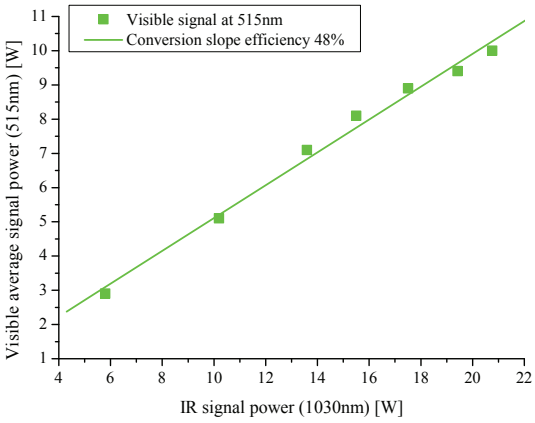

(a)

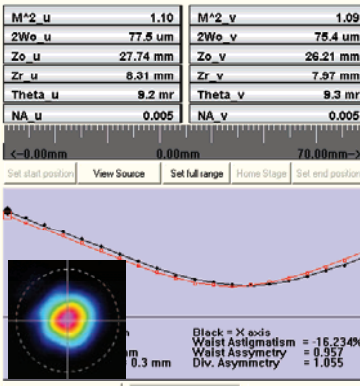

(b)

Figure 5.10: (a) Slope efficiency of the harmonic generation from IR to green light. (b) Typical M^2 measurement results after SHG, with 0.7 mJ pulse energy, 10 kHz repetition rate and 14 ns temporal pulse width.

M^2 <1.1, shown in Fig. 5.10(b). The beam quality measurement was recorded at 0.7 mJ pulse energy at 10 kHz repetition rate and 14 ns temporal pulse width.

Third harmonic generation experiments

High pulse energy of generated UV light at 343 nm from a fiber source was measured in THG experiments. A stable output beam with near

diffraction limited beam quality up to 500 μJ, 400 μJ and 300 μJ was achieved at 10 kHz, 20 kHz and 30 kHz repetition rates, respectively, as shown in Fig. 5.11. The temporal width of the pulse at the maximum output power, increased from 11 ns to 16 ns when the repetition rate was increased from 10 kHz to 30 kHz.

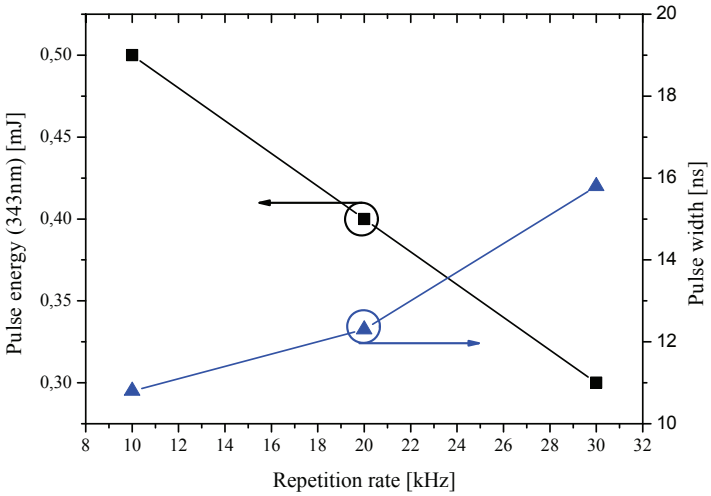

Figure 5.11: Third harmonic generation at 343 nm with different repetition rates.

5.4 Summary of chapter 5

This chapter introduced the new PCF rod fiber design possessing effective HOM suppression called a DMF rod fiber. This rod fiber design is a PBG fiber design and in some certain wavelength ranges the modes in the core couple to the cladding band e.g. SM operation is maintained, formed by high index resonator elements in the cladding. An Yb-doped rod fiber was used in a laser cavity and operated in CW and Q-switched configurations. SM operation of the rod fiber enabled simultaneously good beam quality with high average power and pulse energy generation using a simple laser configuration. In the last section, the output of the laser was used to generate harmonic frequencies resulting in record high pulse energies at visible (515 nm) and UV (343 nm) wavelengths up to 1 mJ and 500 μJ, respectively, from a single stage Q-switched fiber laser.

Chapter 6

High power rod fiber amplifier

Recently, experimental and theoretical studies have shown beam quality degradation of large mode area (LMA) fiber lasers and amplifiers when operating at high average power levels [69, 93–98]. This manifests as severe mode instabilities (MIs), occurring at some threshold level which seems mostly depend on the effective area and inversion profile [94, 95, 97]. The cause of MIs are still under discussion and the earlier described large pitch fiber (LPF) fiber design in Section 2.4.1 has pushed output power levels out of LMA fiber higher before the onset of MIs are observed [43, 44].

In this chapter a high power fiber amplifier configuration is used to study the properties of distributed mode filtering (DMF) rod fibers under high power operation. First, a high power seed source at 1032 nm is constructed and characterized together with a high power pump module delivering up to 600 W of output power at 976 nm. Then, the DMF rod fibers are tested under active operation. The mode quality and power conversion efficiencies are reported and a study of the thermally induced refractive index change in the core by identifying a distinct movement of the edge of an photonic bandgap is included. In addition, MIs in high power fibers are discussed and the limits of DMF rod fibers are tested. An improved performance, a memory effect and increase of the MI threshold level is shown by operating the rod fiber in a special guiding regime.

6.1 High power rod fiber amplifier experiments

The high power rod fiber amplifier configuration consists of a high power seed source and a rod setup. The seed source for the rod setup consists of a master oscillator power amplifier (MOPA) comprised of a mode-locked seed source and a several-stage fiber amplifier chain, the final of which is built using free-space optics. The rod housing was purchased from an external supplier and it consisted of the necessary mechanical and optical components to operate rod type fibers in an amplifier configuration and fit the requirements of this thesis work.

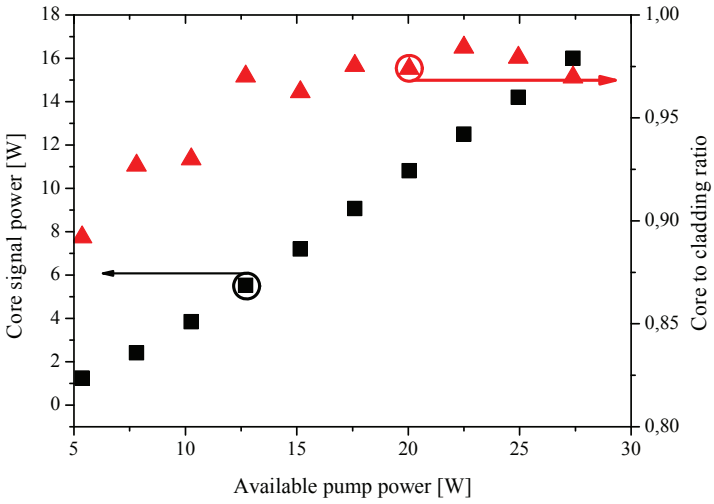

Figure 6.1: Output power of the ps-seed source and the measured signal core-to-cladding ratio.

6.1.1 High power seed source and pump module

The rod seed source deliveres a linearly polarized signal with ∼30 ps pulses at 1032.2 nm at a 40 MHz repetition rate. The seed source generates a signal via a mode-locked ps seed laser, and the signal is passed through several all-fiber amplification stages which maintain the spectral and temporal pulse characteristics. The last fiber amplifier before the rod, the photonic crystal fiber (PCF) amplifier, is constructed using a 3-m long ytterbium (Yb)-doped single-mode (SM) PCF. The fiber has a core diameter of 40 μm and is backward pumped through a 200 μm cladding with a multi mode (MM) pump at 976 nm. This fiber is the

same as in the earlier modal characterization experiments in Section 4.1 and therefore provides a SM, linearly polarized output beam. The signal is amplified from ∼1 W up to 17 W in this stage and the pulse shape is maintained without any indication of non-linearities or amplified spontaneous emission (ASE).

The efficiency of the PCF amplifier is only moderate (max ∼51 % optical to optical), shown in Fig. 6.1, due to the fact that the pump module is operated away from the optimal temperature. This of course detunes pump laser the emission wavelength and the main absorption peak of Yb ions is not utilized, reducing overal pump absorption of the fiber. The pump module is cooled with the same water line as the main base plate of the rod setup, which requires cooling water of ∼20 °C. The signal core-to-cladding ratio out of this amplification stage is as high as 98 %, shown in Fig. 6.1.

The PCF amplifier has a 10 dB spectral width of ∼0.5 nm and ∼0.7 nm at 1.2 W and 16 W of average output power level, respectively, as shown in Fig. 6.2. The maximum seed power is limited by the available pump power. The output of the PCF amplifier is coupled to the rod fiber through a high power free-space isolator via free-space optics. Therefore, the seed source exhibits a high polarization extinction ratio (PER) of ∼24 dB.

The rod fibers are pumped in counter-propagating direction with a

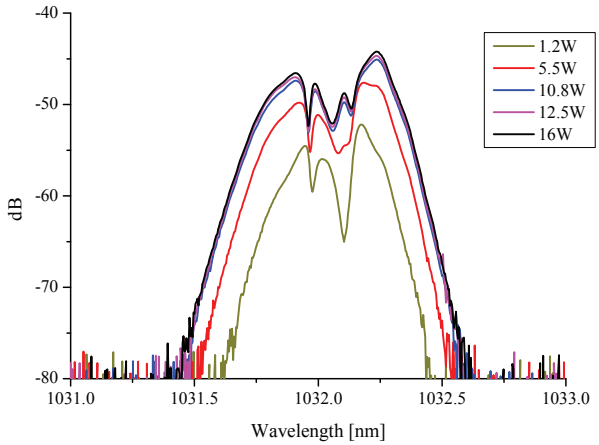

Figure 6.2: Measured spectra of the ps-seed source at different average output power levels.

pump module delivering up to 600 W of pump power (976 nm, 400 μm,

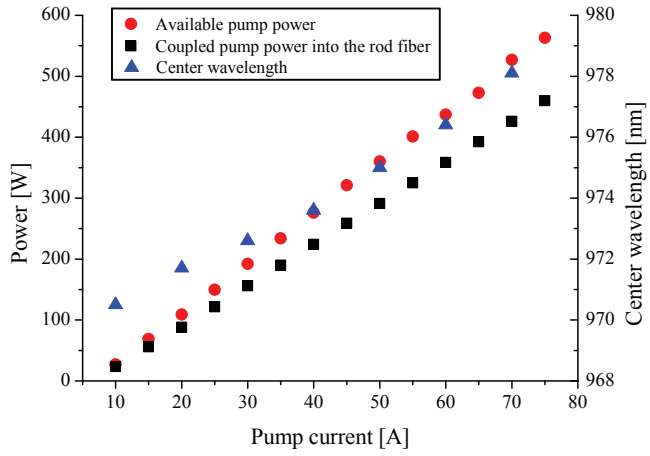

(a)

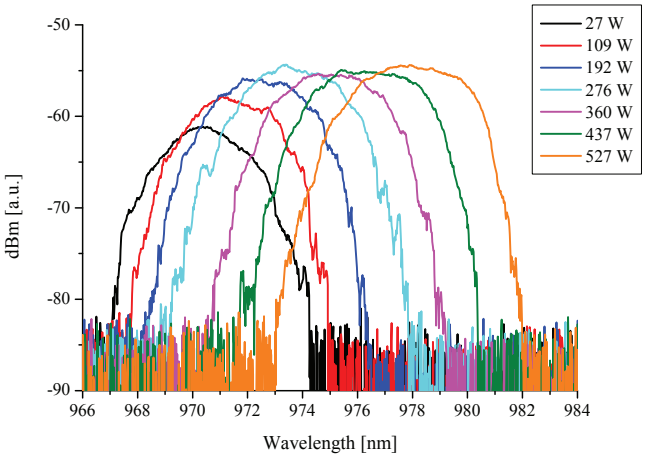

(b)

Figure 6.3: (a) Measured output power of the pump module, the coupled power into the rod fiber and center wavelength of the pump module. (b) Measured spectra of the pump module at different output power levels.

0.22 NA) shown in Fig. 6.3(a). The same figure shows the measured coupled power into the rod fibers. The coupling efficiency was measured using a passive double clad rod fiber with the same cladding diameter as the active rod fibers used in the experiments. The coupling efficiency is rather low, reaching only a maximum of ∼83 % , shown in Fig. 6.3(a)

which is caused by losses through the optics and imperfect pump fiber imaging.

The pump module is not wavelength stabilized and therefore the center wavelength of the pump shifts when the pump power is increased, shown in Fig. 6.3(b). The pump module is water cooled and the temperature of the water is optimized to ∼30°C to obtained maximum pump absorption at the pump power level of ∼360 – 430 W as the most of the experiments only require a maximum pump power of less than the designed output power of 600 W. The pump module has a spectral width of ∼3 – 5 nm and the center wavelength moves from ∼970 nm to 978 nm, as shown in Fig. 6.3, when the pump power is increased from 27 W to 527 W, respectively.

6.1.2 High power rod setup

Figure 6.4 shows the schematic of the entire high power rod amplifier setup. Both the pump and the signal are single-passed through the rod fiber. The output of the rod fiber is sampled for beam diagnostics and a CCD camera (Spiricon GRAS20, frame rate ∼20 Hz) is used to verify the beam quality. Two different Yb-doped double-clad DMF rod fiber designs were used for experimentation which were manufactured to be SM in two different wavelength regions, one at 1030 – 1045 nm, hereafter referred to as DMF1030, and the other at 1050 – 1070 nm, referred to as DMF1064. The DMF rod fibers have a core diameter of ∼85 μm, an

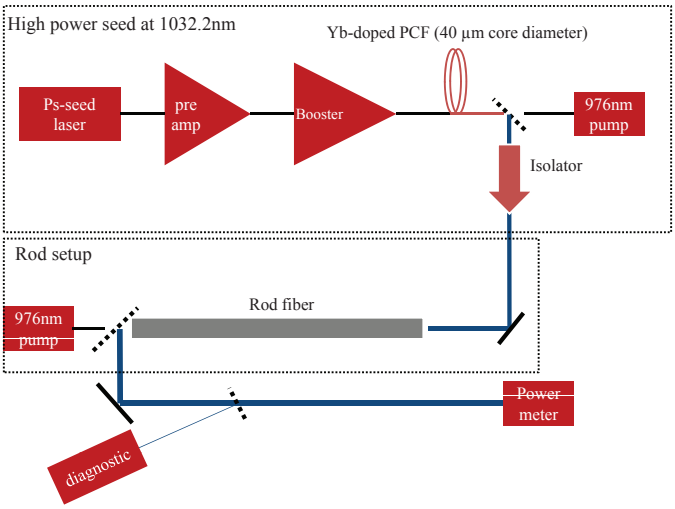

Figure 6.4: Schematic of the high power rod amplifier setup.

estimated core numerical aperture (NA) of ∼0.01 and a pump cladding of

265 – 270 μm with ∼0.6 NA. The length of the DMF rod fibers is 90 cm and the pump absorption is ∼27 dB/m (nominal) at 976 nm. Both of the ends are prepared with AR-coated end caps. When high power experiments are performed the rod fibers are placed inside a V-groove in an aluminum holder and covered with a thin sheet of copper. The aluminum holder is water cooled through a base plate and a copper sheet on top of the rod fiber provides a small amount of heat dissipation along the rod length as well as a method by which the rod is mechanically secured.

6.1.3 Power conversion efficiency and mode quality

In the first test a seed power of 1.1 W was amplified and the slope efficiency up to the onset level of mode instability (MI) for the two DMF rod fibers shown in Fig. 6.5 was measured. Both of the rod fibers have >70 % slope efficiency but the threshold level of MI is different. At

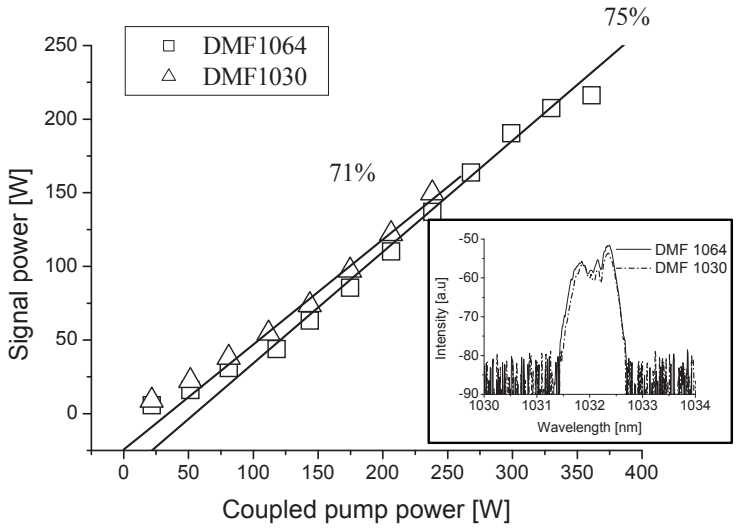

Figure 6.5: Slope efficiency measurement of the DMF1030 and the DMF1064 and recorded output spectra at the maximum output powers.

∼150 W of output power the DMF1030 start to suffer from MI but for the DMF1064 the MI threshold level is not observed until output reaches 216 W. The method described by Eidam et al. [94] was used to identify the MI threshold level, which is described as the power level where the output beam quality shows a first sign of a temporal change from single mode to a random temporal movement. This method requires a

fast detection device to fully resolve the first temporal changes of the beam quality. The CCD camera used in the experiment had a frame rate of ∼18 Hz but still provides a repeatable way to compare different rod fiber samples within ±10 W repeatability. Spectral broadening of the amplified signal is small and the measured output spectra have a 10 dB spectral width of ∼0.9 nm (FWHM ∼0.3 nm), shown in the inset of Fig. 6.5.

When the DMF1064 is seeded with a 1032 nm signal it operates in a leaky waveguide regime, where the fundamental mode (FM) is partly coupled to the DMF elements and has high confinement loss. At low output power levels (<50 W), the core mode appears to be leaky with high amount of cladding light, but becomes more confined at higher output power levels (>80 W), as shown in Fig. 6.6(a). This can also be observed from the signal core-to-cladding ratio measurement, shown in Fig. 6.6(a), which shows that the core light increases from 60 % to 93 % with increasing power. The increased confinement loss at low power levels also decreases the measured slope efficiency at low power levels, as shown in Fig. 6.5. This indicates that the confinement loss decreases with increasing output power levels, which is caused by a thermally induced change in the refractive index profile. As the DMF1064 is operated in the leaky regime at low power levels and as the power is increased, the thermal load will raise the refractive index of the core and the DMF filtering effect is blue shifted. The guiding dynamics of the DMF rod fibers under high power operation and a thermally induced refractive index change will be discussed more in Section 6.3.

The DMF1030 is operated in the SM guiding regime at all the power levels and therefore the confinement loss is low. The measured signal core-to-cladding ratio, except at very low power (<10 W), is within the range of 90 – 97 % and the mode appears to be well confined in the core, shown in Fig. 6.6(b).

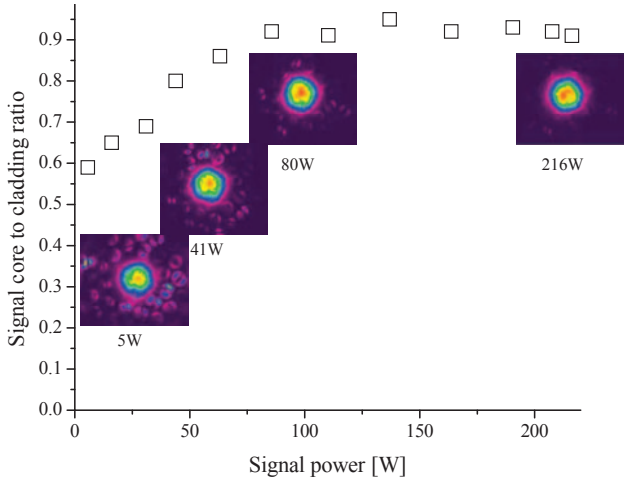

(a)

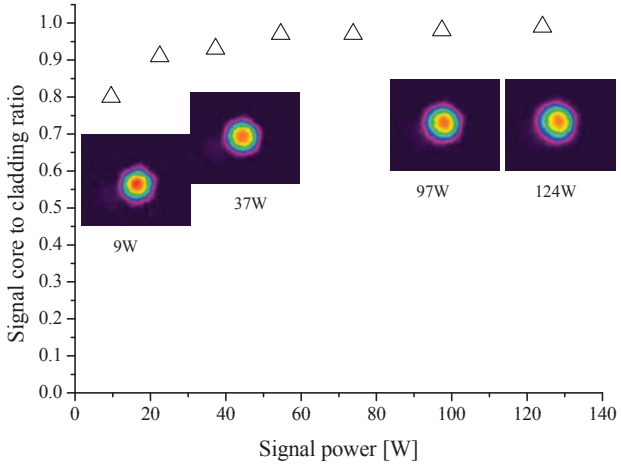

(b)

Figure 6.6: Measured signal core-to-cladding ratio and recorded evolution of the NF image quality at different signal (1032nm) output powers for two DMF rod fiber (a) DMF1064 and (b) DMF1030.

6.2 Modal instabilities in high power operation

An example of MIs is shown in Fig. 6.7, where below the MI level the beam quality appears SM but above the threshold level beam quality becomes unstable and several modes are seen. One possible cause of MIs is the formation of inversion and/or thermal long-period grating (LPG) formed by

the interference between the FM and higher order modes (HOMs), which can be supported by a SM waveguide under strong thermal load [95, 97]. Gain and therefore inversion plays a vital role on the formation of this LPG and thereby gain dynamics will change the onset level of MIs [94].

A 101 cm long, new DMF1064 rod fiber was tested with a much high

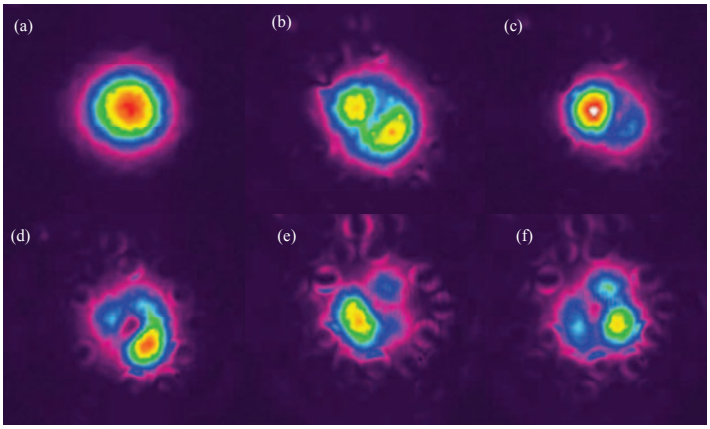

Figure 6.7: Mode field images of output from the DMF1030 rod below and above the MIs threshold level. (a) below (<150 W) an (b)-(f) above the threshold level (>155 W).

seed level of 15 W. With these conditions, an average output power level of 292 W was reached before the onset of MIs was observed. The measured slope efficiency is high at 73 % and the mode quality is good below the MI level, shown in Fig. 6.8. As observed earlier, the confinement loss is high at low output power levels and thereby the slope efficiency below 100 W of output power level is low at 39 %. This can also be partially attributed to the pump spectrum missmatch. The inset of Fig. 6.8 shows the measured output spectrum at the highest power level. The amplified signal experiences a small amount of spectral broadening with a 10 dB spectral width of ∼1.1 nm at maximum output power (full width half maximum (FWHM) ∼0.3 nm).

6.2.1 Memory effect

As the experiment was repeated multiple times, a decrease in the MI threshold level was observed. This indicates that the fiber possesses a memory effect, possibly because the LPG grating has a component which is of a permanent nature. A permanent inscription of index changes by high-power radiation could be related to the color-center formation commonly associated with photodarkening phenomena. A set of measure-

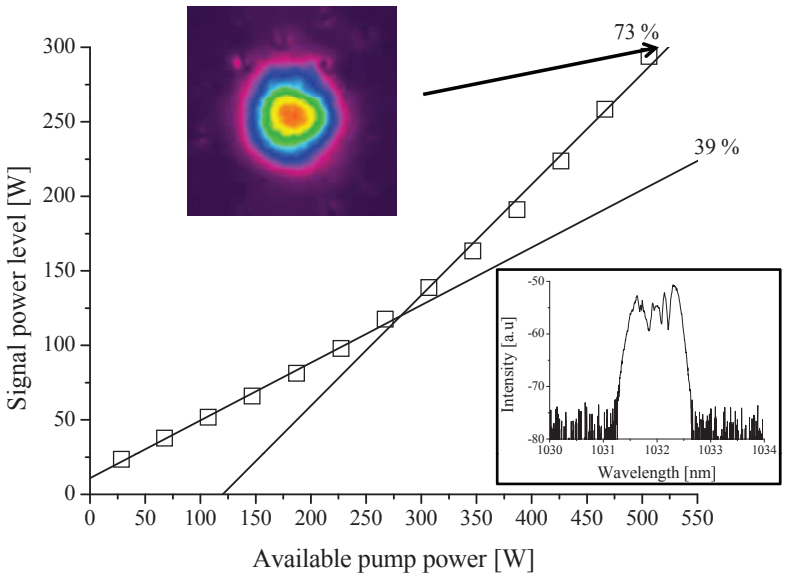

Figure 6.8: Slope efficiency measurement of the DMF1064 with 15 W of seed power level, recorded mode field images and spectrum at the maximum output power level.

ments on the DMF1064 rod fiber was performed where the MI threshold level was obtained ten times while allowing the system to cool down ∼1 min between each test. The level of the MI threshold lowered from ∼292 W down to ∼230 W after a few tests and stabilized around 230 W.

If the formation of the LPG is linked to color center formation, it can be, with some limitations, removed by bleaching either thermally or optically [99]. Therefore, the rod fiber was exposed to blue irradiation (405 nm, ∼20 mW) from a laser source. Light from the laser source was coupled into the pump cladding of the rod fiber through the end-facet and exposed for 20 hours. After the photo-bleaching, the earlier test was repeated. The MI threshold level recovered and was back to the originally observed level of ∼285 W but once again the level decreased when the experiment was repeated, as shown in Figure 6.9. Error bars in the figure shows the uncertainty of those measurements caused by the slow detection system used (±10 W). It seems that photo-bleaching can remove the formed LPG grating (or at least part of it) but the photo-bleaching is reversible process and it will not prevent future formation of the LPG grating [99].

Self-recovery of the MI threshold level was tested by storing the

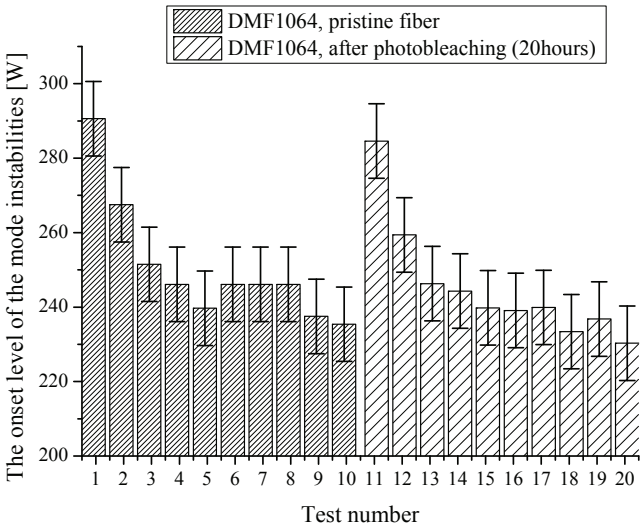

Figure 6.9: Development of the MI threshold level of a pristine rod fiber and after photo-bleaching it with blue laser source (405 nm, 20 mW, 20 hours). Error bars ±10 W represent the uncertainty caused by the slow detection system.

rod fibers in closed plastic bags and testing those rod fibers to find the MI threshold level after a certain time. No recovery of the MI threshold level was found for the samples stored for few days to a few weeks. The MI threshold level was always measured to be the same before and after storing the rod within the uncertainty limit of the detection system. The only working method discovered in this work to recover rods to their initial state and increase the MI threshold level was found to be through photo-bleaching. Depending on the glass composition, other means for photo-bleaching can also be implemented, such as bleaching simultaneously under active operation, photo-bleaching at different wavelengths or incorporating thermal bleaching.

6.3 Photonic bandgap movement under high power operation

The movement of the photonic bandgap edge using a DFM1064 rod fiber (101 cm long) was measured by seeding the rod fiber with an ASE source with 1.1 W of input signal and varying the pump power. Figure 6.10 shows the input ASE signal spectrum and typically measured

output spectrum of two rod fibers with similar parameters (core diameter, pump absorption, doping level), one without (reference rod fiber) and one with the DMF elements. The spectrum obtained from the rod fiber with DMF elements (DMF1064) shows clear edge of the photonic bandgap in the leaky wavelength regime at ∼1040 nm, while the output spectrum from the rod fiber without the DMF elements is smooth without any indication of photonic bandgaps.

The output spectrum was measured at different signal power levels

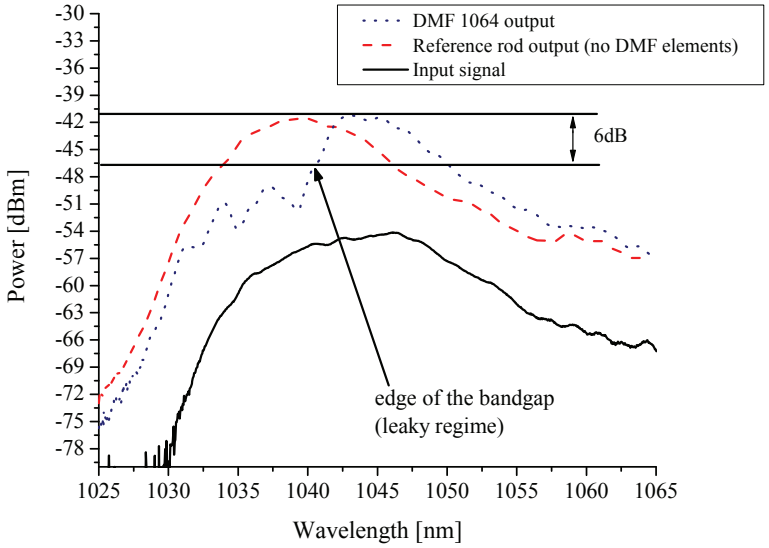

Figure 6.10: Measured spectrum of the input ASE signal and output spectra of two different rod fibers, one without DMF elements and one with DMF elements (DMF1064) under the same pumping conditions. The DMF1064 shows clearly resolved edge of the photonic bandgap in the leaky wavelength regime at ∼1040 nm.

up to ∼160 W and a 6 dB power criteria was used to identify the edge of the photonic bandgap, as shown in Fig. 6.10. The measured output spectra were subtracted from the input spectrum and gain induced photonic bandgap blueshift was corrected using a reference gain profile for each power level. The reference gain profiles were obtained from a reference rod fiber without the DMF elements. Without the gain correction, the measured photonic bandgap position would be more blue shifted as increasing Yb gain peaks at 1030 nm.

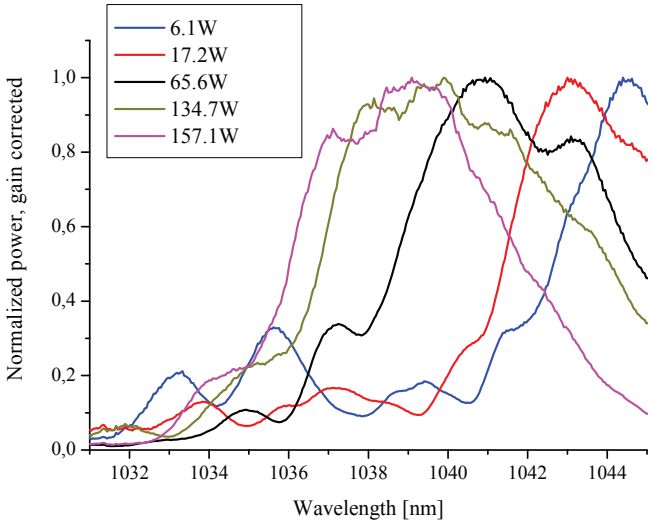

Figure 6.11: Normalized output spectra of the DMF1064 at different output power levels.

6.3.1 Thermally induced refractive index change

The movement of the photonic bandgap is a clear evidence of a thermally induced refractive index profile change of the rod fiber. The thermal load is highest at the output end of the rod fiber and declines toward the input end, and therefore the photonic bandgap blueshift is gradual along the fiber length. The measurement thereby shows an effective photonic bandgap position and not the absolute or local photonic bandgap position as the edges of the photonic bandgap are broadened. Figure 6.11 shows normalized output spectra of the DMF1064 at five different output power levels. The edge of the photonic bandgap moves from ∼1043 nm to ∼1035 nm when the signal power increases from 0.5 W to 157.1 W (6 dB power criteria). This measurement shows that the guiding dynamics of the DMF1064 change from leaky at low power operation to almost SM guiding at high power operation if a signal centered at a wavelength of 1032 nm is considered. However, the observations in Section 6.1.3 (signal core-to-cladding measurement) indicated that already above 80 W of output power the DMF1064 guides in the SM regime as is evidenced by an increasing core-to-cladding ratio. This is caused by the gain dynamics of a backward pumped system; the highest amount of gain is imparted to the signal at the output end of the rod, and therefore the signal core-to-cladding ratio is affected more by the local photonic

bandgap position at the end of the rod fiber.

To obtain an estimate of the thermally induced refractive index change, a circular symmetric step-index fiber approximation of the DMF rod fiber was simulated using a beam propagation model, taking transverse hole-burning and the thermo-optical effect into consideration [69]. A core NA of 0.016 and core diameter of 60 μm was chosen to match the mode field diameter (MFD) of the actual DMF fiber FM, and the Yb concentration in the core was chosen to provide 27 dB/m pump absorption at 976 nm. The simulated rod fiber length was 1 m and the seed level was constant at 1 W. The pump power was altered in nine steps from 10 W to 200 W yielding signal levels from 6 W to 153 W. The boundary condition for the calculation of the thermal profile was chosen to be a Dirichlet boundary condition, in which the temperature at the fiber surface was fixed at room temperature.

Three examples of simulated thermally induced index change pro-

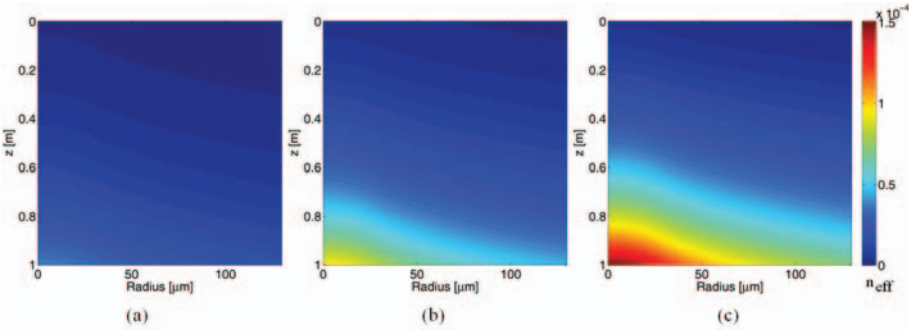

Figure 6.12: The simulated thermally induced refractive index profile of a circular symmetric fiber with similar properties as the DMF rod fiber used in the experiments with signal power level of (a) 38 W, (b) 97 W and (c) 153 W.

files are plotted on the same color scale for the change in refractive index Δn from 0 to $\sim 1.5 \cdot 10^{-4}$ in Fig. 6.12 with signal output power levels of (a) 38 W, (b) 97 W and (c) 153 W. The largest change in refractive index occurs at the center of the core and diminishes as a function of radius. The change of the refractive index Δn at the end of the rod fiber is determined as the difference in the refractive index at r = 0 and r = 54 μm for z = 1 m. The outer radius of r = 54 μm was chosen because the first ring of resonators (DMF elements) are located at a mean radius of 54 μm, which means that change of the refractive index is an approximation of the refractive index difference between the first ring of resonators and the center of the core. The change in the refractive index is only applied to the hexagonal core, shown in Fig. 6.13(a) as a

step-index profile. The photonic bandgap in the DMF rod fiber occurs because of the DMF elements, which implies that temperature difference between these elements and the core becomes the dominating reason for photonic bandgap movement caused by a thermally induced refractive index change.

Cross-sections of the DMF rod fiber were modeled numerically us-

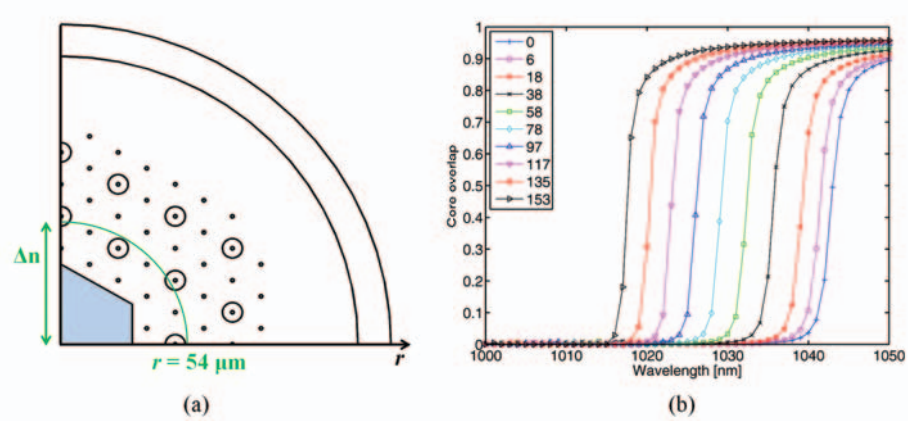

Figure 6.13: (a) The modeled cross-section of a DMF rod fiber with indication of the zero level from the thermal simulations to estimate Δn. (b) The FM photonic bandgap edge movement as a function of wavelength for 10 different signal power levels.

ing the finite-element method and assuming harmonic modes for the z-component, where the thermally induced change in refractive index of the core Δn was integrated. The cross-section is symmetrical along the horizontal and vertical axes, and each subdomain is specified by setting the refractive index, as shown in Fig. 6.13(a). The air cladding of the DMF rod fiber is represented by one outer ring having an NA = 0.6. From these simulations the core overlap of the FM as a function of wavelength was determined for $\Delta n = 0$ and for nine computed non-zero index differences ($\Delta n > 0$) obtained from thermal simulations, shown in Fig. 6.13(b). The FM couples to the resonators inside the inner cladding structure when the wavelength decreases, thereby decreasing the overlap in the core. However as the signal power level increases as a result of increasing pump power the position of the simulated photonic bandgap edge is blue shifted, which agrees well with the experimentally observed trend. The results of these simulations estimate the theoretical guiding regime of this DMF rod fiber design.

The position of the photonic bandgap edge is estimated to be the wavelength at which the the core overlap is reduced to 50 %. This is

shown in Fig. 6.14 together with the experimental estimation of the photonic bandgap edge as a function of output power level. For low output power levels the experimental and simulated positions of the photonic bandgap edge match but as the signal power level increases the simulated results estimate a larger photonic bandgap edge shift. Both the simulated and experimentally determined photonic bandgap edge shift show linear bahavior when plotted versus optical output power of the rod fiber; however, in the case of measured photonic bandgap edges, the shift deviates from this linearity at high output power levels. This could be an indication of saturation of the photonic bandgap edge position. At the moment, the saturation effect of the photonic bandgap edge position is not fully understood.

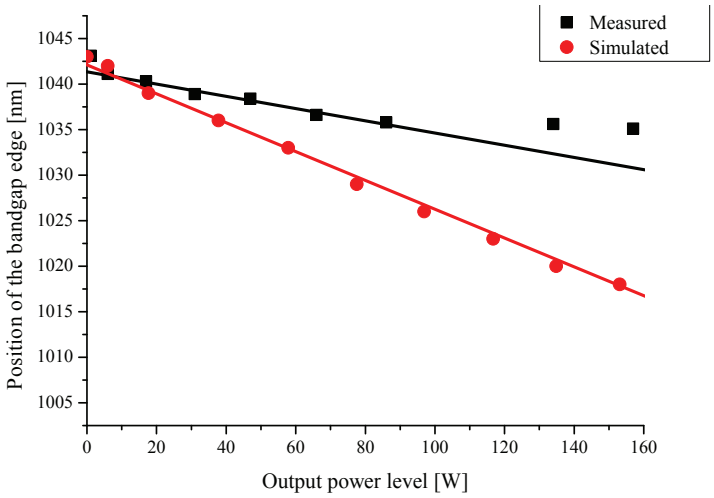

Figure 6.14: Measured and simulated position of the photonic bandgap edge with respect to output power level.

6.3.2 Discussion on temperature induced refractive index change

The position of the simulated and measured photonic bandgap edges exhibit different linear behavior because the simulations represent a local photonic bandgap at the end of the rod fiber and the measured results are of course effectively an average photonic bandgap edge shift over the length of the entire rod fiber. In the simulations an increased homogeneous refractive index profile along the entire rod fiber length is used for each output power level, but this does not take into account the thermal gradient due to uneven pump absorption along the rod fiber length.

Typically, measuring a core temperature of an active fiber or rod fiber is difficult or impossible. It may be necessary in the future to develop a method to measure the temperature of the core as new high power fiber designs with extremely large effective areas are developed and as higher average power levels are demanded from active fibers. As most of active fiber designs are made to support only one or a few modes, even a small increase in the refractive index of the core will shift the fibers toward a multimode regime and cause the fibers to support an increasing number of modes, thereby decreasing the beam quality. Therefore, DMF rod fibers have a unique property where thermally induced refractive index changes can be calculated via the measured position of the photonic bandgap edge.

Both experiments and simulations support the theory that the shift in behavior of DMF rod fibers originates from a thermally induced refractive index profile change inside the rod fiber. Simulated results can be greatly improved by adding complexity to the model to better match experimental conditions, such as by altering the step-index model to take into account the full DMF structure including complications of the boundary conditions imposed by the air-cladding. Also, overestimation of the photonic bandgap edge position at high signal power levels can be corrected for using a decaying refractive index profile along the rod fiber length and including the full DMF structure in the simulation. In addition, only the index inside the hexagonal core, shown in Fig. 6.13, was increased using a step-index like profile and the index of the cladding where the DMF elements reside was not changed. In reality the modes inside the core experience a thermally induced refractive index profile which has a maximum at the center of the core and decreases towards the edge of the core.

The above mentioned improvements will of course increase the complexity of the model and increase the computation time significantly but these changes are feasible to implement. Enhanced simulations should decrease the deviation between simulated and experimental results and provide a great tool to further investigate the exact temperature and refractive index profile inside DMF rod fibers.

6.4 Summary of chapter 6

This chapter introduced a high power rod amplifier setup together with the characterization of the seed source and high power pump module. The rod setup was used with SM DMF rod fibers and this configuration delivered average output powers up to 292 W before MIs were observed.

MIs in high power fibers were discussed and an improvement of 44 % output power increase before the MI threshold level was observed by operating the rod fiber in a leaky wavelength regime (at low power). In addition, a memory effect of the MI threshold level was discussed and a photo-bleaching recovery methods was described. The guiding dynamics of DMF rod fibers were discussed both in experiments and simulations. Finally, a thermally induced refractive index change in the core was reported. A shift of the photonic bandgap edge from 1043 nm to 1035 nm was observed when the signal power level was increased from 0.5 W to 160 W. A new method to quantify the thermally induced change in the refractive index profile in the core was discussed.

Chapter 7

Conclusion

Optical fibers have become a significant part of modern society from their implementation in telecommunications networks to various materials processing methods. New developments, especially in rare earth (RE)-doping of fibers and in fiber designs, have opened the door for a wide range of new applications and power scaling efforts of fiber lasers and amplifiers. Various fiber designs delivering up to multi-kilowatts of output power with single-mode (SM) operation have been demonstrated. However, non-linear effects imparted by the fiber set the limit of maximum pulse energy and peak power generation or amplification and thereby a larger effective core area (A_{eff}) is required to mitigate these non-linear effects. Maintaining SM operation in fibers with very large A_{eff} requires extremely low core numerical aperture (NA), which in turn requires extremely high index precision, which can make manufacturing quite difficult. The implementation of photonic crystal fiber (PCF) technology has enabled the engineering of fiber designs with core diameters up to 100 μm while simultaneously providing more effective methods to suppress higher order modes (HOMs). With these novel designs, traditional methods of determining beam quality generally do not provide enough information and new methods to quantify the modal content of fibers are required. In addition, new fiber designs with more effective HOM suppression over a short propagation length and acceptable manufacturability yield are required as well.

This dissertation presented an experimental study of modal characterization methods within waveguides and the development and characterization of a new SM large mode area (LMA) photonic bandgap (PBG) PCF rod fiber design.

SM properties of a flexible ytterbium (Yb)-doped PCF with a 40 μm core diameter were evaluated using spatially and spectrally resolved (S^2) imaging under various input coupling conditions. The input beam under offset input coupling conditions had little overlap with the fundamental mode (FM) of the fiber under test and thereby HOMs were deliberately excited. An S^2 imaging setup was constructed and calibrated against a standard cut-off wavelength measurement before the SM properties of a PCF were evaluated. The PCF exhibited SM operation under a coiling diameter of 28 cm and HOMs were suppressed $\sim$21 dB below the FM, even under extreme offset input coupling condition. However, as the S^2 imaging method relies on a spectral interference between the supported modes of the core it has its limitations and cannot be used for example to measure modal content of modes having similar weights or fibers with very large cores. Another modal characterization method, cross correlated (C^2) imaging, which is free of the limits of S^2 imaging was used to study guiding dynamics of a new rod type fiber, a fiber developed during this thesis work (85 μm core diameter). Resonant coupling of the HOMs between the core and the cladding band was observed and reported using C^2 imaging to investigate the underlying mechanism of SM operation within this fiber design.

This new rod fiber design is a PBG PCF design utilizing distributed mode filtering (DMF) elements in a cladding structure (high index inclusion), which impart special guiding regimes within the core. The DMF elements provide a mechanism for resonant coupling between the core and the cladding of the rod fiber. Because of the wavelength dependence of this coupling this fiber design has a wavelength range where only the FM is guided in the core and HOMs are supported within other wavelength ranges. Also, there exists a regime where no modes are fully guided in the core (leaky regime). This DMF rod fiber design was successfully used as the gain medium within a laser cavity and operated in continuous wave (CW) and Q-switched configurations. SM operation of the rod fiber resulted in simultaneously near diffraction limited output beam quality with high average power and pulse energy generation using simple laser configuration. The laser exhibited narrow output spectra, yielding high spectral brightness and together with high spatial brightness provided excellent conditions for efficienct harmonic generation. As a result, record high pulse energies at visible (515 nm) and UV (343 nm) wavelengths up to 1 mJ and 500 μJ, respectively were reported from a single stage Q-switched fiber laser cavity.

In order to study gain and guiding properties and mode instabilities (MIs) under high power operation of DMF rod fibers, a high

power rod amplifier setup was constructed. A high power seed source delivering ∼30 ps pulses at 1032.2 nm with up to 17 W of average power was implemented. The DMF rod fibers were then tested up to the MI threshold level and power conversion, efficiency and mode quality were measured and reported. The MI threshold level diminished as it was reached repeatedly, caused by the permanent nature of generation of a developing long-period grating (LPG). A photo-bleaching method using UV light at 405 nm was described and utilized to restore the MI threshold level back to its original value.

Under high power operation the refractive index of the core is modified by a thermally induced refractive index change. An increase of the MI threshold level (44 % increase) was measured and reported by using a DMF rod fiber in the leaky regime at low power and taking advantage of the change in guiding dynamics due to the heat load generated within the core which shifts the rod fiber to the SM guiding regime at high power levels. An average power level of 292 W with near diffraction limited beam was achieved before the MI threshold level was observed. The thermally induced refractive index change was explored by measuring the bandgap positions of the DMF rod fiber using a broad band input signal at various output power levels. The bandgap position for the particular fiber design experienced a shift of over 12 nm, as was reported.

7.1 Future work

An S^2 imaging setup was developed and successfully used to examine SM properties of flexible PCF fiber with a 40 μm core diameter. However, the method fails for fibers with very large core diameters. C^2 imaging was employed on a DMF rod fiber having core diameter of 85 μm. C^2 imaging is a less mature modal characterization method, and as the experiments were performed at Boston University, Boston, USA, it would be essential to develop the method locally at DTU Fotonik, Kgs. Lyngby, Denmark, to explore the method further and find a deeper understanding of possible limits and capabilities of this method. The performed experiments only gave a small glimpse into what the method is capable of. The method would greatly benefit the development of very LMA fibers, especially in the area of verification of SM operation as well as in the characterization of other properties such as group delay or/and dispersion of the modes under thermal load.

The DMF rod fiber design was successfully used under active configurations with near diffraction limited output but a few important

parameters were not characterized e.g. polarization maintaining and long-term reliability of the output power and mode quality. The DMF rod fiber has no polarization maintaining elements but as the high-index elements have no circular symmetry around the core and due to the small mechanical stresses or form birefringence induced in the core during the drawing process the rod fiber can maintain the state of polarization in a certain orientation. However, as the polarization properties and long-term reliability are vital for future commercial use of DMF rod fibers they should be carefully investigated. Also, MIs during high power operation were only brief explored and requires more study, both experimentally and theoretically as MIs seem to be the most dominant limiting factor of future power scaling efforts of fibers with very large core diameters. The thermally induced refractive index change in the core of DMF rod fibers was measured but simulations of the phenomena need to be improved as it appeared the measured values of the bandgap shift were smaller than simulations indicated. The difference is mainly due to the fact that the simulation conditions do not fully match the experiments and complexity needs to be added to better match realistic operation conditions. Several methods to improve the simulations were described and work will continue towards better matching of simulations with experimental results.

List of Acronyms

RE rare earth

SM single-mode

MM multi mode

FM fundamental mode

HOM higher order mode

LMA large mode area

PCF photonic crystal fiber

S^2 spatially and spectrally resolved

C^2 cross correlated

MI mode instability

MIs mode instabilities

PBG photonic bandgap

LPF large pitch fiber

TIR total internal reflection

NA numerical aperture

Er erbium

Yb ytterbium

SEM scanning electron microscope

PM polarization maintaining

SAP stress applying part

ARROW antiresonant reflecting optical waveguide

SRS stimulated Raman scattering

SBS simulated Brillouin scattering

SPM self phase modulation

$\mathbf{A}_{eff}$ effective core area

MFD mode field diameter

CW continuous wave

MOPA master oscillator power amplifier

ASE amplified spontaneous emission

DMF distributed mode filtering

OSA optical spectrum analyzer

FFT fast Fourier transform

FWHM full width half maximum

NF near-field

FF far-field

HR highly reflective

AOM acoustic-optical-modulator

VBG volume Bragg grating

SHG second-harmonic generation

THG third-harmonic generation

PER polarization extinction ratio

LPG long-period grating

$\mathbf{n}_{eff}$ effective refractive index

LBO Lithium Triborate

Bibliography

[1] D. Keck, "On the ultimate lower limit of attenuation in glass optical waveguides," Applied Physics Letters **22**, 307 (1973).

[2] G. P. Agrawal, *Lightwave Technology: Components and Devices* (John Wiley & Son, Inc, 2004).

[3] G. Agrawal, *Fiber-Optic Communications Systems* (John Wiley & Sons, Inc., New York, 2002).

[4] S. Poole, D. Payne, and M. Fermann, "Fabrication of low-loss optical fibres containing rare-earth ions," Electronics Letters **21**, 737 (1985).

[5] R. Mears, L. Reekie, S. Poole, and D. Payne, "Neodymium-doped silica single-mode fibre lasers," Electronics Letters **21**, 738 (1985).

[6] D. Hanna, R. Percival, I. Perry, R. Smart, P. Suni, and A. Tropper, "An Ytterbium-doped Monomode Fibre Laser: Broadly Tunable Operation from 1.010 μm to 1.162 μm and Three-level Operation at 974 Nm," Journal of Modern Optics **37**, 517–525 (1990).

[7] D. J. Richardson, J. Nilsson, and W. A. Clarkson, "High power fiber lasers: current status and future perspectives [Invited]," Journal of the Optical Society of America B **27**, B63 (2010).

[8] A. Tünnermann, T. Schreiber, and J. Limpert, "Fiber lasers and amplifiers: an ultrafast performance evolution." Applied optics **49**, F71–F78 (2010).

[9] A. Giesen, H. Hügel, A. Voss, K. Wittig, U. Brauch, and H. Opower, "Scalable concept for diode-pumped high-power solid-state lasers," Applied Physics B **58**, 365–372 (1994).

[10] W. Jones, L. Goldman, J. Chernoch, and W. Martin, "The mini-FPL - A face-pumped laser: Concept and implementation," IEEE Journal of Quantum Electronics **8**, 534–535 (1972).

[11] L. Zenteno, "High-power double-clad fiber lasers," Journal of Lightwave Technology **11**, 1435–1446 (1993).

[12] G. P. Agrawal, *Nonlinear Fiber Optics* (Academic,, 1995).

[13] J. P. Koplow, D. A. V. Kliner, and L. Goldberg, "Single-mode operation of a coiled multimode fiber amplifier," Optics Letters **25**, 442 (2000).

[14] C.-H. Liu, G. Chang, N. Litchinister, D. Guertin, N. Jacobson, K. Tankala, and A. Galvanauskas, "Chirally Coupled Core Fibers at 1550-nm and 1064-nm for Effectively Single-Mode Core Size Scaling," (2007).

[15] L. Dong, H. A. McKay, L. Fu, M. Ohta, A. Marcinkevicius, S. Suzuki, and M. E. Fermann, "Ytterbium-doped all glass leakage channel fibers with highly fluorine-doped silica pump cladding," Optics Express **17**, 8962 (2009).

[16] T. A. Birks, J. C. Knight, and P. S. Russell, "Endlessly single-mode photonic crystal fiber," Optics Letters **22**, 961 (1997).

[17] J. Limpert, O. Schmidt, J. Rothhardt, F. Röser, T. Schreiber, A. Tünnermann, S. Ermeneux, P. Yvernault, and F. Salin, "Extended single-mode photonic crystal fiber lasers," Optics Express **14**, 2715 (2006).

[18] J. Limpert, N. Deguil-Robin, I. Manek-Hönninger, F. Salin, F. Röser, A. Liem, T. Schreiber, S. Nolte, H. Zellmer, A. Tünnermann, J. Broeng, A. Petersson, and C. Jakobsen, "High-power rod-type photonic crystal fiber laser," Optics Express **13**, 1055 (2005).

[19] O. Schmidt, J. Rothhardt, F. Röser, S. Linke, T. Schreiber, K. Rademaker, J. Limpert, S. Ermeneux, P. Yvernault, F. Salin, and a. Tünnermann, "Millijoule pulse energy Q-switched short-length fiber laser." Optics letters **32**, 1551–3 (2007).

[20] C. D. Brooks and F. Di Teodoro, "Multimegawatt peak-power, single-transverse-mode operation of a 100um core diameter, Yb-doped rodlike photonic crystal fiber amplifier," Applied Physics Letters **89**, 111119 (2006).

[21] F. Jansen, F. Stutzki, H.-J. Otto, M. Baumgartl, C. Jauregui, J. Limpert, and A. Tünnermann, "The influence of index-

depressions in core-pumped Yb-doped large pitch fibers," Optics Express **18**, 26834 (2010).

[22] A. Siegman, "New developments in laser resonators," Proc. SPIE Vol. 1224 **1224**, 2–14 (1990).

[23] A. Siegman, "Defining, measuring, and optimizing laser beam quality," In: Laser resonators and coherent optics: Modeling pp. 2–12 (1993).

[24] S. Wielandy, "Implications of higher-order mode content in large mode area fibers with good beam quality," Optics Express **15**, 15402 (2007).

[25] J. Nicholson, A. Yablon, J. Fini, and M. Mermelstein, "Measuring the Modal Content of Large-Mode-Area Fibers," Selected Topics in Quantum Electronics, IEEE Journal of **15**, 61–70 (2009).

[26] D. N. Schimpf, R. A. Barankov, and S. Ramachandran, "Cross-correlated (C^2) imaging of fiber and waveguide modes," Optics Express **19**, 13008 (2011).

[27] T. T. Alkeskjold, M. Laurila, L. Scolari, and J. Broeng, "Single-mode ytterbium-doped large-mode-area photonic bandgap rod fiber amplifier," Optics Express **19**, 7398 (2011).

[28] T. T. Alkeskjold, M. Laurila, L. Scolari, and J. Broeng, "Low-NA single-mode LMA photonic crystal rod fiber amplifier," in "Proceedings of SPIE," , vol. 7914 (2011), vol. 7914, pp. 79141S–79141S–9.

[29] M. Born and E. Wolf, *Principles of Optics* (Cambridge University Press, New York, 1999), 7th ed.

[30] K. Tankala, D. Guertin, J. Abramczyk, and N. Jacobson, "Reliability of low-index polymer coated double-clad fibers used in fiber lasers and amplifiers," Optical Engineering **50**, 111607 (2011).

[31] R. Windeler, J. Wagener, and D. DiGiovanni, "Silica-air microstructured fibers: properties and applications," in "OFC/IOOC . Technical Digest. Optical Fiber Communication Conference, 1999, and the International Conference on Integrated Optics and Optical Fiber Communication," (IEEE, 1999), pp. 106–107.

[32] W. Wadsworth, R. Percival, G. Bouwmans, J. Knight, T. Birks, T. Hedley, and P. St. J. Russell, "Very High Numerical Aperture Fibers," IEEE Photonics Technology Letters **16**, 843–845 (2004).

[33] J. C. Knight, T. A. Birks, P. S. J. Russell, and D. M. Atkin, "All-silica single-mode optical fiber with photonic crystal cladding," Optics Letters **21**, 1547 (1996).

[34] P. Russell, "Photonic crystal fibers." Science (New York, N.Y.) **299**, 358–62 (2003).

[35] T. A. Birks, J. C. Knight, B. J. Mangan, and P. S. J. Russell, "Photonic Crystal Fibres: An Endless Variety," (2001).

[36] K. P. Hansen, "High-power photonic crystal fibers," in "Proceedings of SPIE," , vol. 6102 (SPIE, 2006), vol. 6102, pp. 61020B–61020B–11.

[37] K. P. Hansen, C. B. Olausson, J. Broeng, D. Noordegraaf, M. D. Maack, T. T. Alkeskjold, M. Laurila, T. Nikolajsen, P. M. W. Skovgaard, M. H. SoÌ¸rensen, M. Denninger, C. Jakobsen, and H. R. Simonsen, "Airclad fiber laser technology," Optical Engineering **50**, 111609 (2011).

[38] J. Laegsgaard, "Gap formation and guided modes in photonic bandgap fibres with high-index rods," Journal of Optics A: Pure and Applied Optics **6**, 798–804 (2004).

[39] T. A. Birks, G. J. Pearce, and D. M. Bird, "Approximate band structure calculation for photonic bandgap fibres," Optics Express **14**, 9483 (2006).

[40] N. M. Litchinitser, A. K. Abeeluck, C. Headley, and B. J. Eggleton, "Antiresonant reflecting photonic crystal optical waveguides," Optics Letters **27**, 1592 (2002).

[41] N. M. Litchinitser, S. C. Dunn, B. Usner, B. J. Eggleton, T. P. White, R. C. McPhedran, and C. M. de Sterke, "Resonances in microstructured optical waveguides," Optics Express **11**, 1243 (2003).

[42] F. Jansen, M. Baumgartl, and H. Otto, "Influence of index depressions in active large pitch fibers," Lasers and Electro- pp. 3–4 (2010).

[43] F. Stutzki, F. Jansen, T. Eidam, A. Steinmetz, C. Jauregui, J. Limpert, and A. Tünnermann, "High average power large-pitch fiber amplifier with robust single-mode operation." Optics letters **36**, 689–91 (2011).

[44] F. Jansen, F. Stutzki, H.-J. Otto, T. Eidam, A. Liem, C. Jauregui, J. Limpert, and A. Tünnermann, "Thermally induced waveguide changes in active fibers," Optics Express **20**, 3997 (2012).

[45] T. Eidam, S. Hädrich, F. Jansen, F. Stutzki, J. Rothhardt, H. Carstens, C. Jauregui, J. Limpert, and A. Tünnermann, "Preferential gain photonic-crystal fiber for mode stabilization at high average powers." Optics express **19**, 8656–61 (2011).

[46] R. Mears, L. Reekie, I. Jauncey, and D. Payne, "Low-noise erbium-doped fibre amplifier operating at 1.54μm," Electronics Letters **23**, 1026 (1987).

[47] P. Blixt, J. Nilsson, T. Carlnas, and B. Jaskorzynska, "Concentration-dependent upconversion in Er/sup 3+/-doped fiber amplifiers: Experiments and modeling," IEEE Photonics Technology Letters **3**, 996–998 (1991).

[48] J. Nilsson, P. Blixt, B. Jaskorzynska, and J. Babonas, "Evaluation of parasitic upconversion mechanisms in Er/sup 3+/-doped silica-glass fibers by analysis of fluorescence at 980 nm," Journal of Lightwave Technology **13**, 341–349 (1995).

[49] V. Kuhn, D. Kracht, J. Neumann, and P. Wessels, "67 W of Output Power From an Yb-Free Er-Doped Fiber Amplifier Cladding Pumped at 976 nm," IEEE Photonics Technology Letters **23**, 432–434 (2011).

[50] Y. Jeong, J. K. Sahu, D. B. S. Soh, C. A. Codemard, and J. Nilsson, "High-power tunable single-frequency single-mode erbium:ytterbium codoped large-core fiber master-oscillator power amplifier source," Optics Letters **30**, 2997 (2005).

[51] H. Pask, R. Carman, D. Hanna, A. Tropper, C. Mackechnie, P. Barber, and J. Dawes, "Ytterbium-doped silica fiber lasers: versatile sources for the 1-1.2 μm region," IEEE Journal of Selected Topics in Quantum Electronics **1**, 2–13 (1995).

[52] R. Paschotta, J. Nilsson, A. Tropper, and D. Hanna, "Ytterbium-doped fiber amplifiers," IEEE Journal of Quantum Electronics **33**, 1049–1056 (1997).

[53] D. Payne, Y. Jeong, J. Nilsson, J. Sahu, D. Soh, C. Algeria, C. Codemard, V. Philippov, V. Hernandez, R. Horley, L. Hickey, C. Wanzcyk, C. Chryssou, J. Alvarez-Chavez, and P. Turner, "Kilowatt-class single-frequency fiber sources," (2005).

[54] J. Nilsson and D. N. Payne, "High-power fiber lasers." Science (New York, N.Y.) **332**, 921–2 (2011).

[55] E. Snitzer, H. Po, F. Hakimi, R. Tumminelli, and B. McCollum, "Double clad, offset core Nd fiber laser - OSA Technical Digest Series," in "Optical Fiber Sensors," , vol. 2 (Optical Society of America, 1988), vol. 2, p. PD5.

[56] H. Po, E. Snitzer, R. Tumminelli, L. Zenteno, F. Hakimi, N. M. Cho, and T. Haw, "Double clad high brightness Nd fiber laser pumped by GaAlAs phased array - 1989 OSA Technical Digest Series," in "Optical Fiber Communication Conference," , vol. 5 (Optical Society of America, 1989), vol. 5, p. PD7.

[57] O. Svelto, *Principle of Lasers* (Springer, 1998), 4th ed.

[58] M. L. Osowski, W. Hu, R. M. Lammert, S. W. Oh, P. T. Rudy, T. Stakelon, L. Vaissie, and J. E. Ungar, "Advances in high-brightness semiconductor lasers," in "Proceedings of SPIE," , vol. 6952 (SPIE, 2008), vol. 6952, pp. 695208–695208–8.

[59] F. Gonthier, "High-power All-Fiber components: the missing link for high-power fiber lasers," in "Proceedings of SPIE," , vol. 5335 (SPIE, 2004), vol. 5335, pp. 266–276.

[60] Y. Jeong, A. J. Boyland, J. K. Sahu, S.-H. Chung, J. Nilsson, and D. N. Payne, "Multi-kilowatt single-mode ytterbium-doped large-core fiber laser," (2009).

[61] IPG, "Single-Mode Fiber Laser produces bright, 10 kW output." IPG Photonics (2012).

[62] E. Stiles, "New developments in IPG fiber laser technology," in "Proceedings of the 5th International Workshop on Fiber Lasers," (2009).

[63] J. Limpert, F. Roser, and D. Schimpf, "High repetition rate gigawatt peak power fiber laser systems: challenges, design, and experiment," Selected Topics in **15**, 159–169 (2009).

[64] F. Stutzki, F. Jansen, A. Liem, C. Jauregui, J. Limpert, and A. Tünnermann, "26 mJ, 130 W Q-switched fiber-laser system with near-diffraction-limited beam quality," Optics Letters **37**, 1073 (2012).

[65] F. Ilday, J. Buckley, L. Kuznetsova, and F. Wise, "Generation of 36-femtosecond pulses from a ytterbium fiber laser," Optics Express **11**, 3550 (2003).

[66] U. Keller, K. Weingarten, F. Kartner, D. Kopf, B. Braun, I. Jung, R. Fluck, C. Honninger, N. Matuschek, and J. Aus der Au, "Semiconductor saturable absorber mirrors (SESAM's) for femtosecond to nanosecond pulse generation in solid-state lasers," IEEE Journal of Selected Topics in Quantum Electronics **2**, 435–453 (1996).

[67] I. Kelson and A. Hardy, "Strongly pumped fiber lasers," IEEE Journal of Quantum Electronics **34**, 1570–1577 (1998).

[68] W. Koechner, *Solid-State Laser Engineering* (Springer, 2006), 6th ed.

[69] K. R. Hansen, T. T. Alkeskjold, J. Broeng, and J. Lægsgaard, "Thermo-optical effects in high-power Ytterbium-doped fiber amplifiers," Optics Express **19**, 23965 (2011).

[70] J. Koponen, M. Söderlund, H. J. Hoffman, D. A. V. Kliner, J. P. Koplow, and M. Hotoleanu, "Photodarkening rate in Yb-doped silica fibers," Applied Optics **47**, 1247 (2008).

[71] J. Koponen, M. Laurila, and M. Hotoleanu, "Inversion behavior in core- and cladding-pumped Yb-doped fiber photodarkening measurements," Applied Optics **47**, 4522 (2008).

[72] E. J. Friebele and D. L. Griscom, "Color Centers in Glass Optical Fiber Waveguides," MRS Proceedings **61** (1985).

[73] S. Yoo, C. Basu, A. J. Boyland, C. Sones, J. Nilsson, J. K. Sahu, and D. Payne, "Photodarkening in Yb-doped aluminosilicate fibers induced by 488 nm irradiation," Optics Letters **32**, 1626 (2007).

[74] K. E. Mattsson, "Photo darkening of rare earth doped silica," Optics Express **19**, 19797 (2011).

[75] F. Auzel and P. Goldner, "Towards rare-earth clustering control in doped glasses," Optical Materials **16**, 93–103 (2001).

[76] T. Kitabayashi, M. Ikeda, M. Nakai, T. Sakai, K. Himeno, and K. Ohashi, "Population Inversion Factor Dependence of Photodarkening of Yb-Doped Fibers and Its Suppression by Highly Aluminum Doping - Technical Digest (CD)," in "Optical Fiber Communication Conference and Exposition and The National Fiber Optic Engineers Conference," (Optical Society of America, 2006), p. OThC5.

[77] M. Engholm, P. Jelger, F. Laurell, and L. Norin, "Improved photodarkening resistivity in ytterbium-doped fiber lasers by cerium codoping," Optics Letters **34**, 1285 (2009).

[78] R. G. Smith, "Optical Power Handling Capacity of Low Loss Optical Fibers as Determined by Stimulated Raman and Brillouin Scattering," Applied Optics **11**, 2489 (1972).

[79] Telecommunications Industry Association, "Measurement methods and test procedures cut-off wavelength," Tech. rep., TIA Standards, FOTP-80 IEC-60793-1-44 Optical Fibres - Part 1-44 (2003).

[80] T. Sø rensen, J. Broeng, A. Bjarklev, E. Knudsen, and S. Barkou Libori, "Macro-bending loss properties of photonic crystal fibre," Electronics Letters **37**, 287 (2001).

[81] J. W. Nicholson, A. D. Yablon, S. Ramachandran, and S. Ghalmi, "Spatially and spectrally resolved imaging of modal content in large-mode-area fibers," Optics Express **16**, 7233 (2008).

[82] J. Nicholson, J. Jasapara, A. Desantolo, and E. Monberg, "Characterizing the modes of a core-pumped, large-mode area Er fiber using spatially and spectrally resolved imaging," in "Lasers and Electro-Optics, 2009 and 2009 Conference on Quantum electronics and Laser Science Conference, CLEO/QELS 2009," (2009).

[83] J. W. Nicholson, J. M. Fini, A. M. DeSantolo, E. Monberg, F. DiMarcello, J. Fleming, C. Headley, D. J. DiGiovanni, S. Ghalmi, and S. Ramachandran, "A higher-order-mode Erbium-doped-fiber amplifier," Optics Express **18**, 17651 (2010).

[84] J. Nicholson, J. Fini, S. Ghalmi, J. Jasapara, A. DeSantolo, E. Monberg, and F. Dimarcello, "Measuring the modes of optical fibers using S2 imaging," in "Lasers and Electro-Optics (CLEO) and Quantum Electronics and Laser Science Conference (QELS), 2010 Conference on," (2010).

[85] J. Bromage, C. Dorrer, M. Shoup, and J. Zuegel, "Optimizing injection into large-mode-area photonic crystal-fiber amplifiers by spatially resolved spectral interferometry," in "Lasers and Electro-Optics, 2009 and 2009 Conference on Quantum electronics and Laser Science Conference. CLEO/QELS 2009. Conference on," (2009).

[86] B. G. Ward, "Bend performance-enhanced photonic crystal fibers with anisotropic numerical aperture," Optics Express **16**, 8532 (2008).

[87] D. N. Schimpf and S. Ramachandran, "Polarization-resolved imaging of an ensemble of waveguide modes," Optics Letters **37**, 3069 (2012).

[88] R. A. Barankov, "Cross-correlation Imaging for Waveguide Characterization," M. S. Thesis, http://arxiv.org/abs/1206.0666 (2012).

[89] M. M. Jørgensen, S. R. Petersen, M. Laurila, J. Læ gsgaard, and T. T. Alkeskjold, "Design optimization of the distributed modal filtering rod fiber for increasing single mode bandwidth," in "Proceedings of SPIE," , vol. 8237 (2012), vol. 8237, pp. 82373P–82373P–10.

[90] S. Ramachandran, J. Nicholson, S. Ghalmi, and M. Yan, "Measurement of multipath interference in the coherent crosstalk regime," IEEE Photonics Technology Letters **15**, 1171–1173 (2003).

[91] J. Saby, B. Cocquelin, A. Meunier, S. Pierrot, P.-J. Devilder, P. Deslandes, and F. Salin, "High average and peak power pulsed fiber lasers at 1030 nm, 515 nm, and 343 nm," in "Proceedings of SPIE," , vol. 7580 (2010), vol. 7580, pp. 75800I–75800I–11.

[92] R. Bello-Doua, F. Salin, and E. Freysz, "Harmonics generation from rod-type Yb doped fiber laser," in "Lasers and Electro-Optics, 2008 and 2008 Conference on Quantum Electronics and Laser Science. CLEO/QELS 2008. Conference on," (2008).

[93] A. V. Smith and J. J. Smith, "Mode instability in high power fiber amplifiers," Optics Express **19**, 10180 (2011).

[94] T. Eidam, C. Wirth, C. Jauregui, F. Stutzki, F. Jansen, H.-J. Otto, O. Schmidt, T. Schreiber, J. Limpert, and A. Tünnermann, "Experimental observations of the threshold-like onset of mode instabilities in high power fiber amplifiers," Optics Express **19**, 13218 (2011).

[95] C. Jauregui, T. Eidam, J. Limpert, and A. Tünnermann, "The impact of modal interference on the beam quality of high-power fiber amplifiers," Optics Express **19**, 3258 (2011).

[96] H.-J. Otto, F. Stutzki, F. Jansen, T. Eidam, C. Jauregui, J. Limpert, and A. Tünnermann, "Temporal dynamics of mode instabilities in high-power fiber lasers and amplifiers," Optics Express **20**, 15710 (2012).

[97] C. Jauregui, T. Eidam, H.-J. Otto, F. Stutzki, F. Jansen, J. Limpert, and A. Tünnermann, "Physical origin of mode instabilities in high-power fiber laser systems," Optics Express **20**, 12912 (2012).

[98] B. Ward, C. Robin, and I. Dajani, "Origin of thermal modal instabilities in large mode area fiber amplifiers," Optics Express **20**, 11407 (2012).

[99] I. Manek-Hönninger, J. Boullet, T. Cardinal, F. Guillen, S. Ermeneux, M. Podgorski, R. Bello Doua, and F. Salin, "Photodarkening and photobleaching of an ytterbium-doped silica double-clad LMA fiber," Optics Express **15**, 1606 (2007).